

Optical Fiber-Based Corrosion Sensor Systems

by

Mark S. Miller

Dissertation submitted to the faculty of the Virginia Polytechnic Institute and State University in partial fulfillment of the requirements for the degree of

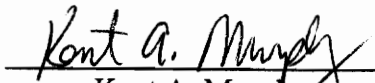
Doctor of Philosophy

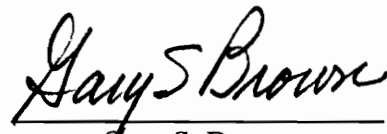
in

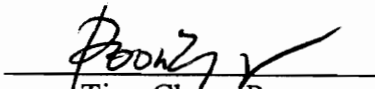
Electrical Engineering

APPROVED:


Richard O. Claus, Chairman


Kent A. Murphy


Gary S. Brown


Ting-Chung Poon


J. Kenneth Shaw

August 1995

Blacksburg, Virginia

C.2

LD

5655

V856

1995

M556

C.2

Handwritten signature or scribble

Optical Fiber-Based Corrosion Sensor Systems

by

Mark S. Miller

Richard O. Claus, Chairman

Electrical Engineering

(ABSTRACT)

An investigation into optical fiber sensing methods for monitoring metallic corrosion is presented. A series of sensing techniques are presented and explored, and two techniques are identified as possible candidates for a corrosion sensing system. The first is a technique based on the phenomenon of surface plasmon resonance, a technology useful in the sensing of changes in the index of refraction of a material in a localized area. The second involves the use of a metal-clad fiber sensing region where the standard core/cladding fiber geometry is modified to have a silica core and a metal cladding.

A series of improvements to the current surface plasmon devices lead to the choice of a multimode cylindrical geometry for the sensor fiber. Under the correct conditions, energy in the TM modes in the fiber will transfer to a surface plasmon mode coupled to the surface of a metal film on the fiber. Monitoring the spectral output of the sensor provides information on the change in index of refraction of the surrounding material or the remaining thickness of the metal film applied to the fiber.

The metal-clad sensor involves replacing the standard dielectric cladding with a metal in the sensing region. The loss of power through this region is directly related to the thickness of the metal cladding, which decreases with corrosion. A theoretical analysis is performed and compared with experimental results which demonstrate the feasibility of the sensing technique.

Both the surface plasmon approach and the metal-clad approach are demonstrated as corrosion presence indicators, that is, they cannot currently resolve the level of corrosion, but just indicate when a certain amount of corrosion has occurred. The metal-clad technique is therefore identified as the most practical technique due to its relatively simple operation and easily understandable output response to corrosion. Future improvements are presented for the metal-clad sensor to help resolve the total amount of corrosion and a method is demonstrated for the repeatable fabrication of the metal-clad sensor.

ACKNOWLEDGMENTS

I would like to thank Dr. Richard O. Claus, my advisor, for helping to foster a research environment dedicated to the state-of-the-art, but still a place where one can enjoy the people and work that are involved. The Fiber & Electro-Optics Research Center (FEORC) is a wonderful institution. I would also like to thank Dr. Kent A. Murphy for his guidance over the years, but more importantly for his friendship. Thank you to Dr. Gary S. Brown, Dr. Ting-Chung Poon, and Dr. J. Kenneth Shaw for serving on my committee and their understanding in the last months as I prepared this dissertation while taking a new job in Minneapolis.

To the remainder of FEORC, my thanks for a great seven years. Help has come from many people including the staff: Mike Gunther, Russ May, Linda Jones, Dr. Marten deVries, and the others who have come and gone; and the students. A special thanks goes to Jason Zeakes and Anjana Nagarajan who helped so much in the research described in this dissertation. Jason was responsible for the development of the control system for the modified sputtering chamber as well as the analysis of the metal films fabricated using that chamber, and Anjana helped perform the experiments using the sodium hydroxide test cell.

My thanks also go out to Dr. Shinjo Onishi, formerly with the microelectronics lab in the electrical engineering department, for his initiation of the modified sputtering chamber. His insight made the chamber a reality. I would also like to thank Dr. William Bender for introducing me to surface plasmons and allowing me to learn from him while developing the surface plasmon model. His test results form the background that is presented in this work.

This research would not have been possible without the support of the Boeing Corporation. The people there provided immeasurable help in the understanding of the corrosion problem and for discussing ideas and results. Thank you to Donald Bartlett for beginning the support and to Paul Rutherford for continuing the support of this work and for allowing me the latitude to explore many ideas and technologies while working toward a practical sensing system.

Finally, I would like to thank my family for all of their support throughout the years as I pursued my dreams. To my parents, Theodore and Martha, thanks for getting me started in the right direction and never losing faith in me. To my brothers, Daniel and Andrew, for their support and much needed injection of reality. Most especially, to my wife, Rebecca, and son, Robert, who have stood by me in the darkest of times to always show me the light. Even though Robert could not understand why daddy had to work all the time, his support and presence have made life a little better. This dissertation is dedicated to you, Rebecca and Robert.

Table of Contents

Chapter 1 Introduction	1
Chapter 2 Corrosion	4
2.1 Corrosion Classification	7
2.2 State-of-the-Art Corrosion Detection Techniques	9
Chapter 3 Fiber Optic Corrosion Sensing	15
3.1 Enthalpy Monitoring	16
3.2 Magnetic Field Detection	16
3.3 Signature Testing	17
3.4 Acoustic Emission Monitoring	20
3.5 Reflection Techniques	24
3.5.1 Spectral reflectance monitoring	24
3.5.2 Extrinsic pure reflection monitoring	26
3.5.3 Intrinsic pure reflection monitoring	31
3.6 Transmission Techniques	36
3.6.1 Metal coated optical fiber sensor	36
3.6.2 Surface plasmon sensing technique	37
3.6.3 Metal-clad optical fiber sensor	37
Chapter 4 Surface Plasmon Sensor	38
4.1 History	38
4.2 3-Layer Surface Plasmon Resonance	41
4.2.1 Theoretical analysis	41
4.2.2 Experimental results	45
4.3 4-Layer Surface Plasmon Resonance	47
4.3.1 Theoretical analysis	47
4.3.2 Experimental results	53
4.4 Cylindrical Surface Plasmon Resonance	56
4.4.1 Theoretical analysis	58
4.4.2 Experimental results	58
Chapter 5 Metal-Clad Corrosion Sensor	62
5.1 Theoretical Analysis	66
5.2 Aluminum-Clad NaOH Tests	74
5.2.1 Experimental setup	75
5.2.2 Sensor fabrication	75
5.2.3 Experimental results	77
5.3 Sputter-Coated Sensor	89

5.3.1 Sensor fabrication unit	89
5.3.2 Sensor fabrication	93
5.3.3 Sensor analysis	99
5.3.4 Sensor fabrication and testing	108
Chapter 6 Discussion	110
6.1 Surface Plasmon Approach	110
6.2 Metal-Clad Corrosion Sensor	112
6.2.1 Tapered aluminum sensors	113
6.2.2 Reflective sensor design	116
References	119
Appendix A Computer Programs	122
Vita	130

List of Illustrations

2.1 A diagram of a corrosion cell	5
3.1 Schematic of an elliptical-core two-mode optical fiber sensor setup.....	19
3.2 Schematic of an EFPI sensor	22
3.3 A Mach-Zehnder optical fiber interferometer	23
3.4 A Michelson optical fiber interferometer	23
3.5 Schematic of the spectral reflectance setup.....	25
3.6 spectrums of the reflected signals from pure and corroded aluminum	25
3.7 Schematic of the corrosion monitoring test cell.....	28
3.8 Schematic of the sensor support system	29
3.9 Plot of the extrinsic type reflection sensor versus time	30
3.10 A graph of the reflectance aluminum thin film for several wavelengths	33
3.11 Schematic of the intrinsic reflection sensor.....	35
3.12 Reflected power versus time for two aluminum end coated fibers	35
4.1 Kretschmann prism assembly	40
4.2 Schematic of a fiber optic surface plasmon device	43
4.3 Dispersion plot for a 3-layer system	44
4.4 Experimental curves for the 3-layer surface plasmon device.....	46
4.5 Schematic of the 4-layer surface plasmon geometry.....	49
4.6 Dispersion relation for the 4-layer geometry	54
4.7 Experimental curve for the 4-layer sensor.....	55
4.8 Dispersion curve for the modified 4-layer geometry with underlay	57
4.9 Reprint of the theoretical curve for spectral analysis of the cylindrical device .	59
4.10 Spectrum of cylindrical device at a sample index of 1.3595.....	61
4.11 Spectrum of cylindrical device at a sample index of 1.3856.....	61

5.1 Schematic of the metal-clad corrosion sensor	63
5.2 Output power versus time for two aluminum-clad corrosion sensors	65
5.3 Schematic of a fiber and the ray-optics approximation.....	67
5.4 A metal film between two dielectric media.....	70
5.5 Theoretical data for power level versus thickness.....	73
5.6 The setup of the NaOH etch tests for the aluminum-clad sensor	76
5.7 Schematic of the splice for the aluminum-clad sensor	78
5.8 Power versus time for a 3” sensor with 633 nm light.....	79
5.9 Power versus time for a 10.4” sensor with 633 nm light.....	79
5.10 Theoretical data for a 3” sensor using 633 nm light.....	81
5.11 Theoretical data for a 10.4” sensor using 633 nm light.....	82
5.12 Experimental data for a 3” sensor using a 1300 nm source.....	84
5.13 Theoretical curve for a 3” sensor and a source at 1300 nm.....	85
5.14 Experimental curve for a 4” sensor and 850 nm source	87
5.15 Theoretical curve for a 4” sensor and 850 nm source	88
5.16 Schematic of the vacuum deposition chamber and fiber holder.....	91
5.17 Block diagram of the positioning system.....	92
5.18 Photograph of the positioning system.....	94
5.19 The in-line aluminum-clad corrosion sensor	95
5.20 Platform for mounting fibers for etching.....	97
5.21 Photograph of the mounting platform with loaded fibers.....	97
5.22 Schematic of the etching assembly.....	98
5.23 Photograph of the completed etching assembly	98
5.24 SEM photograph of the 7075 film	101
5.25 EDAX spectral analysis of the 7075 film	102
5.26 Color composite showing the distribution of elements in the film	104
5.27 SEM photograph of the sputter coated 2024 film.....	105
5.28 Spectrum of the 2024 film	106

5.29 Color composite of the 2024 film.....	107
5.30 Corrosion sensor test setup	109
6.1 Diagram of process and anticipated results of the masking technique.....	114
6.2 The acid etch technique	115
6.3 NaOH etch test on a 4” half-etched aluminum-clad sensor.....	117
6.4 Proposed reflective aluminum-clad corrosion sensor.....	118

List of Tables

5.1 Aluminum alloy 7075	100
5.2 Aluminum alloy 2024	103

CHAPTER 1: INTRODUCTION

Metallic materials are used extensively in most contemporary structures, and the corrosion of those structures has become a serious problem. This is especially true for aircraft, where corrosion-induced fatigue and weakening of structural components can lead to catastrophic failures causing the loss of human lives and costing millions of dollars in damage. An *in-situ*, continuous corrosion detection system is needed, not only for the aircraft industry, but for all cases where corrosion of metal structures is a problem. Optical fiber sensors present a unique opportunity for the development of such a system.

This dissertation research was performed to design, fabricate and demonstrate a practical corrosion sensing technique for aircraft applications. The technique chosen was required to have commercial potential including reasonable cost, good reliability, and a repeatable manufacturing technique.

Optical fibers have been investigated and used for nearly three decades, mostly in the communications industry. An optical fiber is a waveguiding structure with a core and cladding where the core is of a higher index of refraction than the cladding. Light entering the core at one end of the fiber is confined to the core by the phenomenon of total internal reflection. It is not the intent of this dissertation to explain the operation of optical fibers, but for more information about optical fibers see references [1] and [2].

Optical fiber sensors offer many advantages over other sensing techniques for aircraft applications. Some of these advantages are: an inherent immunity to electro-magnetic interference (EMI), small size, light weight, high sensitivity and accuracy, and good potential multiplexing capabilities. Optical fiber sensors operate on the principle that an external perturbation will cause a variation or fluctuation in a specific characteristic of light field propagating in the fiber. The characteristics of the light field that may change include intensity, phase, polarization, wavelength, or time of propagation. In order to sense corrosion, the corrosion must cause a change in one of these characteristics of the light traveling in the optical fiber.

In order to determine the exact method by which the corrosion process can alter the light traveling in the fiber, a detailed analysis of the corrosion process was performed. Additionally, existing techniques for monitoring corrosion were investigated to determine if any of these techniques could offer insight into optical fiber-based corrosion sensing alternatives or possibly even apply directly. This investigation, presented in Chapter 2 provided the information necessary to develop a series of ideas for using optical fiber sensors to monitor corrosion.

The ideas developed after the investigation of corrosion and current corrosion sensing techniques were then analyzed. Some of these sensing techniques were dismissed after short investigations because these sensors had obvious flaws and were obviously not feasible. Other sensing techniques were tested experimentally to determine their feasibility. After testing, additional sensors were dismissed because of low sensitivity, or other problems that were discovered during the testing. Chapter 3 describes the sensing techniques that were identified and the results of the investigation into each of these techniques.

Two fiber sensing techniques were identified as potentially good alternatives for a practical corrosion sensing system. The two techniques are: surface plasmon-based corrosion sensors and metal-clad corrosion sensors. Surface plasmon-based sensors have been studied extensively in the past for monitoring index of refraction changes caused by chemical reactions [3,4]. Since corrosion is also a chemical reaction, initial tests indicated that the use of surface plasmons could provide information about the corrosion process. Chapter 4 is a description of the investigation into surface plasmons for corrosion sensing.

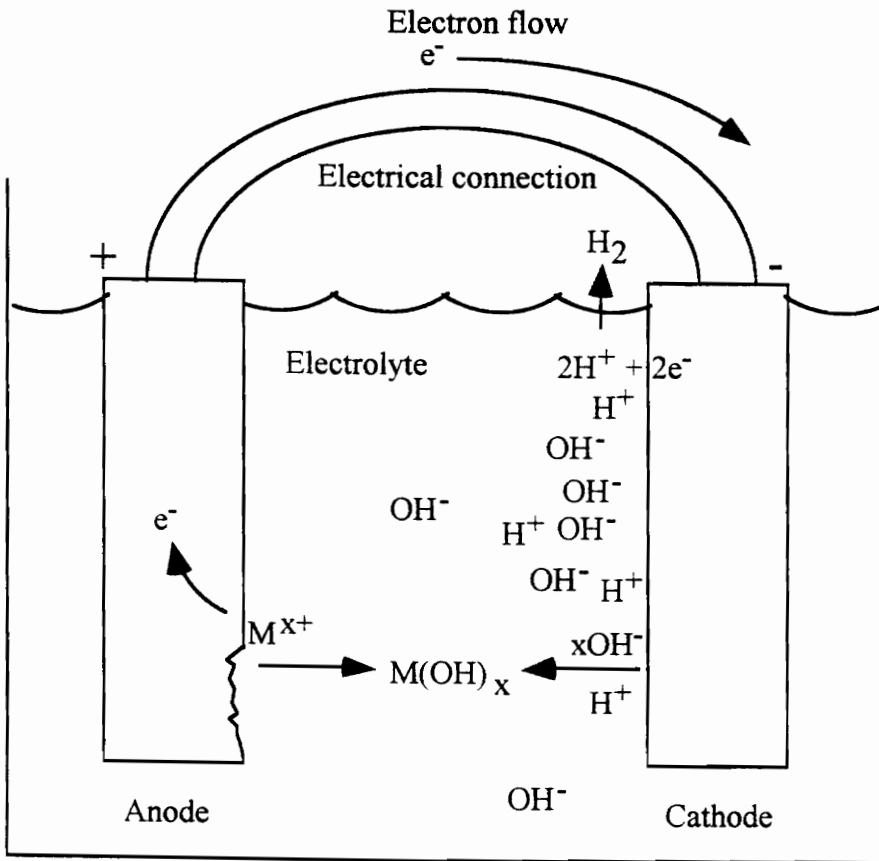
Chapter 5 describes the investigation into the use of metal-clad optical fibers for corrosion sensing. For this sensor, the fiber structure has been modified from a glass core and cladding to a glass core and a metal cladding, where the metal cladding matches the metal that is being monitored for corrosion. Although, by definition, this is not a true waveguide, light will still be confined to the core for a certain distance by repeated reflection at the core-metal interface. By keeping the active region relatively short, approximately 25 centimeters (cm) or less, light with an amplitude large enough to be detectable is monitored at the output. This sensing method monitors the thinning of the metal that forms the cladding. Thinning of the metal is indicative of the corrosion process.

The conclusions drawn by this research include that both the surface plasmon technique and the metal-clad technique could potentially be used to monitor the corrosion process. However, the metal-clad sensor is a simpler system and therefore inherently more practical. The experiments using the surface-plasmon sensor demonstrated the eventual ability to monitor corrosion, but as those experiments also show, the surface-plasmon sensor still requires more development before it will offer the same corrosion monitoring capabilities as the metal clad sensor. Chapter 6 provides a further discussion of the sensing techniques and possible future work.

CHAPTER 2: CORROSION

Although metallic corrosion is given many different definitions [4-10], a common factor in all definitions is the deterioration of a metal due to a chemical reaction with constituents within its surrounding environment. More specifically, the chemical reaction will return the metal to its natural state. A metal's natural state, usually an oxide, is the state in which the metal is found in the earth's crust. Because the natural state of a metal is not the form used in industry, where a pure state of the metal or an alloy is preferred, the corrosion process is a natural process. Therefore, whenever the necessary ingredients are present, corrosion will occur spontaneously.

Corrosion is a process similar to that which occurs in a battery and therefore, there are four necessary conditions for corrosion to occur: there must be an anode - the metal that gives up ions, there must be a cathode - the metal receiving the ions from the anode, there must be an electrolyte between the anode and cathode, and there must be an electrical connection between the anode and cathode. The anode and cathode can be any combination of metals, or the cathode could be a conductive plastic, or the anode and cathode could be different regions of the same metal. The electrolyte transports the ions released by the reaction at the anode to the cathode. The electrolyte most commonly found is moisture, anything from a pool of water to very humid air. The electrical connection allows the flow of electrons between the anode and cathode. Figure 2.1 shows a diagram of a typical corrosion cell.



M^{x+} : Represents the metal ion, x is the charge of the ion

$M(OH)_x$: Represents the metal hydroxide, again x is the charge of the ion

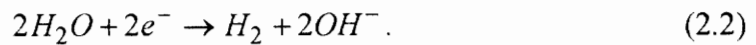
Figure 2.1 A diagram of a corrosion cell.

The corrosion process is a chain reaction starting with the release of electrons at an anode, forming positively charged ions. The ions move off of the surface of the anode into the electrolyte. The electrons move through the electrical connection to the cathode. The ions react with the molecules of the electrolyte forming metal oxides (usually) and releasing hydrogen ions. The hydrogen ions migrate toward the cathode to pick up the electrons that gather there and form hydrogen molecules.

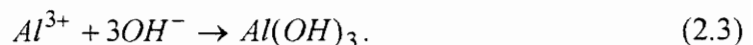
Aluminum, the most commonly used metal on aircraft, and the metal used during this research program in the fabrication and testing of corrosion sensors, has an ionization equation given by



where e^{-} represents electrons. The electrons will react with water, the most common electrolyte and used here for simplicity, and form hydroxide ions as follows

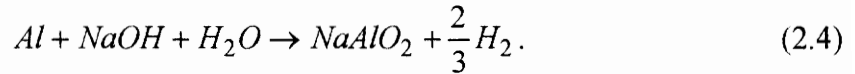


The final reaction occurs as the metal ions pair with the hydroxide ions to form a metal hydroxide. The formula is given by



The presence of other ions, such as chlorine (Cl^{-}) formed when salt ($NaCl$) is added to water, can form other metal compounds, but the process is similar to the one described above. These other compounds do speed up the corrosion process because the compounds dissolve naturally into ions and offer immediate sites for reaction with the metal as opposed to pure water where the water molecules need to be broken down before reacting with the metal.

This is especially true with sodium hydroxide ($NaOH$) which readily breaks down to the Na^+ and OH^- ions in water and reacts well with aluminum. The reaction is described by



In fact, the more alkaline the solution (above a pH of 8) the more rapidly the corrosion process occurs [6]. This helps explain the reaction with $NaOH$ which when added to water forms a highly alkaline solution. $NaOH$ was utilized during this research to increase the rate of corrosion in corrosion test cells for corroding prototype metal-clad corrosion sensors as described in Chapter 5.

Some results of the corrosion process are stress corrosion cracking and corrosion fatigue. Stress corrosion cracking occurs when the material is weakened by the corrosion process and normal stresses become too much for the material to handle. The result is a crack in the material caused at much lower loading than would be expected for the pure metal. Stress may also increase the localized corrosion rate which in hastens the weakening of the metal and leads to a stress corrosion crack. Corrosion fatigue is the failure of the material due to cyclic loading after it has been weakened by the corrosion process. A very small amount of corrosion can cause corrosion fatigue.

2.1 Corrosion Classification

Corrosion is most often categorized by the conditions that cause the corrosion as well as the method by which the corrosion progresses. There are six well-known categories of corrosion: galvanic, uniform, crevice, intergranular, pitting, and exfoliation. Galvanic corrosion occurs between two dissimilar metals in electrical contact in the presence of an electrolyte. The metal more resistant to corrosion becomes the cathode and the other the anode. In general, the anodic metal corrodes much faster in this situation than if it were alone. The development of galvanic corrosion can be predicted in regions where there

are two different metals in contact and avoided if these regions are minimized or protected from electrolytes.

Uniform corrosion occurs on a single metal where the anode and cathode randomly and constantly move around the material causing uniform attack. Uniform corrosion would occur, for example, when a single sheet of metal is left in a highly corrosive environment, such as outside near the sea. In the type of situation described above, corrosion would occur on the metal at random locations. This type of corrosion is possibly the most difficult to prevent since it is unknown where the corrosion will start

Uniform corrosion will be the focus of this research program because it is the most common corrosion phenomenon and the most difficult to detect. As will be seen in the following descriptions, the remainder of the corrosion classes require certain conditions to occur which makes them easier to predict and monitor.

Crevice corrosion occurs when two pieces of metal are in close contact which forms a crevice between them. When an electrolyte is introduced into the crevice, a complex series of events occur causing corrosion inside the crevice. First, a normal corrosion reaction takes place in the crevice. When all of the oxygen in the crevice is depleted, the electrons begin traveling to the outside of the crevice. The positive charge from the ions building up in the crevice due to the absence of oxygen draws other ions from the electrolyte into the crevice. For sea water, the ions are chloride ions which eventually help accelerate the corrosion process inside the crevice. The reactions outside of the crevice also accelerates and a layer of hydroxide ions is formed on the surface, effectively protecting the surface from corrosion. Therefore, a large amount of corrosion occurs inside the crevice, while very little occurs outside. Crevice corrosion is similar to galvanic corrosion because there are two pieces of metal present. However, the metals do not need to be dissimilar for Crevice corrosion to occur.

Intergranular corrosion occurs at the grain boundaries of metals. This type of corrosion can start off as uniform corrosion or other types of corrosion. The boundaries act somewhat like dissimilar metals which makes this corrosion process similar to galvanic corrosion. However the process can occur anywhere there is a grain boundary on a metal surface. This process is limited to the metal surface because of the requirement for an electrolyte to be present. Therefore it is much more difficult to predict intergranular corrosion than it is to predict galvanic corrosion. The sensors developed in this research will also detect intergranular corrosion since it is also similar to uniform corrosion in that it can occur anywhere on the surface of the metal and has the same byproducts and effects as uniform corrosion.

Pitting corrosion results in holes in the material surface. The mechanism is the same as that for crevice corrosion, but the reaction occurs at localized sites on the metal's surface. The process starts as uniform or intergranular corrosion but stays localized thereby causing a small pit. The crevice corrosion process then begins, widening the pit and propagating itself.

Exfoliation corrosion is simply an advanced stage of intergranular corrosion. Essentially, there is so much product created by the corrosion process that it begins to push up on the surface grains of the material or on the coatings. This type of corrosion appears as bubbles on the surface of the material.

2.2 State-of-the-Art Corrosion Detection Techniques

There are currently many techniques used to detect corrosion. The corrosion monitoring techniques found to date include: visual inspection, ultrasonic testing, eddy current testing, radiography (both neutron and x-ray), acoustic emission detection, witness coupons, and hydrogen probes [9-14]. There are other techniques currently under

development, but the aforementioned techniques represent the most widely used and will provide a good representation of what is available.

Visual Inspection: This is the simplest and most common method for detecting corrosion. Essentially, a technician moves around the aircraft and looks for evidence of corrosion. Conversations with Richard Butler, an engineer in the NAVAIR Engineering Support Office in the Naval Aviation Depot, Norfolk, Virginia, indicated that technicians also tap the structure with small hammers and listen for audible changes that indicate corrosion. The aircraft are also disassembled periodically in order to investigate inner parts of the structure. Specific signs of corrosion include: a dulling of the surface shine, white powder caused by exfoliation corrosion, small black dots indicating pitting corrosion, bubbling of painted surfaces, and general roughness of the surfaces caused by the corrosion byproducts. Obviously, the disassembly of aircraft is a time consuming and costly procedure. This type of inspection may also be useful with fiberscopes or similar apparatus that allow investigation of inner surfaces without disassembly.

Ultrasonic Techniques: Ultrasonic measurement methods are useful for measuring the thickness of a material. A high-frequency wave is introduced into the material using an ultrasonic transducer. This wave travels through the material, reflects off of the far side, and travels back to the original transducer or a second transducer placed nearby. An obvious limitation of this method is on curved metal surfaces where the reflection may not return to the receiver or may be dispersed in the medium. The time needed to travel this route combined with the velocity of the ultrasonic wave propagation in the material is then used to determine the thickness of the material. This technique can be used to monitor general thinning or localized thinning of the material.

There are problems with this method of corrosion monitoring. First, the material must be homogeneous to get accurate results. If it is not homogeneous, the propagation constant

of the energy will change depending on the location in the material. This will cause errors in the readings taken by the ultrasonic device. Second, layered materials will cause multiple reflections to return to the detector. These multiple reflections may be confused with the multiple reflections present in a single material when the energy reflects back and forth between the two walls of that material. Therefore, only the first layer may be accurately measured for thickness without complicated signal processing. Finally, water or anti-corrosion coatings may cause difficulty in the interpretation of the results because of either multiple reflections or inhomogeneity.

Eddy current examination: A wire coil with an ac current passing through it is placed near the surface of the metal structure. Eddy currents form in the material near the coil (also called a probe). These eddy currents penetrate into the metal at a distance proportional to the frequency of the ac signal. Lower frequencies will penetrate further with a theoretical maximum penetration depth of infinity at a frequency of 0 Hz. At higher frequencies, the depth of penetration asymptotes to approximately 1 mm, with a useful thickness measurement range up to 5 mm at a frequency of approximately 1 kHz. Therefore, thin structures are the best suited for investigation using eddy currents. The phase of the ac signal is dependent on the volume of the metal beneath the probe, and this phase is linear with respect to that volume. This technique is useful because it gives information about the inner surface of a skin without the need for disassembly [13]. However, the volume of metal under the probe could be a uniformly thick section of metal or a slightly thicker piece of metal with a corrosion pit or crack; there is no way to tell the difference between these two geometries. Also, access to one surface of the material is necessary, and this method is not used during operation of an aircraft due to bulky equipment and the need for a technician to operate and interpret data continuously.

Neutron Radiography: For this method, the material is irradiated with neutrons and a neutron detector is set up on the far side. The attenuation of the neutron beam is

dependent on the amount of hydrogen present in the material. Hydrogen is a byproduct of corrosion, and the amount of hydrogen present in the material is related to the amount of corrosion that has taken place. The attenuation of the beam of neutrons can then be used to calculate the amount of corrosion of the material.

Problems with this method include the need for a radioactive source for the neutron beam, the high cost of the equipment necessary for the system, and the inherent danger of radiation exposure to the operators. An advantage of this technique is the ability to detect corrosion in very thick structures, where other techniques cannot. It can detect the amount of remaining metal in a part, and the known initial thickness of the part is then used to determine the amount of corrosion. Again, this technique requires access to both sides of a structure and cannot be used during normal operation of the aircraft.

X-radiography: Essentially, this is taking X-rays of a structure. This technique can detect internal corrosion as well as general thinning of the material. The main problem with this technique involves the difficulty in interpreting the results due to varying paint thicknesses or uneven sealant and bonding surfaces. Also, only large material loss or cracking can be detected using this technique on large structures. Corrosion found in this manner is advanced enough to cause the replacement of the part. The sensors designed in this research can detect the beginning of the corrosion process, perhaps allowing repair of the structure without the need for replacement.

Acoustic Emission Techniques: There are two types of acoustic emission sensors currently used for corrosion monitoring. The first is an acoustic emission detector which is used to monitor the acoustic emissions that occur during the corrosion process. The level of these acoustic emissions is very small and requires expensive, sensitive detectors to monitor. Also, determining the exact location of the emissions requires multiple detection and complex algorithms to triangulate on the source of the emission. There is

also the possibility that random acoustic emission noise from other sources may be misinterpreted as corrosion by the sensor.

The second acoustic emission technique involves the detection of damage after it has occurred. For this type of acoustic detection, an external load is applied to the structure, and acoustic emissions caused by this load are monitored. Possible drawbacks to this method are the necessity of large loads on the structure to generate the emissions and the degradation to the structure caused by these loads.

Use of Witness Coupons: For this technique, a coupon of the material of interest is placed with the permanent material and periodically removed for examination. These coupons are typically placed where it is difficult to visually inspect the individual aircraft parts. Therefore, by placing and removing these coupons, the technicians can estimate the corrosion surrounding the area where the coupon was located. A simple form of examination is to measure the loss in mass of the coupon, thus estimating the corrosion rate for the entire structure. Estimated lifetimes of structures can be calculated from the information gained from the coupons. This technique is mainly used in large industrial plants but is not applicable to aircraft because obtaining the coupon would be similar to the current method of disassembly being used. Also, all of the possible corrosion sites would require individual coupons

Electrical resistance probe: The resistance of a material is directly proportional to its cross-sectional area and the amount of corrosion of the material. Therefore, monitoring the resistance of a material will give its cross-sectional area and the amount of corrosion the material has experienced

The main disadvantage to this technique is the necessity to penetrate the material to insert the probes. This could create locations of localized corrosion. Also, the probe

cannot detect localized corrosion sites because the output indicates an average value over the cross-sectional area for the material. This technique is also not used in aircraft.

Hydrogen probe: The main byproduct of many corrosion processes is hydrogen. A hydrogen probe consists of a thin foil (such as palladium) attached to an electrolytic cell. The cell produces a current through the foil which is required for the oxidation of the hydrogen. The current necessary for this reaction is measured and the corrosion rate is calculated from the current. This technique does not require any penetration of the material being monitored.

The disadvantages of this method include the necessity of high hydrogen diffusion rates through the material and the restriction to ambient temperature conditions. The equipment needed to make accurate measurements is also expensive.

Of these techniques, visual inspection and ultrasonic evaluation are the two most prevalent in use on aircraft today. The remainder are all under investigation or in use in limited areas. As noted in each of the individual descriptions, most of these approaches require the aircraft to be in the hanger to attempt corrosion detection. This was determined to be a shortcoming for corrosion monitoring. The optical fiber sensors developed here are intended to be used continuously during the operation of the aircraft or in the hanger. Additionally, it is obvious from reading the above descriptions that none of the above methods could be simply modified for use with optical fiber sensors. New optical fiber sensing techniques needed to be developed.

CHAPTER 3: FIBER OPTIC CORROSION SENSING

In order to monitor corrosion, the optical fiber sensor had to be designed to detect either the constituents that cause the corrosion process (predicting where corrosion might occur), the corrosion process as it occurs, or the byproducts of corrosion. Various types of optical fiber sensors were analyzed to determine the possibility of monitoring each of these three corrosion indicators. For the monitoring of the constituents that cause corrosion, humidity or liquid presence sensors were investigated. It was determined that this type of sensor might predict where corrosion would occur, but it would not identify the exact amount of corrosion present or even if corrosion had started, just that it might start. Therefore, this type of sensor was discarded as a possible method for monitoring corrosion.

Detection of the corrosion process would require the continuous detection of the effects of the chemical reaction that is corrosion in order to insure that the total amount of corrosion is known at all times. An alternative is a sensor that indicates only the effects of the process without giving detailed information on the rate or amount of corrosion. Methods to monitor the corrosion reaction include detecting the enthalpy of the reaction, or possibly monitoring the magnetic or electric fields caused by the flow of electrons created by the reaction, none of which are in practice today. The acoustic detection device described in Section 2.2 is another example of this type of sensor. These techniques are explored more fully in the following sections.

The final method, that of detecting the byproducts of corrosion, is the most commonly used type of sensor as demonstrated in Section 2.2; most of the existing techniques monitor material thinning or look for hydrogen or other byproducts of corrosion. The remainder of the optical fiber sensors described in the following sections are of the type that monitor the effects of corrosion. They monitor the changes in the byproducts of corrosion, such as metal oxides or a change in the metal thickness.

3.1 Enthalpy Monitoring

Enthalpy is defined as the energy released during a chemical reaction. A fiber optic sensor could be used to measure the temperature in a given area which could then be compared to the ambient temperature [14]. An increase in temperature would indicate that the reaction was taking place. This technique could utilize existing optical fiber temperature sensors to determine the enthalpy. The problem is that the aircraft will experience many other changes in temperature during operation. These other changes would probably make it impossible to determine when the corrosion reaction was occurring. Therefore this technique would need to be used only on the ground where ambient temperature could be monitored. The result of this restriction is that the majority of corrosion would be missed during aircraft operation because of the vast temperature fluctuations experienced in the aircraft environment during flight. This sensing technique was not given further consideration after the initial investigation.

3.2 Magnetic Field Detection

A typical fiber optic magnetic field detector utilizes a magnetostrictive material in conjunction with an interferometric fiber optic sensor to monitor the magnetic field fluctuations in a given region [15]. The presence of a field would indicate the presence of a corrosion reaction because the electron flow from the corrosion reaction generates a magnetic field. Other researchers are investigating such methods using other techniques

than fiber optics, but these investigations are generally in the initial stages and not used in practice. Although this approach may work well in a laboratory environment, use of the sensor on an aircraft with its high electro-magnetic environment did not appear feasible. The strength of the magnetic fields produced by the corrosion reaction is very small compared to that of the general electro-magnetic environment surrounding aircraft. Additionally, at this time, the fields are so small that optical fiber sensors are not sensitive enough to provide any useful information about this field. This sensor was therefore removed from consideration.

3.3 Signature Testing

A signature, in this case, is defined as the vibrational response of a structure to a known impulse. Optical fiber vibration sensors are set up to monitor the vibrational response of the structure. The structure is tested before each use (or at the beginning of its lifetime), and subsequent tests during the lifetime will give varying signatures due to changes in the structure. Corrosion of the structure is one of the factors that will change the signature. Therefore, these signature tests can be used to monitor corrosion damage. At this time, this type of monitoring technique has been considered by scientists, but is not in practical use.

An example of a typical optical fiber vibration sensor is the elliptical-core two-mode fiber sensor [16]. This sensor is a very special type of interferometer. The interference occurs between the two lowest order modes of the optical fiber. This is different from the typical scenario where one source is divided into two legs of fiber and then recombined immediately preceding the detector. The two lowest order modes are isolated by using the elliptical core fiber at a specific wavelength. Essentially, a single-mode elliptical-core fiber is injected with light at a wavelength slightly below the single-mode cutoff wavelength. This allows two modes to propagate. The elliptical-core fiber is necessary to separate the polarization states of the first two modes, and the even/odd

degeneracies of the second mode. The elliptical-core fiber not only restricts the light to one polarization state, it prohibits the propagation of the second order odd mode, which causes a great amount of noise in the system when present. When the optical fiber is strained, the path length difference between the two modes changes, creating a change in the intensity pattern at the output.

If several of these sensors are placed in known orientations in or on the structure to be tested and the structure is impacted in a known, repeatable manner, the signature of the structure can be monitored. This signature could be measured in the frequency or time domains equally as well with these sensors. To acquire a frequency analysis of the output, a fast Fourier transform is performed on the time domain output. The signature is then compared to an original signature taken when the structure was new, or at the beginning of the use of the structure. The amount of difference between the two signatures will determine the changes in the structure.

This technique is a universal technique, i.e. it gives information about the entire structure for each test. Unfortunately, this also means that information about specific areas is difficult to extract from the data. Also, this technique will measure all changes caused to the structure, not individual problems such as corrosion. Again, this makes it difficult to determine the information about a specific effect on the structure.

Figure 3.1 is an example of the setup required for a typical elliptical-core two-mode fiber sensor. The sensing region in this figure would be the length of fiber attached to or embedded in the structure. The sensor actually measures a change in length of the structure integrated over the length of the sensing region. The strain, which is caused by the vibrations, is the change in length of the sensor divided by its gage length. The smallest detectable change in length for this sensor is approximately $1\ \mu\text{m}$ which corresponds to a very small strain for large gage lengths.

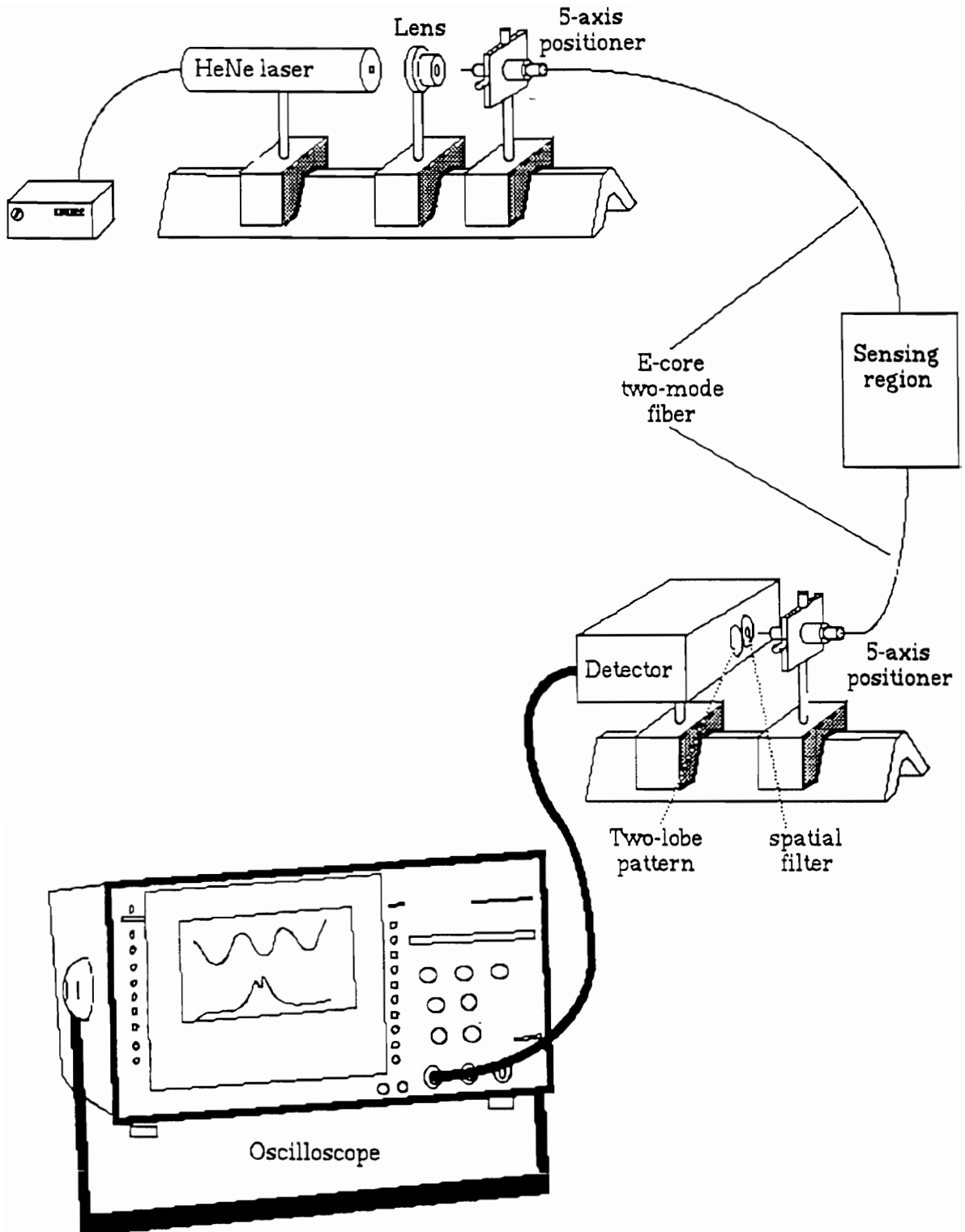


Figure 3.1. A schematic of an elliptical core two-mode optical fiber sensor setup.

Some problems associated with this technique include the possibility of certain vibrational modes being overlooked because a specific mode shape causes a cancellation of some of the strain along the optical fiber. Therefore, only certain vibrational modes will be available for investigation. Also, it is very difficult to multiplex these sensors due to the stringent requirements placed on the input polarization and detection techniques. This means that each sensor would probably require its own source and detector.

Although much information could be gained from this type of sensor, the information would be very general. Specific sites of corrosion would not be easily located which means that intensive dismantling of the aircraft would still be necessary and downtime would not be minimized. Therefore, this sensor was not pursued as a practical sensing alternative for this research.

3.4 Acoustic Emission Monitoring

This is similar to the technique described in Section 2.2. The difference is that optical fiber sensor systems would be used to detect the acoustic emissions. These fiber sensors can become a permanent part of the material or structure thus providing continual monitoring of acoustic information. There are currently very accurate optical fiber acoustic emission sensors in development at the Fiber & Electro-Optics Research Center (FEORC).

The sensitivity requirements for the detection of acoustic emission limit the possible sensor types to the interferometric sensors, the most sensitive of the optical fiber sensors. Some possible techniques include the extrinsic Fabry-Perot interferometer (EFPI) sensor [17], Mach-Zehnder interferometers, and Michelson interferometers.

The EFPI sensor is set up in the reflective mode. There are two reflections present at the air-gap: one each at the glass-air interface at the front end and at the air-glass interface at the far end (see Figure 3.2). The two reflected signals differ in phase by an amount proportional to the air-gap distance. This difference in phase causes the typical interference fringes found in fiber optic interferometers. The signal processing unit must monitor the output and count the fringes that the sensor produces and, for the highest accuracy, determine the intensity level “inside” a fringe. Special techniques may also be necessary to determine whether the gap is increasing or decreasing because the fringes look the same in both cases. Tran et al. [18] have demonstrated the use of EFPI sensors for the monitoring of surface acoustic waves. The EFPI sensor is attached to the surface of a material and surface acoustic waves cause a variation in the air gap length thus causing a change in the output signal. Figures 3.3 and 3.4 show a Mach-Zehnder interferometer and a Michelson interferometer, respectively. Some recent work at FEORC has concentrated on the use of the EFPI sensor. It may even be possible to use three or more sensors to triangulate the location and initial intensity of the acoustic emission.

The original premise of this work was to find an inexpensive optical fiber corrosion sensor that could be used throughout an aircraft. The use of interferometric sensors such as the EFPI requires the use of laser diodes and complex signal processing units. These systems are much more expensive than intensity-based techniques. Also, for the acoustic emission sensing technique, a triangulation method must be used to determine the precise location of the corrosion causing the acoustic emissions. Again, this adds complexity and expense. Therefore, this sensing technique was initially placed at a low priority while other, less expensive techniques were investigated. Later, the technique was discarded when the aluminum-clad sensors showed much promise.

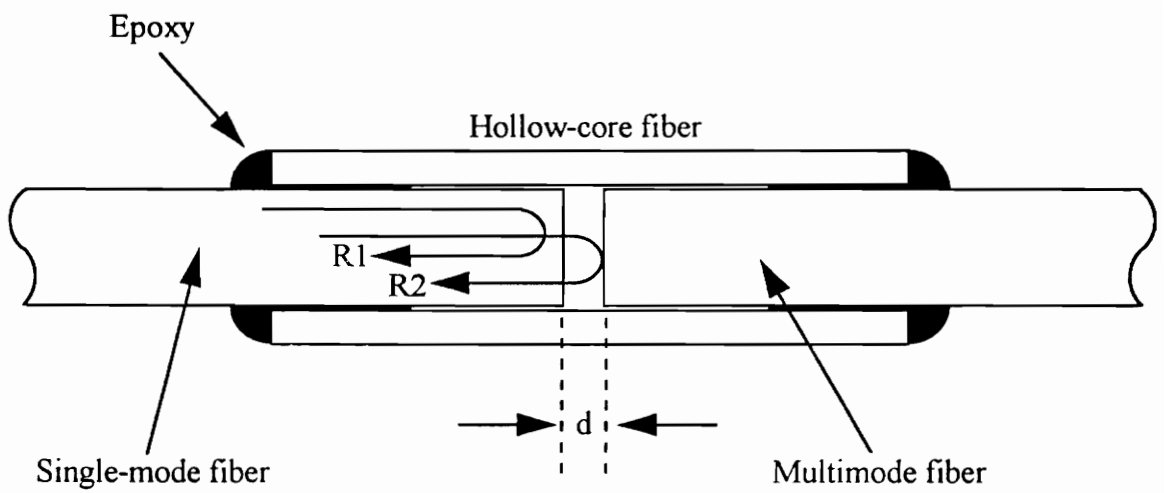


Figure 3.2. A schematic of an EFPI sensor.

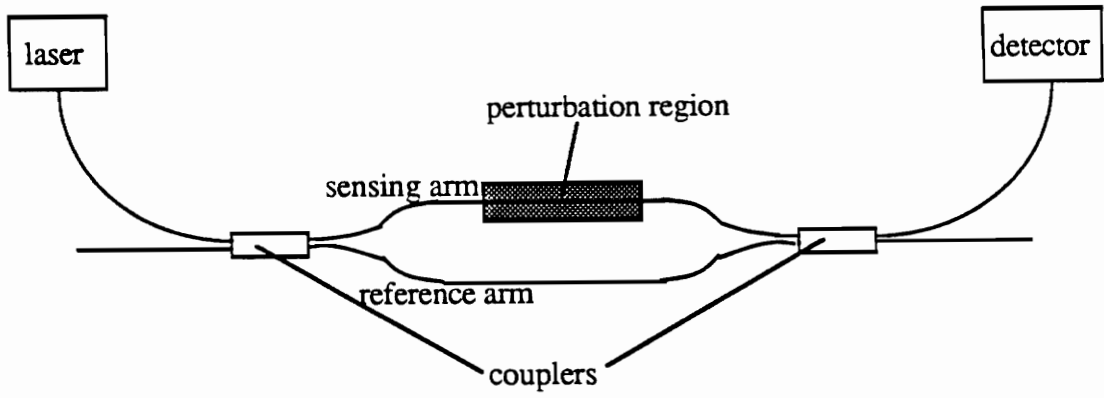


Figure 3.3. A Mach-Zehnder optical fiber interferometer.

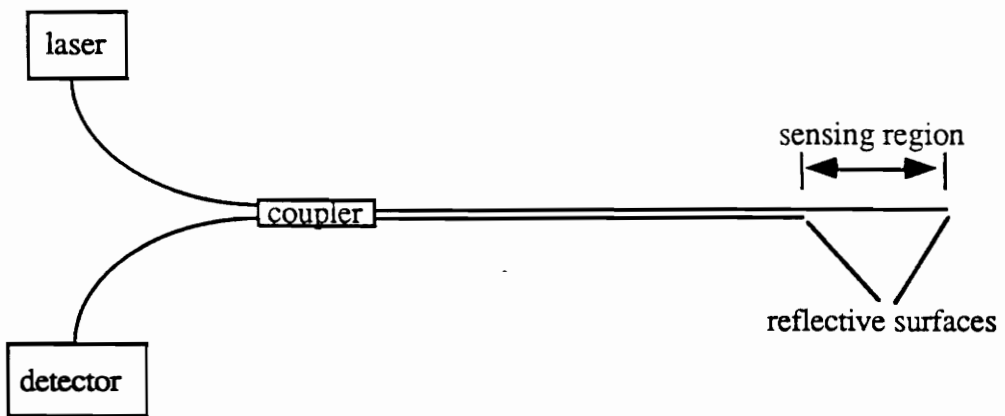


Figure 3.4. A Michelson optical fiber interferometer.

3.5 Reflection Techniques

One of the main sources of visual information indicating the presence of corrosion is a change in the appearance of the material that is corroding. This change takes the form of both a color change as well as a change in the shine, or reflectance, of the aluminum. This appearance change indicates two possible methods for monitoring corrosion: monitoring the intensity of the reflectance of the aluminum and monitoring the spectral reflectance of the aluminum.

3.5.1 Spectral Reflectance Monitoring

The spectral reflectance method was tested to determine its feasibility since, to our knowledge, no one had attempted this before. White light was reflected from both corroded and uncorroded aluminum samples received from Boeing Defense and Space Group. The light was transmitted to the metal samples using a 100/140 micron multimode optical fiber and a detector was used to monitor the light returned from the reflections as shown in Figure 3.5. A spectrum analyzer was used to investigate the spectra of the reflected signals. Initial test results, shown in Figure 3.6, demonstrated the expected intensity drop with the presence of corrosion, and there appeared to be certain wavelength regions which may have had more dependence on the corrosion than others. These initial tests were conducted over a wavelength range of 500 nm to 1500 nm. The results also showed that the power level returned to the spectrum analyzer was too small to make highly accurate spectral measurements. These results indicated that a larger core fiber, or possibly a fiber bundle, would be necessary to bring more light to the aluminum and increase the returned signal level.

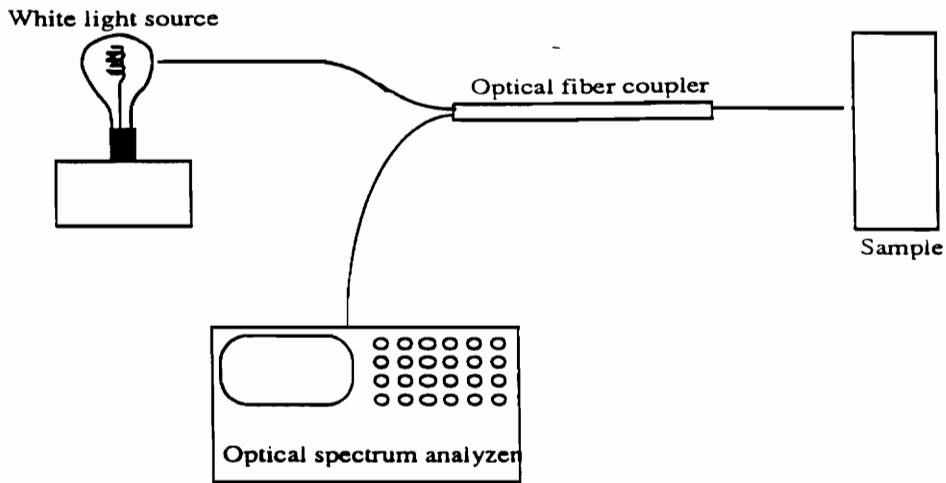


Figure 3.5. A schematic of the spectral reflectance setup.

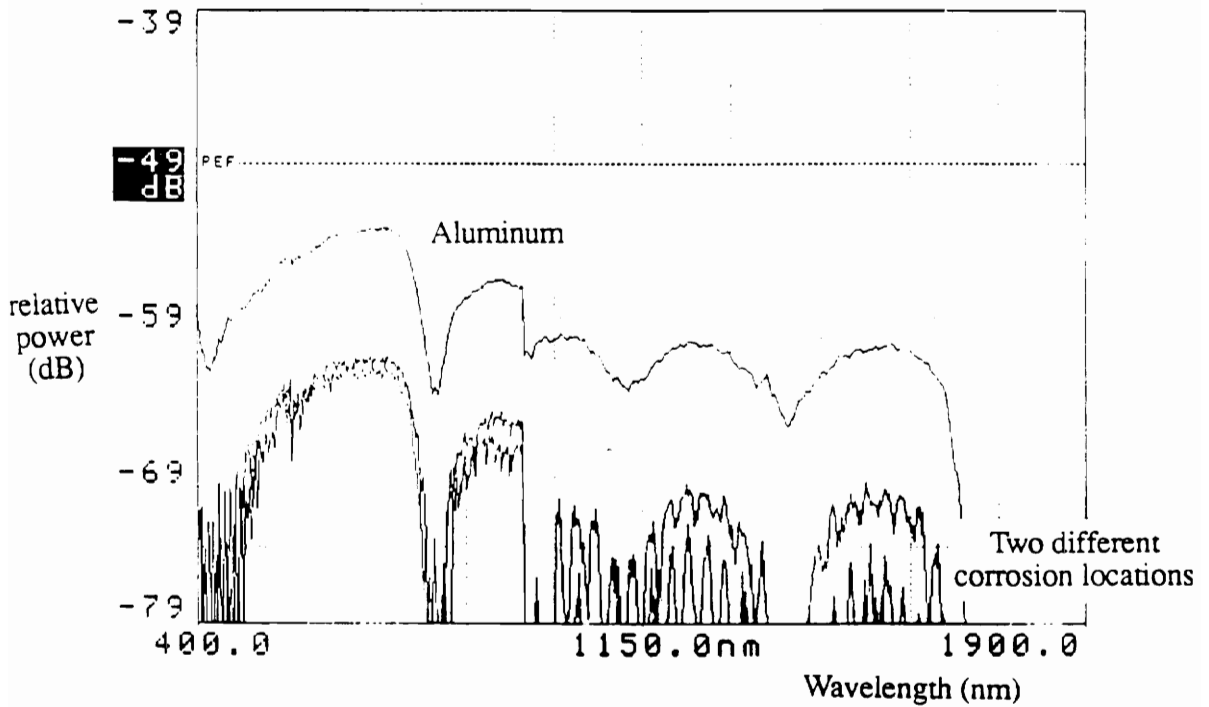


Figure 3.6. Spectrums for reflected signals from pure and corroded aluminum samples.

Further tests were conducted using a fiber bundle to increase the power level available at the spectrum analyzer. Also, the next tests were used to investigate the regions around 900 nm and 1400 nm, which seemed to be more dependent on corrosion. Unfortunately, the changes in these regions also showed a fairly uniform decrease in intensity as the amount of corrosion increased. There was no particular phenomenon that could be used to quantify the corrosion level other than overall intensity drop. There were no regions which showed more or less intensity loss with corrosion than the rest of the spectrum. There were no spectral notches or spikes that changed widths or shapes with corrosion. These results indicate that the corrosion process seems to only cause changes in the overall intensity of the reflections from the corroded surface and that these changes are not spectrally dependent. The idea of spectral reflectance was therefore removed from consideration for use as a practical corrosion monitoring technology.

3.5.2 Extrinsic Pure Reflection Monitoring

The setup for this type of sensor is identical to the setup for the spectral reflectance sensor shown in Figure 3.5 with the exception that the source is not restricted to white light. For our tests, a HeNe laser was used as the source. In this case, the reflection from the aluminum is monitored for intensity changes. To initiate the corrosion process on the metal to be monitored, a corrosion test cell was designed.

The test cell consists of a glass container with a Plexiglas lid and a heating pad placed underneath as shown in Figure 3.7. The heating mat increases the temperature in the chamber to increase the corrosion rate. By adding heat, the overall energy level of the molecules is raised, allowing the reaction between the metal ions and the ions in solution to more easily occur, thus speeding the overall reaction. The bottom of the cell is filled with a small amount of water, and a small amount of salt (NaCl) is added to form ions in the solution. These ions also speed up the corrosion process, as described in Chapter 2.

The mixture of water, salt and heat in the enclosed container forms a highly humid environment conducive to corrosion. A computer-controlled detection system was built to monitor the outputs of the system over long periods of time since the corrosion process is a slow process.

The signal processing system, shown in Figure 3.8, used a HeNe laser as a source which was fed into an 8x8 coupler to allow source monitoring and seven test channels. Two different types of sensors are shown in this figure, the reflective sensors discussed here, and the aluminum coated fiber discussed in Section 3.6.1. For the reflective-type sensor, an additional 2x2 coupler was used to monitor the return reflections. For this system, the maximum amount of reflective sensors that could be monitored simultaneously was three, leaving four channels for transmissive sensors. The signal from the detector was amplified by an amplifier with variable gain so that the output range could be matched to the required input range of an analog-to-digital converter (A/D) board. The signal was converted in a multi-channel A/D board and fed into the computer. A computer program was written which poled the channels serially at given time intervals. The computer could therefore monitor the return signals over an extended period of time.

As is shown in Figure 3.8, the reflective sensor described in this section consists of the end of the optical fiber lightguide positioned facing the aluminum block in the corrosion chamber. As corrosion occurred, the reflectivity of the aluminum decreased and the power level returned to the fiber decreased. Figure 3.9 shows the output of a typical sensor versus the number of days in the corrosion chamber. Visually, the aluminum was polished before corrosion, and as the time progressed, the polish turned dull, and eventually the surface became rough as is indicative of corrosion. Therefore the power drop is caused by the corrosion.

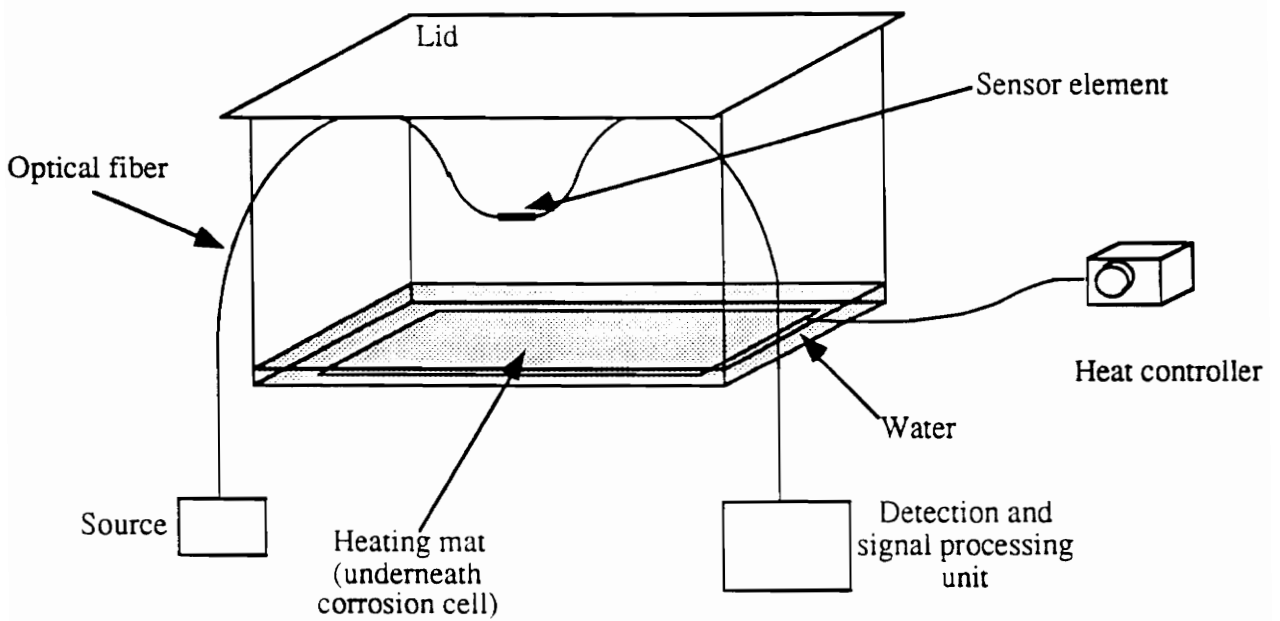


Figure 3.7. A schematic of the corrosion monitoring test cell.

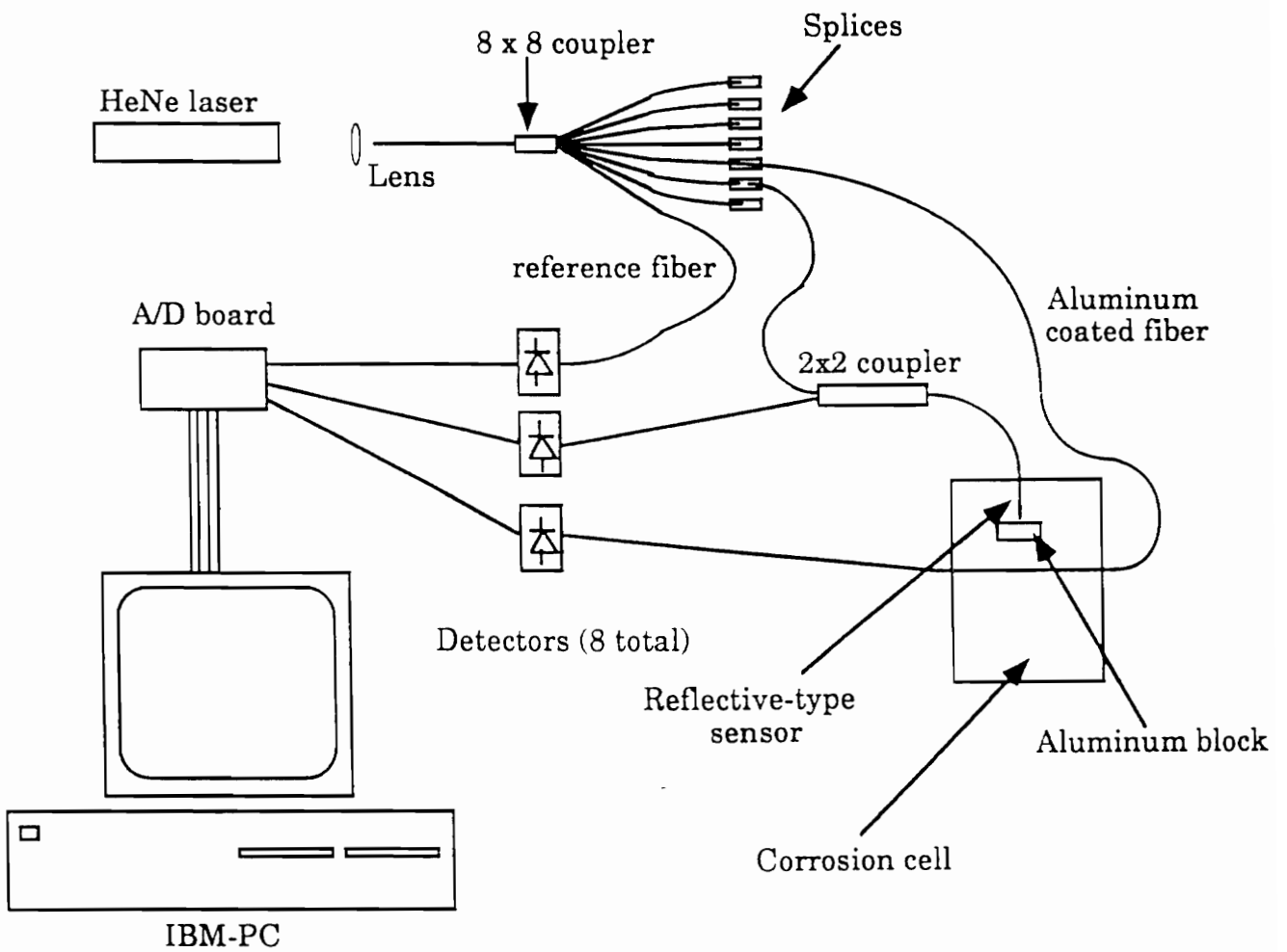


Figure 3.8. A schematic of the sensor support system for corrosion monitoring.

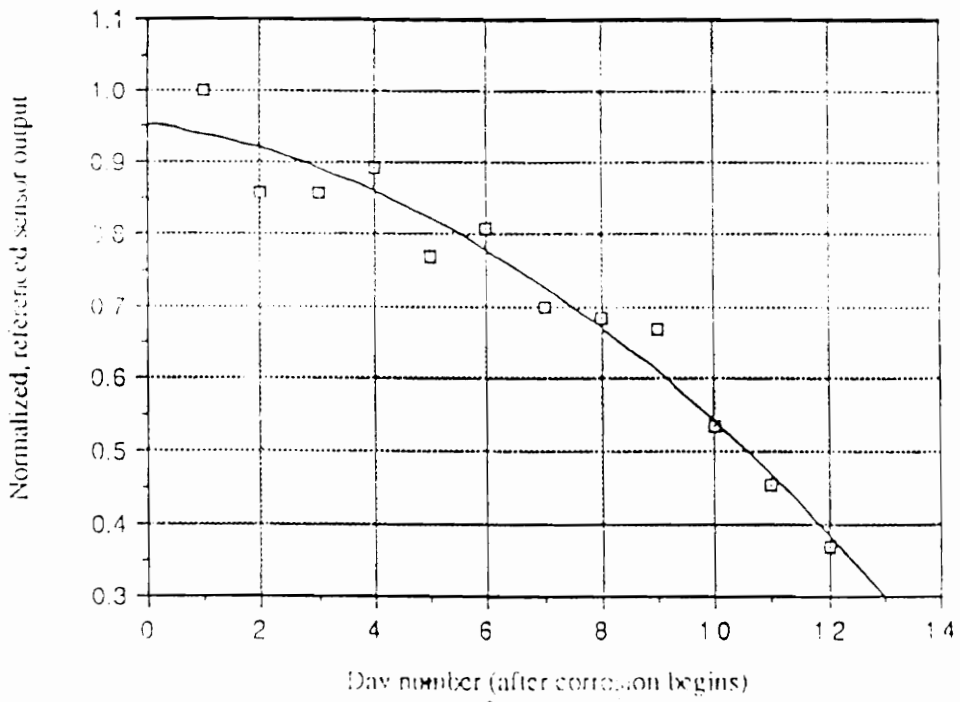


Figure 3.9. A plot of the extrinsic type reflection sensor versus time.

The problems with this sensor are that a very small change in corrosion caused a large change in the output power. Also, for standard usage, aluminum is regularly covered with a sealant or paint. This would make it difficult to determine exactly how much corrosion has occurred. Since some surface change is accepted as normal and the parts are not considered damaged until a large amount of corrosion has occurred, this type of sensor may not be very useful. Additionally, the necessity of placing the fiber facing the metal surface did not appear practical in an aircraft. The fiber would continually be in jeopardy of breakage, and particulate matter could interfere with the signal as it travels to the aluminum and back. Additionally, many of the surfaces in an aircraft are covered with sealants or paint making it impossible to look at the aluminum surface without removing the coating and defeating the original purpose of the coating, i.e. protecting the aluminum. This sensor was discontinued in favor of the intrinsic reflective sensor described in the next section.

3.5.3 Intrinsic Pure Reflection Monitoring

The intrinsic reflection sensor is very similar to the extrinsic reflective sensor except that the metal to be monitored, in this case aluminum, is coated onto the fiber endface. The reflection from this coated film is monitored for changes which would indicate corrosion. Theoretically, the reflections can be described by the Fresnel relations for a three layer system at normal incidence [20]. The reflectivity is given by

$$R = \left| \frac{r_{12} + r_{23}e^{2i\beta}}{1 + r_{12}r_{23}e^{2i\beta}} \right|^2, \quad (3.1)$$

where r_{12} , r_{23} , and β are given by

$$\begin{aligned}
r_{12} &= \frac{n_1 - n_2}{n_1 + n_2}, \\
r_{23} &= \frac{n_2 - n_3}{n_2 + n_3}, \\
\beta &= \frac{2\pi}{\lambda} n_2 h,
\end{aligned}
\tag{3.2}$$

and n_1 , n_2 , n_3 equal the indices of refraction for the core of the fiber, the metal film, and the surrounding medium (air), respectively. λ is the wavelength of the light used and h is the thickness of the film. The index of refraction of the film, n_2 , is a complex value because the film is aluminum.

The above equations were programmed into MATLAB[®] and the results plotted in Figure 3.10 for four wavelengths. The curves show the variation in reflectivity versus film thickness. The wavelengths chosen for this curve are 633, 850, 1300, and 1550 nm, those typically used in optical fiber sensors. As can be seen, the shapes are relatively similar for the various wavelengths and the results should therefore be representative for any chosen wavelength. This curve shows that a 20 nm thick coating will cause nearly 100 % reflectance. Since the change from complete reflectance to complete transmission occurs as the film thickness changes from 20 nm to 0 nm, a corrosion switch is a more viable alternative than a device to measure the precise level of corrosion. By coating much thicker amounts of aluminum onto the fiber the corrosion process will decrease the thickness of the coating over time, but the power will change only when the thickness reaches approximately 20 nm. Therefore, no change will occur until the aluminum is almost completely removed. This would therefore act like a switch indicating corrosion has removed enough aluminum to cause a change in the sensor. In this case, the original thickness would be gone, and the part may need replacement.

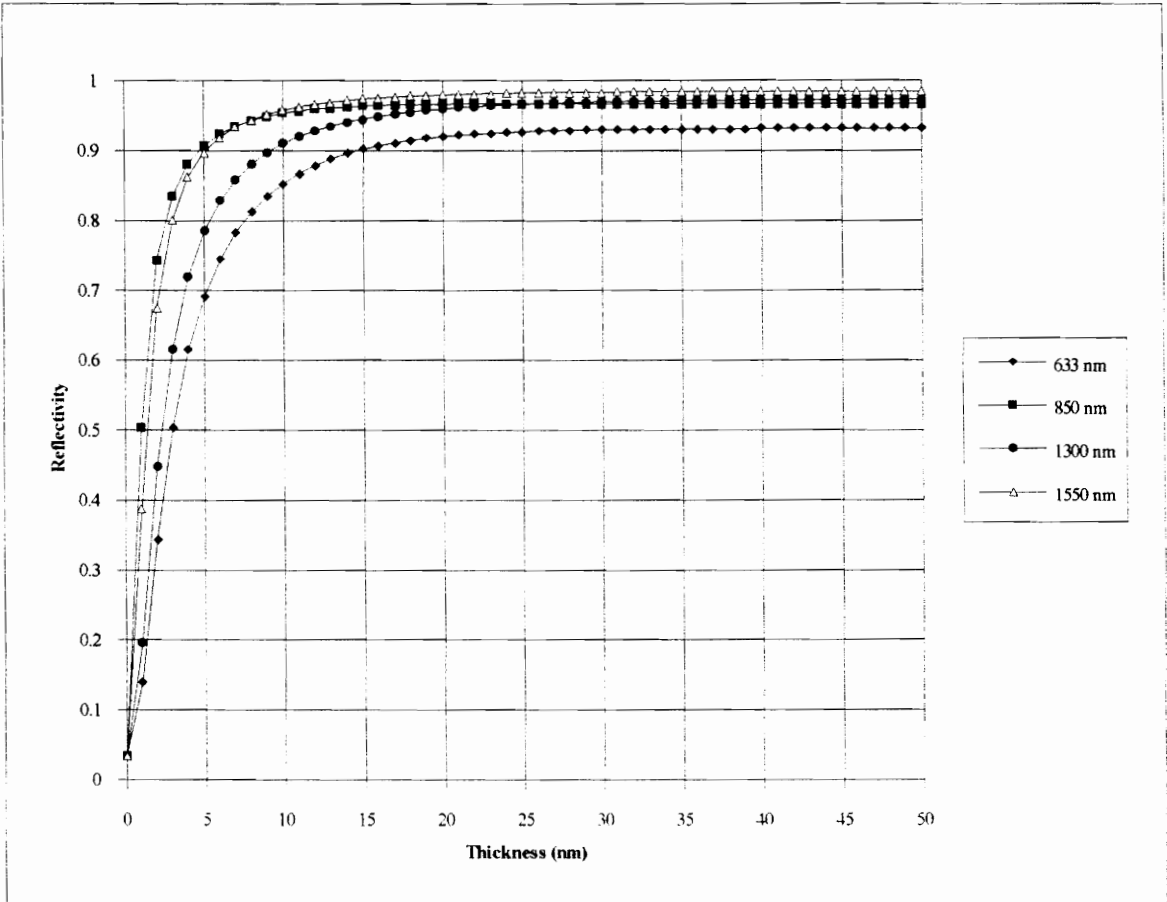


Figure 3.10. A graph of the reflectance of an aluminum thin film for several wavelengths.

Experiments were performed to test this sensing technique using a sodium hydroxide (NaOH) test cell. As described in Chapter 3, the test cell uses NaOH because it greatly increases the rate of the corrosion reaction. Again, a detector is used to monitor the reflection coming from the aluminum coating. A second detector is used to monitor the source for fluctuations as shown in Figure 3.11. The outputs are recorded and normalized to determine the change in power from the sensor. Figure 3.12 shows the test results for two aluminum end-coated sensors. Notice that the entire test took approximately 40 minutes. The same test without the presence of the NaOH would likely take a number of days to complete. The large fluctuations in the output power can be attributed to the instability of the test setup. The table on which the experiments were performed was not isolated from vibrations and the sensor was not held stable in the NaOH.

Although this sensor shows promise, there are some problems with the sensor. It can only monitor one small point approximately the size of the fiber core. Many such sensors would be required to cover a large area of aluminum. As described above, it does not provide continuous information about the corrosion process; it can only determine when corrosion has thinned the metal coating to 20 nm or less, like a switch. It is, however inexpensive and relatively simple to fabricate. This sensor was therefore considered a viable option for corrosion sensing, but the aluminum-clad sensor proved itself superior as will be seen later in this dissertation. Therefore, this sensor was not developed further than shown in this section.

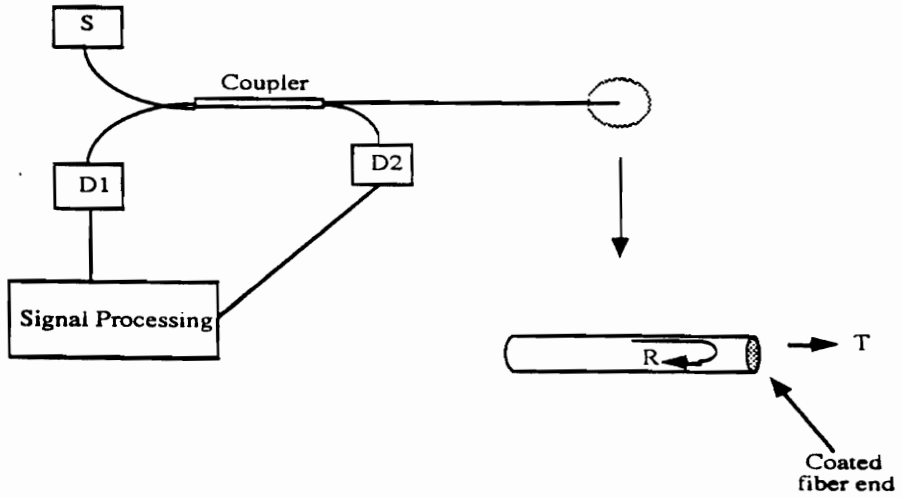


Figure 3.11. A schematic of the intrinsic reflection sensor, S - Source, D1 - Sensor detector, D2- Monitor detector, R- Reflected light, and T - Transmitted light.

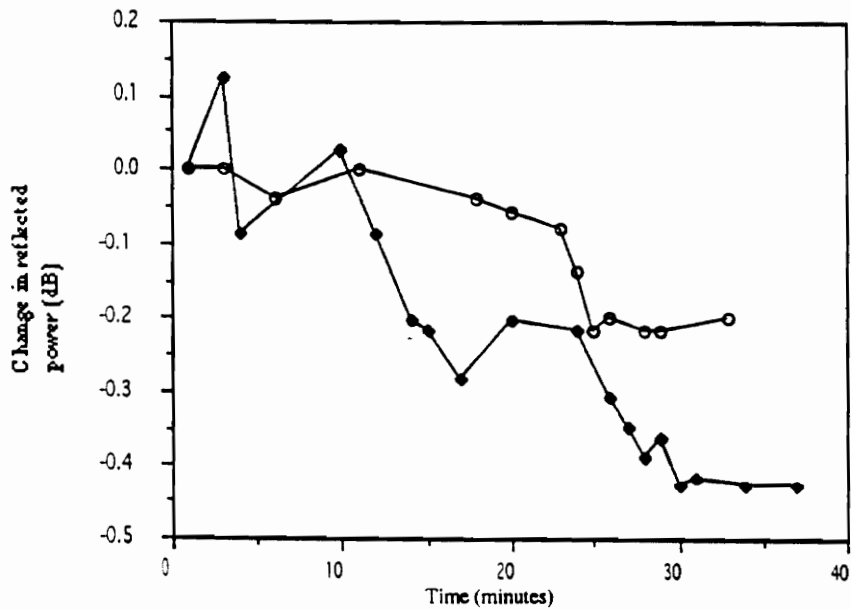


Figure 3.12. Reflected power versus time for two aluminum end coated fiber sensors.

3.6 Transmission Techniques

Transmissive sensors are defined as sensors in which the light propagates through the sensing region to the far end of the fiber where it is detected and analyzed. The following three sensors are all classified as transmissive sensors. Since the light propagates through a sensing region, these sensors are also known as integrating sensors. The term ‘integrating’ refers to the phenomenon where perturbations along the sensing region cause an additive change in the sensed parameter (i.e. phase, intensity, polarization, etc.) at the output end of the fiber. The sum of the effects of the perturbation at every point along the sensing region is included in any output change.

3.6.1 Metal Coated Optical Fiber Sensor

The first transmissive sensor investigated was a simple aluminum-coated optical fiber. The thought process behind this sensor was that a change in the coating would affect the light propagating in the core of the fiber. A 100/140 micron core/cladding optical fiber with a coating of aluminum on its outer cylindrical layer was spliced between two acrylate-coated 100/140 fibers. The sensor was placed in the corrosion cell described in Section 3.5.2 and left to corrode over time. The output was monitored for three weeks with very little change in power observed. The sensor was removed from the chamber, inspected and found to have corroded significantly. The lack of change in optical power indicates that the light is too tightly confined to the core to be affected by changes in the fiber coating. The silica cladding for the fiber was 10 micrometers thick, and as with most multimode fibers, the power carried in the cladding is minimal. Further testing consisting of removing the aluminum completely confirmed that the light is well confined in the core and not affected by changes outside the cladding. Therefore, this sensor was discarded in favor of the metal-clad sensor described in Section 3.6.3.

3.6.2 Surface Plasmon Sensing Technique

A second transmissive sensing technique is that of the surface plasmon-based sensor. A surface plasmon is the oscillation of the electrons which exist at the surface of a solid material (generally a metal) containing free electrons. An optical fiber is modified so that a metal film can be applied on the core of the fiber or over a very thin cladding (typically less than 1 micron). Light traveling through the modified region will transfer to a surface plasmon if the metal thickness, index of refraction of the outside of the metal, and wavelength of the light are properly matched. Since the formation of the surface plasmon is dependent on the index of refraction of the outer material and the metal thickness, corrosion sensing is possible. This technique was investigated further and the results of this investigation are presented in Chapter 4.

3.6.3 Metal-Clad Optical Fiber Sensor

The metal-clad optical fiber corrosion sensor consists of a glass core and a metal cladding in the sensing region. Outside of the sensing region is standard optical fiber to bring the light to and from the sensing area. The light in the core is strongly affected by the metal and changes in the metal. The length of the sensor is limited by the loss in the sensing region to less than 250 cm, and it operates more efficiently at lengths less than 50 cm. Since the sensing region is not truly a waveguide, the light entering it experiences a great deal of loss before exiting on the far side. As the metal is removed due to corrosion, the loss in the sensing region decreases and the output level increases. This behavior is the opposite of that of most intensity-based sensors and removes the possibility that bending or source power drops will cause a misreading from the sensor. This sensor proved the most promising of all the sensors examined and is explained in detail in Chapter 5.

CHAPTER 4: SURFACE PLASMON SENSOR

As mentioned in Section 3.6.2, a surface plasmon is the oscillation of the electrons which exist at the surface of a solid material containing free electrons. Surface plasmons are formed at a dielectric-metal interface when an optical wave is incident on the metal surface. If the optical field has the proper momentum, an electron plasma vibration is formed which has the same momentum as the incident optical wave. The most common and most useful configuration for the generation of surface plasmons has a thin metallic film coated on the dielectric material. The film is then covered with a second dielectric, commonly called the sample. If the wavelength of the light, indices of refraction of the two dielectrics, and the thickness of the metal meet the proper conditions, a surface plasmon will form that is supported by both metal-dielectric surfaces. This type of surface plasmon is known as a thin film surface plasmon.

4.1 History

Surface plasmons have been studied for over twenty years in the analysis of chemical reactions and for index of refraction monitoring. The first thin film surface plasmon device was developed by E. Kretschmann and A. Otto in the late 1960's [21]. This device utilized a prism with one surface coated with a metallic film. The film material and thickness were chosen to match the momentum of the incoming optical wave with the surface plasmon momentum. The device has come to be known as the Kretschmann prism assembly. This device is described in a theoretical paper written by Raether [22].

For this device, the optical wave is injected into the prism at a certain angle, as shown in Figure 4.1. Only the TM polarization state has an electric field that extends into the metal and therefore only the TM polarization state can form a surface plasmon. The surface plasmon is formed if the vector of the optical wave along the surface matches the vector of the surface plasmon. As shown by Raether [18], the surface plasmon wave vector relationship to the incoming optical wave vector is given by

$$K_{sp} = K_0 \left(\frac{1}{n_s^2 + n_m^2} \right)^{-1/2}, \quad (4.1)$$

where n_s is the index of the sample, n_m is the index of the metal, and K_0 is the free space wavevector of the incoming optical wave. The wavevector of the incoming optical wave along the surface of the metal is given by

$$K_x = K_0 n_p \sin \theta, \quad (4.2)$$

where n_p is the index of the prism. If K_x and K_{sp} are equal, then a surface plasmon will form. These formulas also demonstrate how sensing can be performed using the surface plasmon phenomenon. As the outer index, n_s , changes or the index of the metal, n_m , changes the amount of coupling to the surface plasmon changes. By varying the angle to maximize the coupling to the surface plasmon, n_s or n_m can be measured.

The first uses of the Kretschmann prism assembly was in the measuring of the dielectric constant of silver films [23]. Others have used this method to measure the index of other metals including rare earth metals [24]. Additionally, applications of the prism-based surface plasmon assembly are in monitoring biochemical reactions. By adsorbing half of a biochemical pair, such as a protein, the presence of the second half can be detected. If the second half of the pair is present, it reacts with the first half and changes the sample index, thus indicating the presence of the second half of the pair [25].

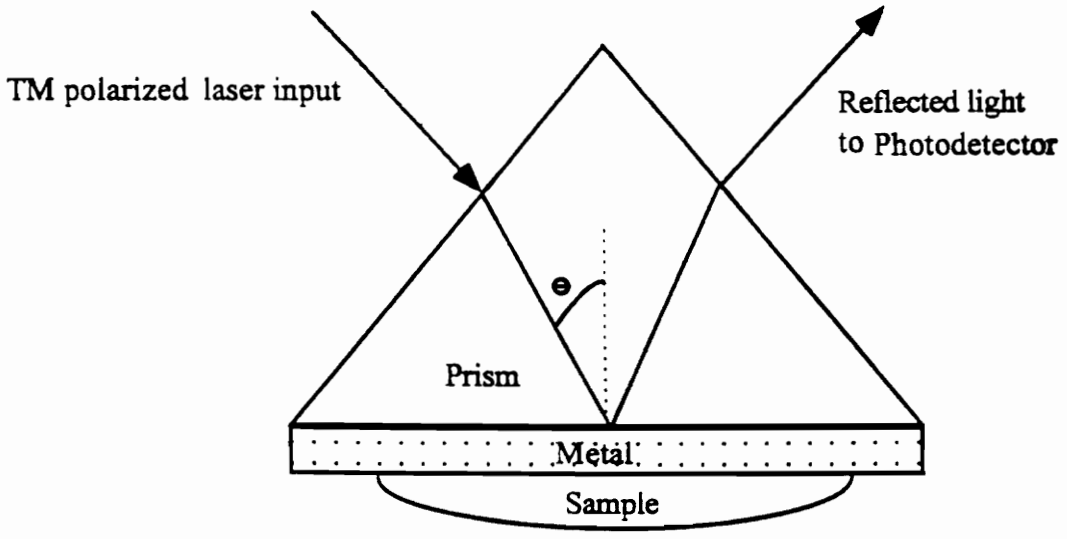


Figure 4.1. Kretschmann prism assembly for surface plasmon generation.

With the advent of optical fiber sensors, an alternative method for creating surface plasmons was introduced. Since the light propagating in the optical fiber travels essentially parallel to the core/cladding surface, it was discovered that a modification of the fiber can create an arrangement capable of forming surface plasmons. By polishing a single-mode optical fiber into its width to within approximately 1 micron of the core of the fiber and coating this polished section with a thin metal film, the optical energy in the TM mode can be coupled to a surface plasmon in the metal film [26].

4.2 3-Layer Surface Plasmon Resonance

Optical fiber surface plasmon devices were first investigated for use as optical fiber in-line polarizers. The setup in Figure 4.2 was used to take unpolarized light in a single-mode fiber and transfer a portion of the TM polarization state to a surface plasmon, leaving mostly the TE polarization in the fiber [26-34]. The amount of TM energy transferred to the surface plasmon is always dependent on the geometry of the device and the material characteristics of the film, fiber, and outer material. To use this phenomenon in a sensor, the TM polarization is monitored as the outer index or properties of the metal film are changed.

4.2.1 Theoretical Analysis

Since the metal film is effectively a waveguide for the surface plasmon in this geometry, waveguide analysis has been used to derive the relationship between the materials, geometry, and surface plasmon resonance condition. The geometry is approximated as a planar waveguide as described by Johnstone et al. [33]. The metal is treated as the core and the fiber and sample are the two cladding materials. The only twist to this analysis is that the index of refraction of the metal is approximated as an imaginary index for simplicity [33]. The real index of the metal is ignored in most analyses. The use of this

approximation is validated in the literature [33]. After performing the waveguide analysis, the dispersion relation for the surface plasmon has been shown to be [33]

$$k_0 \left(\left(\frac{\beta}{k_0} \right)^2 - n_2^2 \right)^{1/2} = \tanh^{-1}(A_1) + \tanh^{-1}(A_3), \quad (4.3)$$

where $k_0 = 2\pi/\lambda$, λ is the wavelength of the light, β is the propagation constant of the light, t is the thickness of the film, and n_2 is the index of refraction of the metal film. A_1 and A_3 are given by the equation

$$A_i = \frac{-(n_2/n_i)^2 (n_e^2 - n_i^2)^2}{\sqrt{(n_e^2 - n_2^2)}}, \quad (4.4)$$

where $n_e = \beta/k_0$ and n_3 and n_1 are the indices of refraction of the material above and below the film, respectively. For a polarizer, the film thickness is calculated to maximize the coupling of the TM mode [33].

This theoretical analysis was repeated by William Bender in his doctoral dissertation [3]. The dispersion relation calculated by Bender is plotted in Figure 4.3. An interesting conclusion that can be drawn from the dispersion relation is that the sample index of refraction must be greater than 1.41 in order for surface plasmons to be formed for the conditions of a typical single-mode optical fiber (i.e. core index of approximately 1.5). At index values less than 1.41, the thickness has an imaginary component which represents an impossible solution to the equation. The effect of this will be discussed at the end of the next section.

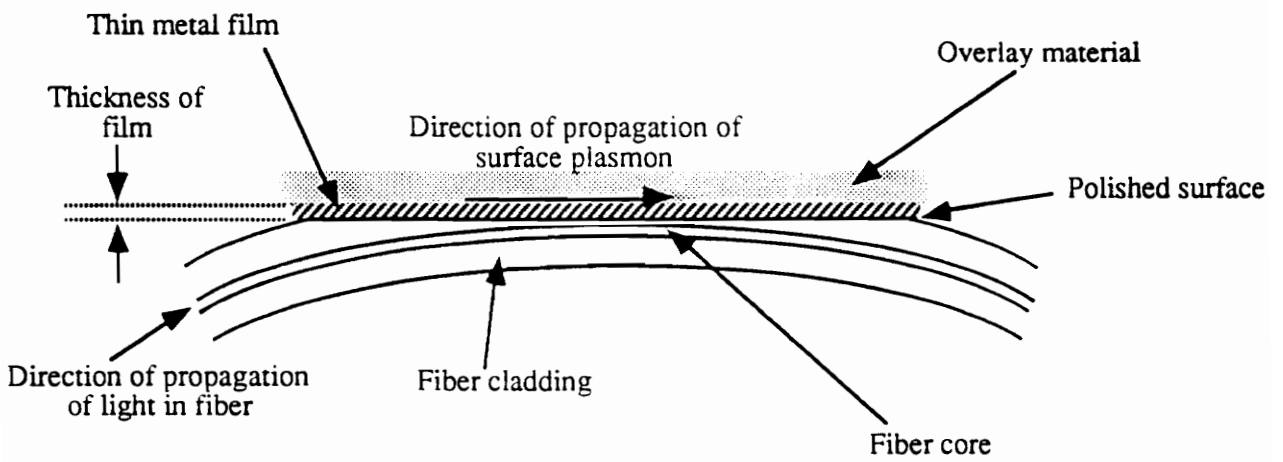


Figure 4.2. Schematic of a fiber optic surface plasmon device.

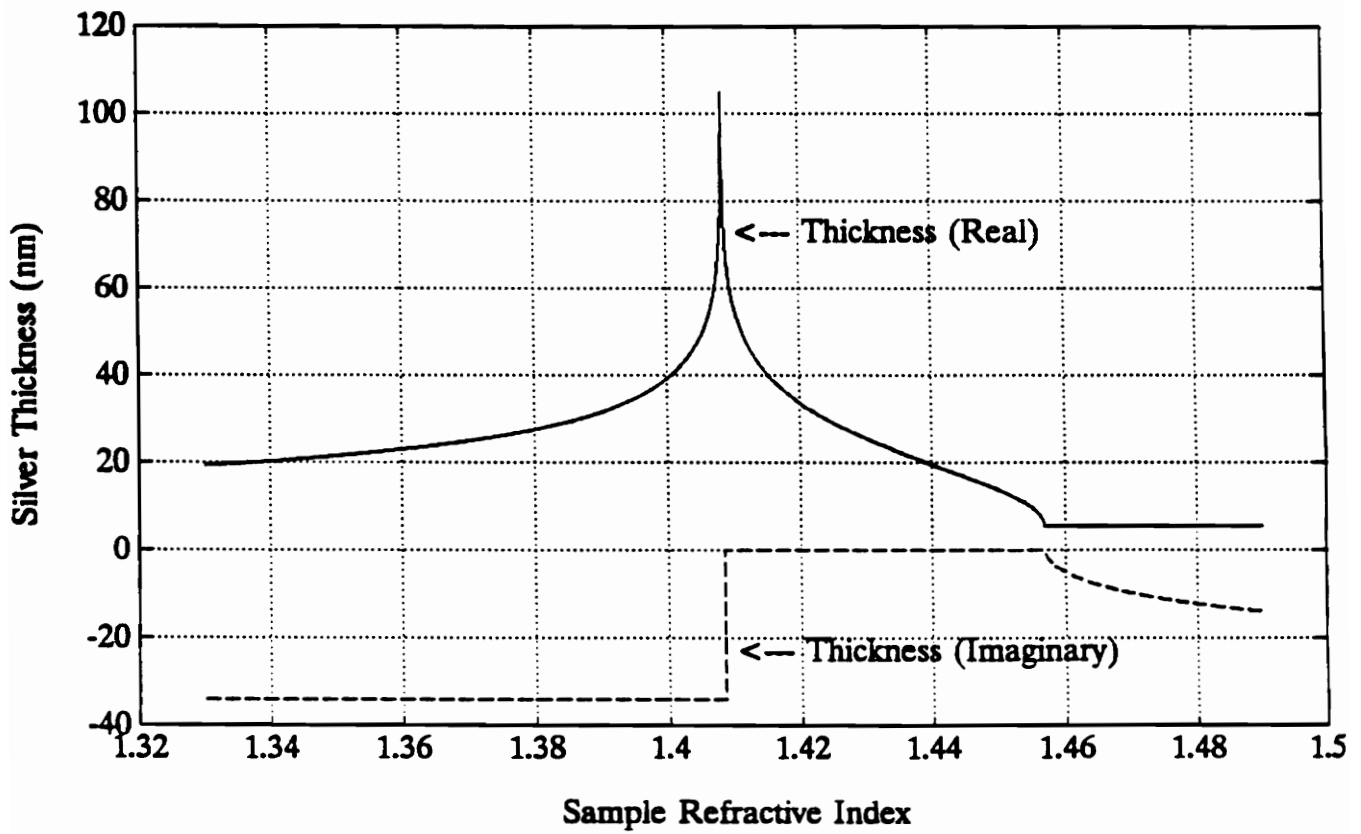


Figure 4.3. Dispersion plot for the 3-layer system [3].

4.2.2 Experimental Results

As described in Bender's dissertation, the sensor was fabricated by bonding an optical fiber to a curved substrate after removal of the fiber coating [3]. The curved substrate allows the polishing of the fiber sideways over a small length of the fiber. The polished fiber is then placed in an evaporation chamber where a metal is evaporated onto the fiber. For the initial tests, the metal was silver. After evaporation of the metal, the sensor was ready to test.

The metal thickness was chosen so that the surface plasmon would form at a sample index of 1.42 [3]. Figure 4.4 shows the outputs obtained by Bender [3] for two tests performed using these sensors. As can be seen from this plot, the resonance condition was met at a sample index slightly below 1.42. This is caused by the process used for the application of the metal film. Evaporated film thicknesses are typically accurate to within a few percent, so the small variations seen in the experimental data when compared to the predicted results is typical. However, the difference between the expected and actual values was very small indicating that with slightly improved control over the metal coating process, the possibility of choosing and applying metal films of the proper thickness to excite surface plasmons exists.

In order to monitor index values less than 1.41, or to measure changes in the metal itself, this system would not work. As mentioned in the previous section, sample indices less than 1.41 cannot excite surface plasmons for the three layer optical fiber system. In order to measure corrosion, the task of this research, the metal must have access to the outer environment, something that is not possible if a sample index greater than 1.41 is present. The answer to this problem was the addition of a fourth layer to the sensor geometry.

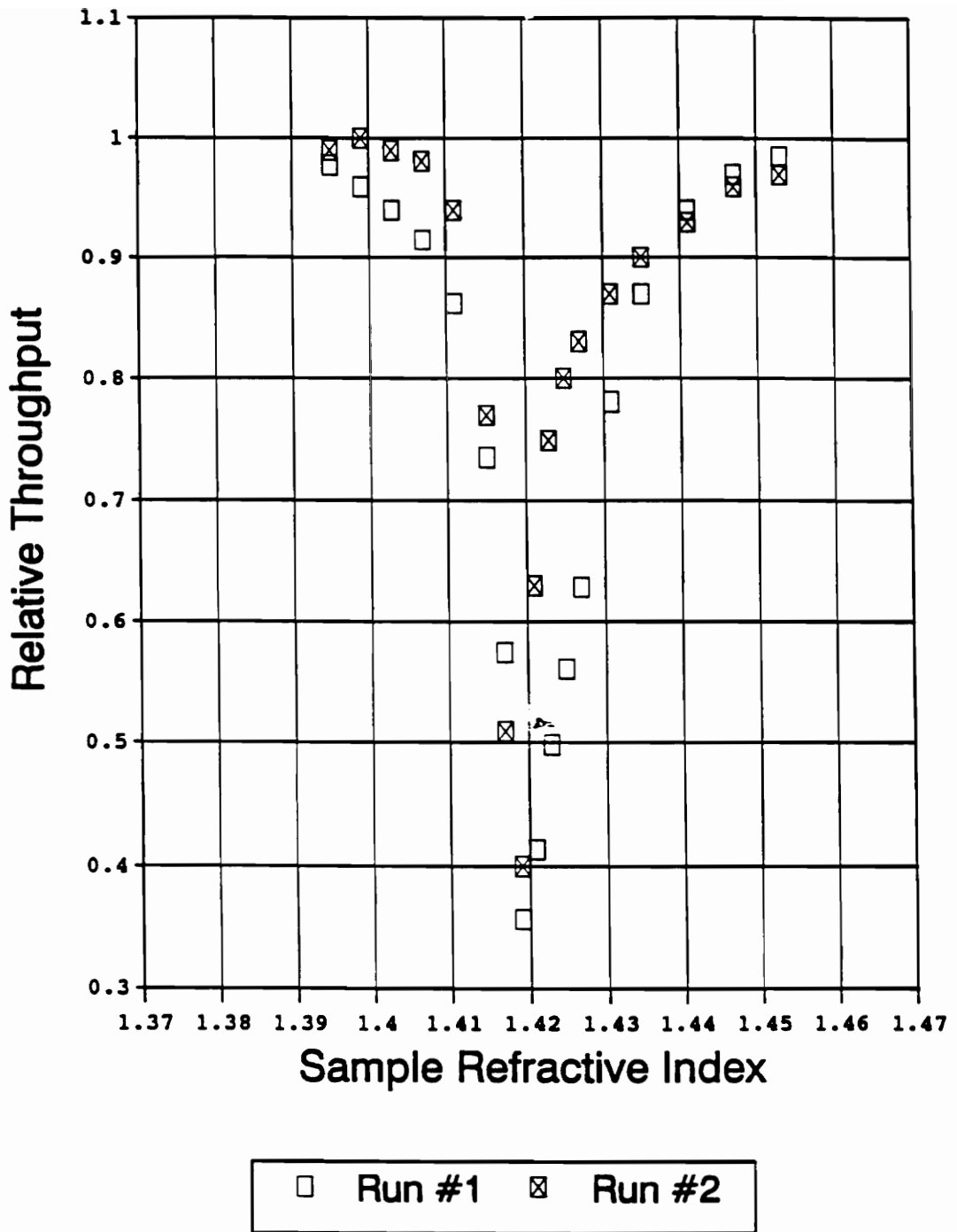


Figure 4.4. Experimental curves for two 3-layer surface plasmon devices [3].

4.3 4-Layer Surface Plasmon Resonance

The basic limitation of the 3-layer surface plasmon design as described in the previous sections is that the indices of the two dielectric materials above and below the metal film must be roughly equal. Therefore, with the fiber effective index (average of the core and cladding) equal to 1.45, the index of the outer material must be closely matched to 1.45. If there was a method to create an effective index in the sampling region that matched the fiber effective index even though the outermost index was less than 1.41, we could make measurements in aqueous solutions (indices near 1.33) or possibly in air (index roughly 1.0). To accomplish this, a fourth layer is added above the metal to bring the effective index up to match the fiber index as shown in Figure 4.5. This fourth layer, called the overlay, is a very thin layer of a high index material, e.g. silicon monoxide at an index of 1.93, placed between the metal and the sample. This geometry will allow sample indices from 1.0 (open to air) to approximately 1.5.

4.3.1 Theoretical Analysis

The theory presented in this section was developed in collaboration with Bender and is also presented in his doctoral dissertation [3]. The geometry is again approximated as a planar waveguide and the metal is treated as the core of the waveguide. This time, the top cladding is a double cladding consisting of the overlay and the sample. The effect of the planar waveguide approximation is a broadening of the expected resonance dip and a lessening of the percent power transfer at the exact resonance condition. The two effects are caused by the presence of the taper in the cladding and slight curvature of the core caused by the polish on the curved substrate. The further from the center of the polished region, the greater the curvature of the core and the thickness of the cladding. These two changes cause the resonance condition to change slightly as one looks further away from the center of the polish. The net effect is that there will be a continuous set of resonance

conditions, all very close to the desired condition. This set causes the broadening of the resonance dip because the indices surrounding the expected index will also form lesser resonances in the region surrounding the exact center of the polish. Similarly, the percent power transfer will not be the expected 100% for the TM mode because of the continuous set of resonance conditions. Waveguide equations are set up as with the 3-layer system and the dispersion relation is determined.

The electric and magnetic fields in the four planar layers are written for the TM mode with unknown magnitude coefficients A-F. Once again, the TE modes do not extend into the cladding and are therefore not included in the theory.

$$\begin{aligned}
 H_y^{sample} &= F e^{-i(n_s^2 k^2 - \beta^2)^{1/2} x} \\
 H_y^{overlay} &= C e^{i(n_o^2 k^2 - \beta^2)^{1/2} x} + D e^{-i(n_o^2 k^2 - \beta^2)^{1/2} x} \\
 H_y^{metal} &= A e^{i(n_m^2 k^2 - \beta^2)^{1/2} x} + B e^{-i(n_m^2 k^2 - \beta^2)^{1/2} x} \\
 H_y^{clad} &= E e^{i(n_c^2 k^2 - \beta^2)^{1/2} x} \\
 \\
 E_x^{sample} &= \left(-i / n_s^2 \omega E_o \right) \left\{ -F i (n_s^2 k^2 - \beta^2)^{1/2} e^{-i(n_s^2 k^2 - \beta^2)^{1/2} x} \right\} \\
 E_x^{overlay} &= \left(-i / n_o^2 \omega E_o \right) \left\{ \begin{aligned} &C i (n_o^2 k^2 - \beta^2)^{1/2} e^{i(n_o^2 k^2 - \beta^2)^{1/2} x} \\ &-D i (n_o^2 k^2 - \beta^2)^{1/2} e^{-i(n_o^2 k^2 - \beta^2)^{1/2} x} \end{aligned} \right\} \\
 E_x^{metal} &= \left(-i / n_m^2 \omega E_o \right) \left\{ \begin{aligned} &A i (n_m^2 k^2 - \beta^2)^{1/2} e^{i(n_m^2 k^2 - \beta^2)^{1/2} x} \\ &-B i (n_m^2 k^2 - \beta^2)^{1/2} e^{-i(n_m^2 k^2 - \beta^2)^{1/2} x} \end{aligned} \right\}, \tag{4.5} \\
 E_x^{clad} &= \left(-i / n_c^2 \omega E_o \right) \left\{ E i (n_c^2 k^2 - \beta^2)^{1/2} e^{i(n_c^2 k^2 - \beta^2)^{1/2} x} \right\}
 \end{aligned}$$

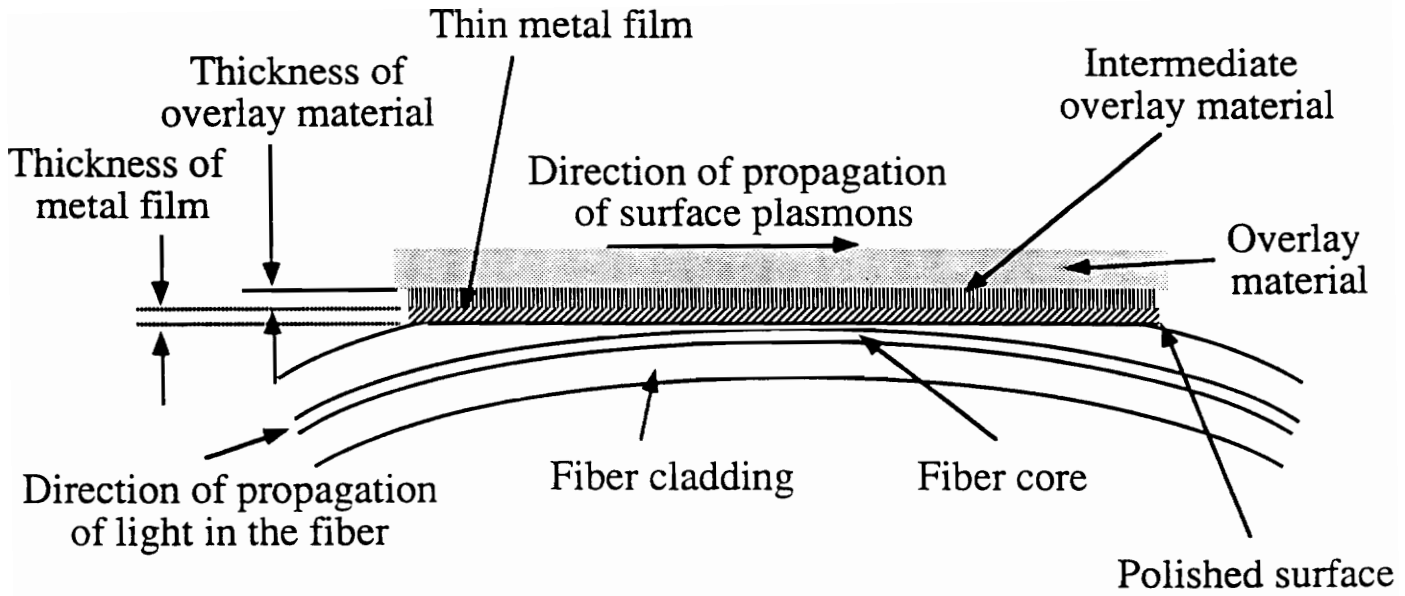


Figure 4.5. Schematic of the four-layer surface plasmon geometry.

where n_s is the sample index, n_o is the overlay index, n_m is the metal index and n_c is the cladding index. As with all waveguide analyses, the outer materials have only one component for each field to insure that the fields do not expand to infinity with the distance from the z-axis. These fields must meet the electric and magnetic field boundary conditions evaluated at the material boundaries. The boundary condition state that the transverse electric and magnetic field components must be continuous at the boundaries between two materials. That is, for the TM mode, E_z and H_y in the core and cladding must be equal at the boundary between the core and cladding. The following equations are the result of the boundary conditions:

$$\begin{aligned} Fe^{-\alpha d_2} &= Ce^{\gamma d_2} + De^{-\gamma d_2} \\ Ce^{\gamma d_1} + De^{-\gamma d_1} &= Ae^{\Delta d_1} - Be^{-\Delta d_1} \\ E &= A + B \end{aligned}$$

$$\begin{aligned} \left(\frac{\alpha}{n_s^2}\right)\{-Fe^{-\alpha d_2}\} &= \left(\frac{\gamma}{n_o^2}\right)\{Ce^{\gamma d_2} - De^{-\gamma d_2}\} \\ \left(\frac{\gamma}{n_o^2}\right)\{Ce^{\gamma d_1} - De^{-\gamma d_1}\} &= \left(\frac{\Delta}{n_m^2}\right)\{Ae^{\Delta d_1} - Be^{-\Delta d_1}\} \\ \left(\frac{\rho}{n_c^2}\right)\{E\} &= \left(\frac{\Delta}{n_m^2}\right)\{A - B\} \end{aligned}$$

where

$$\begin{aligned} \alpha &= i(n_s^2 k^2 - \beta^2)^{1/2} = (\beta^2 - n_s^2 k^2)^{1/2} \\ \gamma &= i(n_o^2 k^2 - \beta^2)^{1/2} = (\beta^2 - n_o^2 k^2)^{1/2} \\ \Delta &= i(n_m^2 k^2 - \beta^2)^{1/2} = (\beta^2 - n_m^2 k^2)^{1/2} \\ \rho &= i(n_c^2 k^2 - \beta^2)^{1/2} = (\beta^2 - n_c^2 k^2)^{1/2} \end{aligned} \quad (4.6)$$

The above equation represents six equations and six unknowns (A, B, C, D, E, and F). This set of equations is then reduced to two equations with two unknowns in the following manner. First, since E is exactly described in the sixth equation, it is substituted for in the third equation. This gives

$$\left(\frac{\rho}{n_c^2}\right)\{A+B\} = \left(\frac{\Delta}{n_m^2}\right)\{A-B\}. \quad (4.7)$$

Next, the first equation is solved for F, and F is substituted into the fourth equation to give

$$\left(\frac{\gamma}{n_o^2}\right)\{Ce^{\gamma d_2} - De^{-\gamma d_2}\} = \left(-\frac{\alpha}{n_s^2}\right)\{Ce^{(\gamma d_2 + \alpha d_1)} + De^{(\alpha d_1 - \gamma d_2)}\}. \quad (4.8)$$

There are now four unknowns left (A, B, C, and D). Equation (4.8) is then solved for D, and D is substituted into the second and fifth equations of Equation (4.6) to give the following equations.

$$Ae^{\Delta d_1} + Be^{-\Delta d_1} = Ce^{\gamma d_1} + Ce^{2\gamma d_2} \frac{\frac{\gamma}{n_o^2} + \frac{\alpha}{n_s^2}}{\frac{\gamma}{n_o^2} - \frac{\alpha}{n_s^2}} e^{-\gamma d_1}. \quad (4.9)$$

$$\left(\frac{\Delta}{n_m^2}\right)\{Ae^{-\Delta d_1} - Be^{-\Delta d_1}\} = \left(\frac{\gamma}{n_o^2}\right)\{Ce^{\gamma d_1} - Ce^{2\gamma d_2}\} \frac{\frac{\gamma}{n_o^2} + \frac{\alpha}{n_s^2}}{\frac{\gamma}{n_o^2} - \frac{\alpha}{n_s^2}} e^{-\gamma d_1}. \quad (4.10)$$

The next step is to solve Equation (4.9) for C, and substitute C into Equation (4.10). This gives the following.

$$\left(\frac{\Delta}{n_m^2}\right)\{Ae^{\Delta d_1} - Be^{-\Delta d_1}\} = \frac{\frac{\gamma}{n_o^2} \left\{ \left(Ae^{\Delta d_1} + Be^{-\Delta d_1} \right) \left(e^{\gamma d_1} - e^{2\gamma d_2} \frac{\frac{\gamma}{n_o^2} + \frac{\alpha}{n_s^2}}{\frac{\gamma}{n_o^2} - \frac{\alpha}{n_s^2}} e^{-\gamma d_1} \right) \right\}}{e^{\gamma d_1} + e^{2\gamma d_2} \frac{\frac{\gamma}{n_o^2} + \frac{\alpha}{n_s^2}}{\frac{\gamma}{n_o^2} - \frac{\alpha}{n_s^2}} e^{-\gamma d_1}}. \quad (4.11)$$

There are now two equations, (4.7) and (4.11), and two unknowns, A and B. Equations (4.7) and (4.11) are then re-arranged to separate the A and B terms. This gives us

$$A\left(\frac{\rho}{n_c^2} - \frac{\Delta}{n_m^2}\right) + B\left(\frac{\rho}{n_c^2} + \frac{\Delta}{n_m^2}\right) = 0 \quad (4.12)$$

for Equation (4.7) and

$$\begin{aligned} & Ae^{\Delta d_1} \left\{ \frac{\gamma}{n_o^2} \left(e^{\gamma d_1} - e^{2\gamma d_2} \frac{\frac{\gamma}{n_o^2} + \frac{\alpha}{n_s^2}}{\frac{\gamma}{n_o^2} - \frac{\alpha}{n_s^2}} e^{-\gamma d_1} \right) - \frac{\Delta}{n_m^2} \left(e^{\gamma d_1} + e^{2\gamma d_2} \frac{\frac{\gamma}{n_o^2} + \frac{\alpha}{n_s^2}}{\frac{\gamma}{n_o^2} - \frac{\alpha}{n_s^2}} e^{-\gamma d_1} \right) \right\} + \\ & Be^{-\Delta d_1} \left\{ \frac{\gamma}{n_o^2} \left(e^{\gamma d_1} - e^{2\gamma d_2} \frac{\frac{\gamma}{n_o^2} + \frac{\alpha}{n_s^2}}{\frac{\gamma}{n_o^2} - \frac{\alpha}{n_s^2}} e^{-\gamma d_1} \right) - \frac{\Delta}{n_m^2} \left(e^{\gamma d_1} + e^{2\gamma d_2} \frac{\frac{\gamma}{n_o^2} + \frac{\alpha}{n_s^2}}{\frac{\gamma}{n_o^2} - \frac{\alpha}{n_s^2}} e^{-\gamma d_1} \right) \right\} = 0 \end{aligned} \quad (4.13)$$

for Equation (4.11). The coefficients for A and B from the two equations are then placed in a 2x2 determinant, and the determinant is set equal to zero. This produces the following dispersion relation for the waveguide:

$$d_2 = \ln \left\{ \frac{\left[\frac{\Delta}{n_m^2} + \frac{\rho}{n_c^2} \right] \left[e^{(\gamma+\Delta)d_1} \right] \left[\frac{\gamma}{n_o^2} - \frac{\Delta}{n_m^2} \right] - \left[\frac{\rho}{n_c^2} - \frac{\Delta}{n_m^2} \right] \left[e^{(\gamma-\Delta)d_1} \right] \left[\frac{\gamma}{n_o^2} + \frac{\Delta}{n_m^2} \right]}{\left[\frac{\rho}{n_c^2} - \frac{\Delta}{n_m^2} \right] \left[e^{-(\gamma+\Delta)d_1} \right] \left[\frac{\gamma}{n_o^2} + \frac{\alpha}{n_s^2} \right] \left[\frac{\Delta}{n_m^2} - \frac{\gamma}{n_o^2} \right] + \left[\frac{\Delta}{n_m^2} + \frac{\rho}{n_c^2} \right] \left[e^{(\Delta-\gamma)d_1} \right] \left[\frac{\gamma}{n_o^2} + \frac{\alpha}{n_s^2} \right] \left[\frac{\gamma}{n_o^2} - \frac{\Delta}{n_m^2} \right]} \right\} \frac{1}{2\gamma} \quad (4.14)$$

The relation is solved for d_2 , which when d_1 is known may be used to find the overlay thickness, because it must be known in order to design and fabricate a sensor. The dispersion relation is plotted in Figure 4.6 using the same values as were used for the 3-layer system for n_m and d_1 , and $n_s = 1.35$. This dispersion plot shows that the overlay thickness goes to infinity at an overlay refractive index of approximately 1.41 which would be equivalent to the behavior of the 3-layer system. This result is important in that it helps prove the validity of the results.

4.3.2 Experimental Results

Experiments were performed by Bender for his dissertation, and a representative sample is presented here. A sensor was fabricated using silicon monoxide (SiO) as the overlay material and silver as the metal. The overlay thickness was 32.2 nm and the metal had a thickness of 34 nm. The dispersion relation indicated that the resonance would occur at a sample index of 1.35. A series of 14 standard sucrose solutions was made covering the index range of 1.338 to 1.400. These solutions were placed on the sensor in turn to generate the curve shown in Figure 4.7. This figure shows that the true resonance occurred at an index of 1.389 as opposed to the expected value of 1.35 for an error of 2.89% [3]. The average error for all experiments was 2.87% [3].

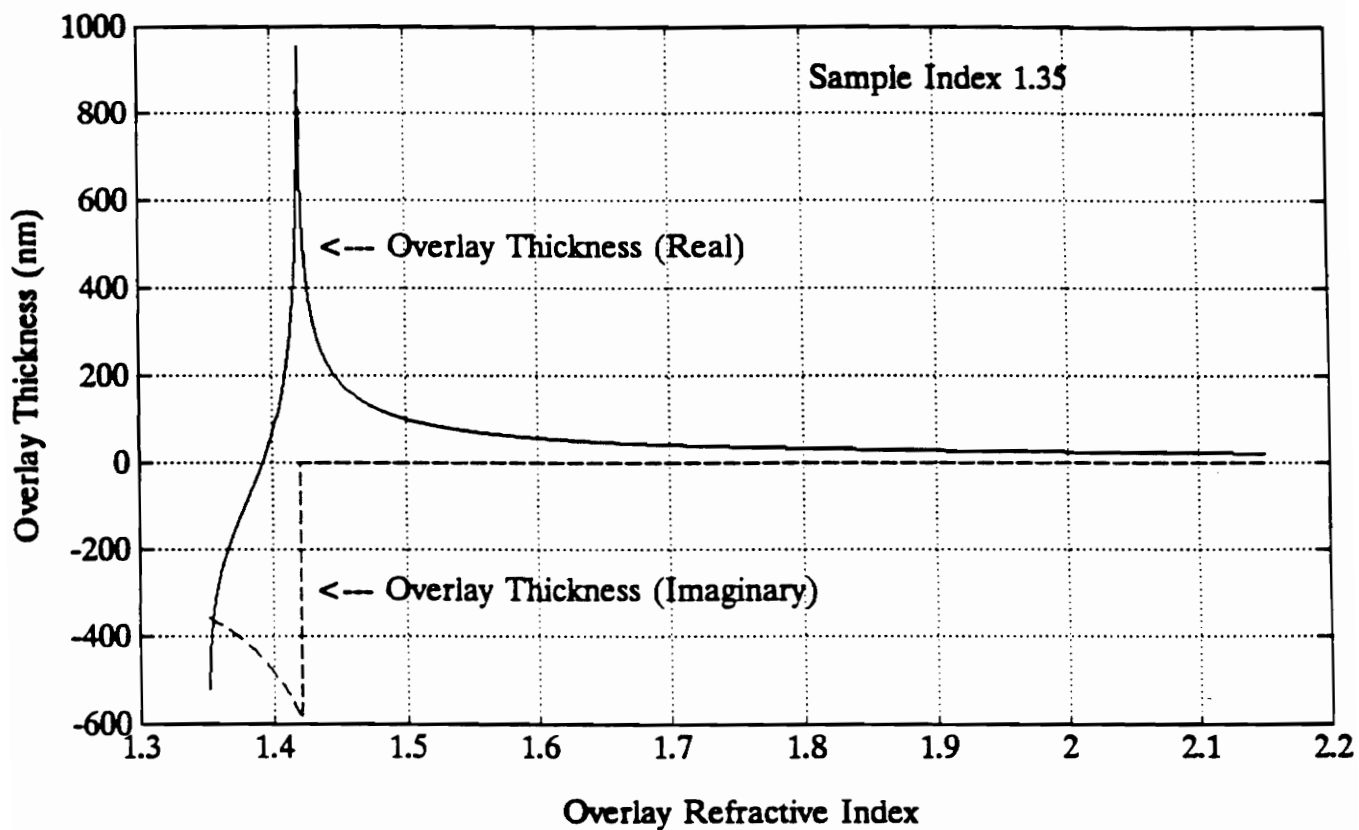


Figure 4.6. Dispersion relation for the 4-layer surface plasmon geometry.

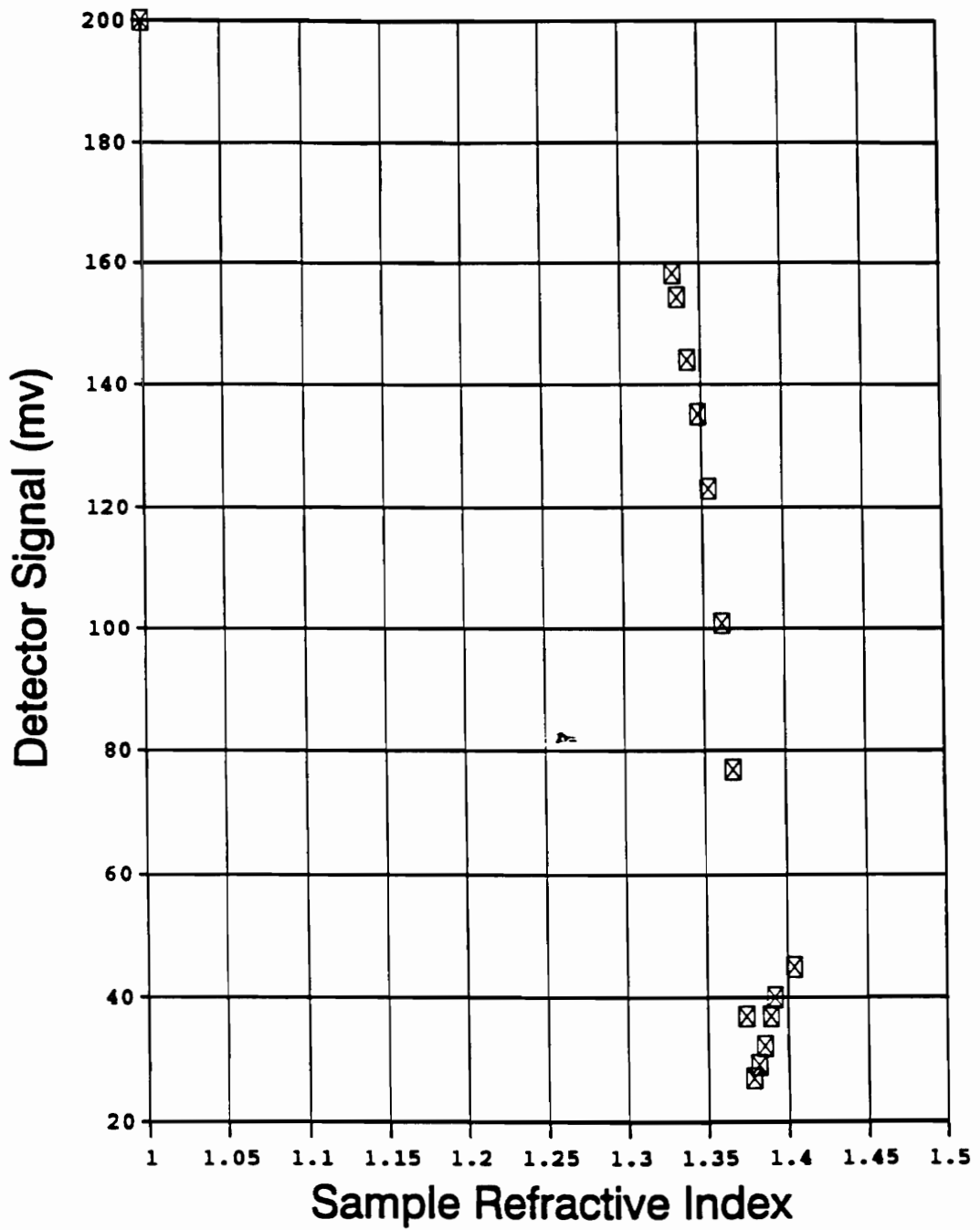


Figure 4.7. Experimental curve for the 4-layer surface plasmon sensor [3].

Although this sensor geometry allows operation at outer indices as low as that of air (1.0), the metal film is still not exposed to the environment, a necessity for a corrosion sensor. Therefore, an investigation into moving the overlay material to the other side of the metal (and calling it an underlay) was carried out. The dispersion relation was used with a sample index of 1.0 (air) and moving the overlay to the other side of the metal film, and the results were plotted as before. Figure 4.8 shows this plot. It can be seen from this plot that there is a region of overlay indices that would allow surface plasmon resonance for the modified 4-layer geometry. This system was not tested at this point because of the investigation into the cylindrical surface plasmon geometry. The following section describes this investigation.

4.4 Cylindrical Surface Plasmon Resonance

All of the previously described optical fiber surface plasmon analyses assumed that the waveguide structure must be approximately planar in order to function correctly. As the research into surface plasmons continued, it was thought possible that surface plasmons could also be formed in a cylindrical geometry, where the metal film would be coated cylindrically around the fiber. Since the original surface plasmon considerations depended on a light beam with a certain angle of incidence in a prism device, and a multimode fiber can be approximated by a series of rays at different angles in the fiber, it was concluded that a multimode fiber should also produce surface plasmons if the correct metal film and thickness were chosen. Also, since the angles are set in a multimode fiber, it was thought that the use of spectral analysis could provide more information than the standard power measurement technique. Surface plasmon resonance occurs at a certain wavelength for a given material and geometry, so by scanning the wavelengths around the resonance wavelength, the typical resonance curve, or dip, was expected.

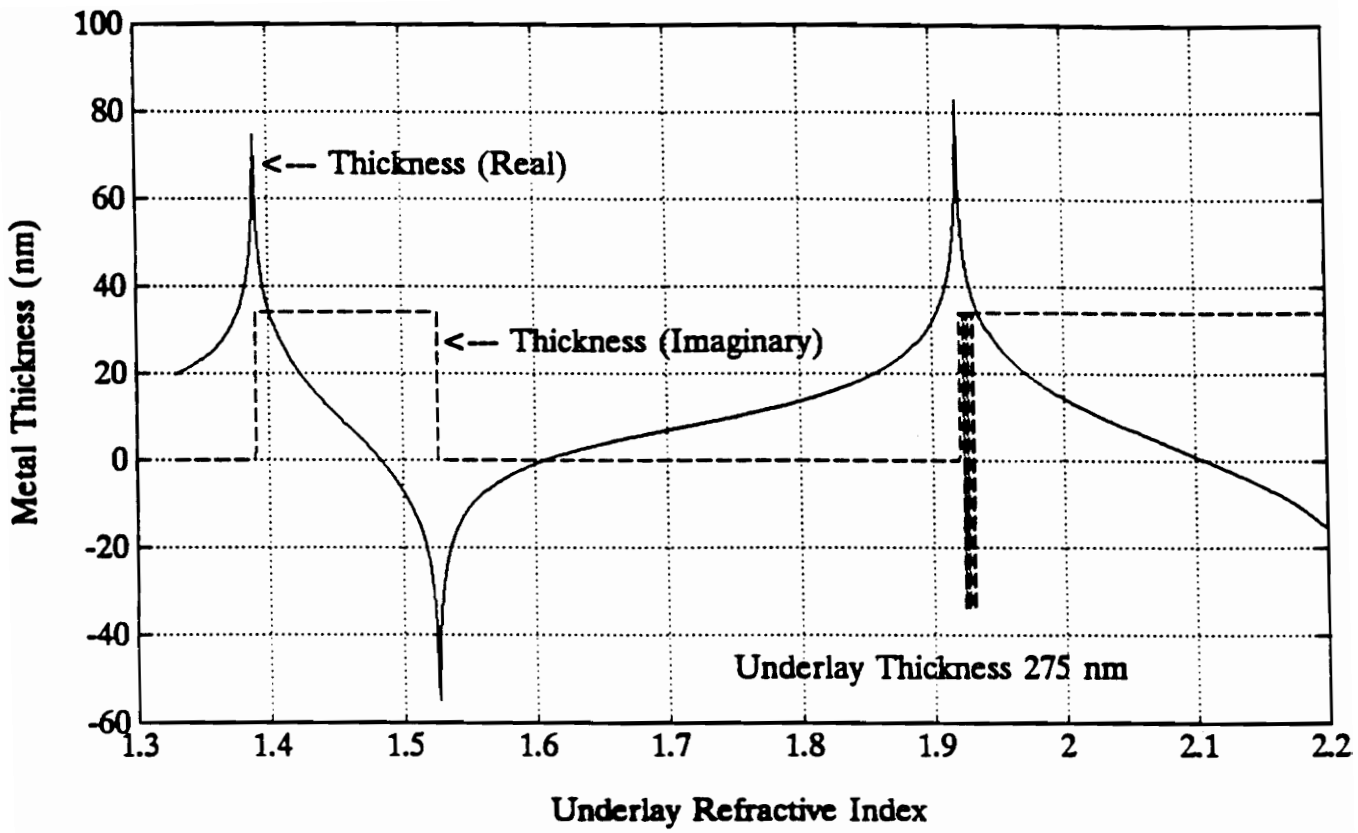


Figure 4.8. Dispersion curve for the modified 4-layer geometry with underlay.

4.4.1 Theoretical Analysis

A theoretical derivation is presented by Jorgenson et al [36] which involves using the ray approximation for the modes in the multimode optical fiber. These rays are treated as in consideration of the Kretschmann prism technique in that they are incident on the dielectric-metal boundary at a given angle. By calculating the resonance factor, i.e. the amount of energy transferred to the surface plasmon, for each angle in the fiber, Jorgenson was able to generate a generic curve of power versus wavelength [36]. Figure 4.9 shows Jorgenson's curve for two aqueous solutions as the outer material. The sensor described in [36] used a 400 micron core fiber and a silver film. The experimental results showed that this sensor was feasible and more practical than the polished single-mode surface plasmon sensors described in the preceding sections.

4.4.2 Experimental Results

To analyze the possibility of using the cylindrically-coated optical fiber surface plasmon geometry for corrosion sensing, a series of sensors were fabricated using 200/240 plastic-clad optical fiber. The use of a plastic cladding allowed the cladding to be removed and replaced with a metal. Initial tests were performed with silver as the metal. Two solutions with different refractive indices were applied to the sensor and the spectra were recorded. Figures 4.10 and 4.11 are curves representing the spectral outputs for sample indices of 1.3595 and 1.3856, respectively. The values for the refractive indices for the solutions were determined from a formula relating the concentration of the sucrose in the solution to the exact refractive index. The resonance wavelength shifted from 540 nm at an index of 1.3595 to a wavelength of 800 nm at an index of 1.3856. Each nanometer of spectral shift therefore represents an index change of 3.115×10^{-4} .

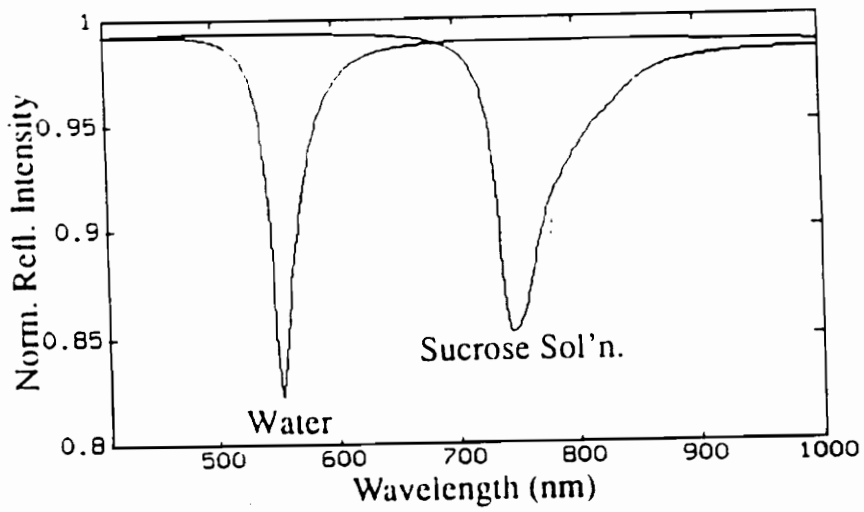


Figure 4.9. Reprint of the theoretical curve for the spectral analysis of the cylindrical surface plasmon device [36].

These experiments prove the validity of this sensing technique for refractive index monitoring, but raise a question about its use in corrosion monitoring. The environment surrounding the sensor is not guaranteed to remain at a certain index of refraction. In fact the environment could be air, water or even a sealant or paint. Since the factor of interest would be the thickness of the metal film, variations in the surrounding medium's refractive index would cause major changes in the spectral response of the sensor thereby making it difficult to actually measure corrosion as opposed to the surrounding index of refraction. This is not to say that the sensor cannot be further modified or limited to be made to measure corrosion, or predict the constituents that cause corrosion before it occurs, it simply means that much more work would be necessary to make the sensing technique practical. Specifically, a technique to separate the changes in power due to outer index changes from metal thickness changes would be necessary. A method for consistent, easy manufacture is required, and that method would need to allow the production of robust sensors so that implementation would be practical.

The surface plasmon technique was being investigated in parallel with the metal-clad sensing technique described in the next chapter. As will be shown in the next chapter, the metal-clad technique was successfully demonstrated and shown to be inexpensive to fabricate and implement. Therefore, in the final downselect to choose one sensor to develop for corrosion sensing, the metal-clad sensor was chosen, and research into the surface-plasmon sensor was discontinued.

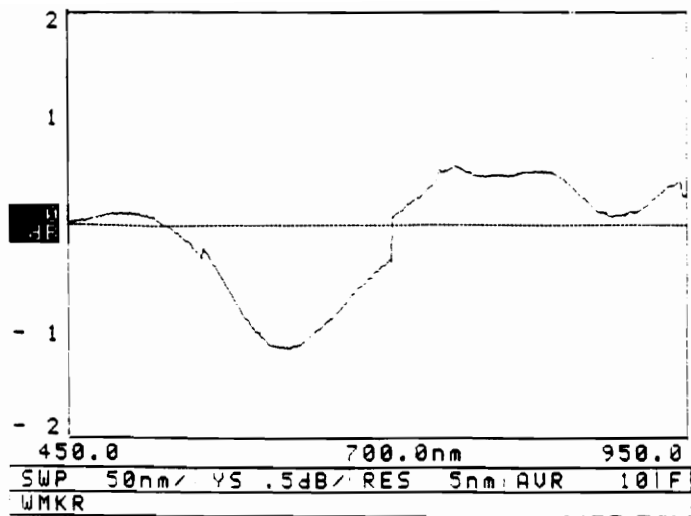


Figure 4.10. Spectrum of cylindrical surface plasmon device at sample index 1.3595.

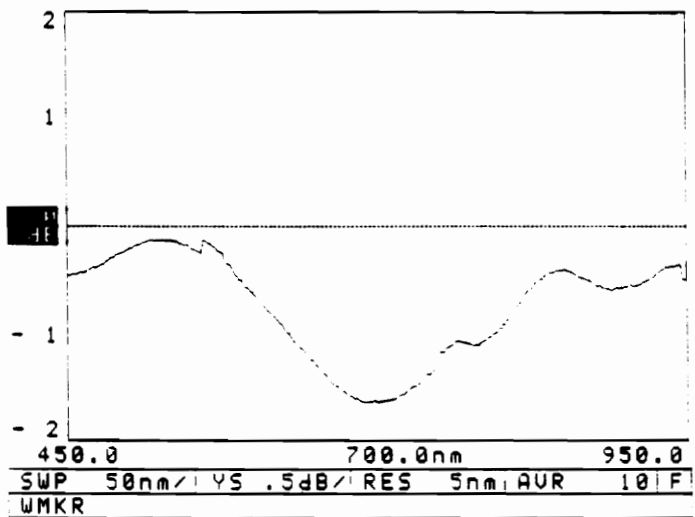


Figure 4.11. Spectrum of cylindrical surface plasmon device at sample index 1.3856.

CHAPTER 5: METAL-CLAD CORROSION SENSOR

The metal-clad corrosion described in section 3.6.3 has proven to be the most promising of all the optical fiber corrosion sensing techniques tested in this work. As described in Section 3.6.3, the metal-clad corrosion sensor consists of a glass core and a metal cladding. The input and output fibers are standard multimode silica fibers chosen to match core diameter with that of the sensing fiber. Figure 5.1 shows a typical setup for the metal-clad corrosion sensor. The signal processing scheme is designed to correct for source fluctuations by dividing out a reference detector signal that monitors the source only (detector D2 in Figure 5.1). The basis of operation is that the light entering the sensing region experiences loss as it passes through the metal-clad region. As the metal cladding changes due to the corrosion process, the loss also changes. Since the main effect of corrosion is a thinning of the metal, the loss in the sensing region will lessen with corrosion. Therefore, the output power from the sensor will increase as corrosion progresses. For most intensity-based sensors, the signal level decreases with the measurand. The fact that the signal level increases for the corrosion sensor offers many advantages. Intensity sensors have historically presented problems to engineers because of source fluctuation, bending, and connector losses causing false readings from the sensor processing unit. The effect is caused when the power level decreases due these three effects and a decrease in the signal level also indicates a change in the measurand. The metal-clad corrosion sensor output increases with corrosion, and as will be shown, increases nearly an order of magnitude. This removes the problem of misinterpreting power losses as signal measurement changes.

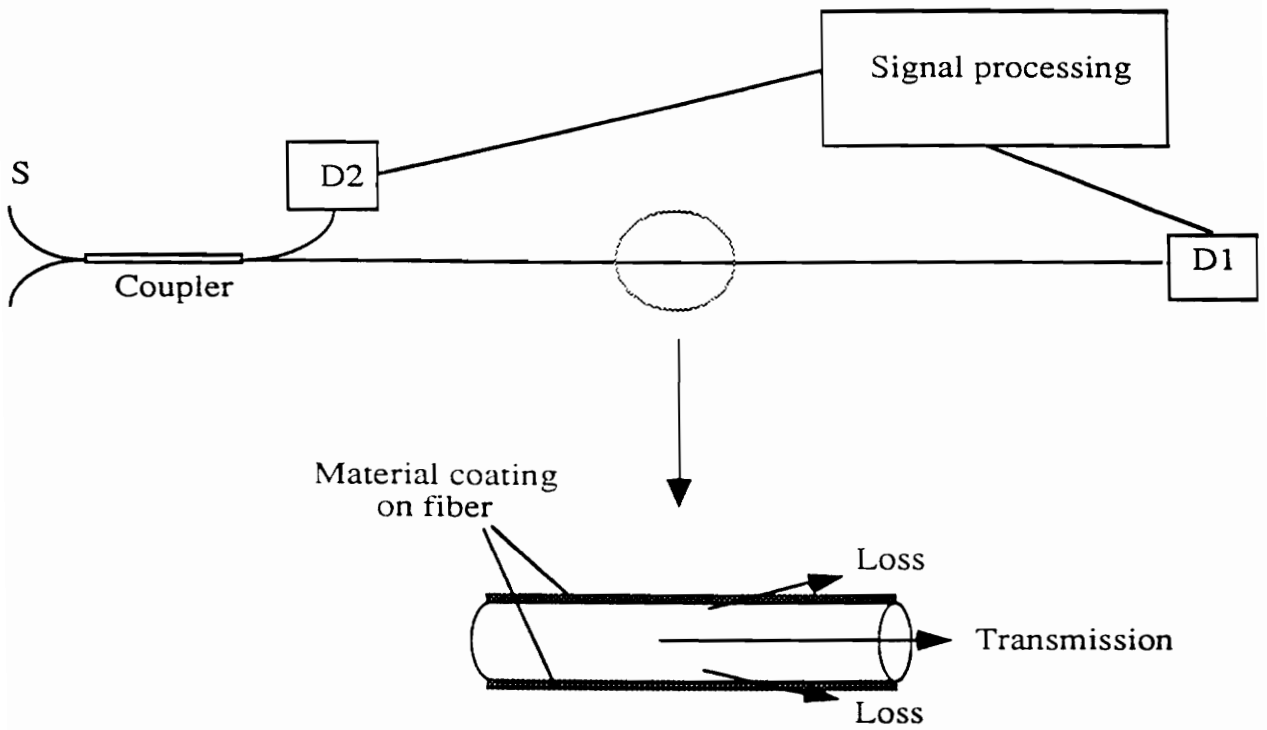


Figure 5.1. Schematic of the metal-clad corrosion sensor. S-Source, D1 - Sensing detector, D2-Source monitor detector.

Initial tests were performed to determine the feasibility of the sensing method. A hard-clad silica 200/240 micron optical fiber made by Ensign-Bickford was modified by removing a section of its plastic cladding mechanically and replacing it with an aluminum cladding. Aluminum was the metal of choice for this program since the end product is anticipated for aircraft where aluminum is primarily used. The aluminum was evaporated onto the cladding-stripped fiber in a standard vacuum evaporation chamber. The end thickness was estimated to be between one and two microns. The first of the sensors were placed in the corrosion test cell described in Section 3.5.2 to initialize the system and estimate testing times for the corrosion process. Once these values were determined, the test was repeated and data was collected. Figure 5.2 shows the data collected for this test. As is evident in the curve, the output does indeed increase markedly with the removal of the aluminum caused by corrosion. The time difference between the onset of intensity changes between the two sensors can be attributed to the method used to fabricate the sensors. Since these initial tests were performed in order to prove the feasibility of the sensor, no special care was taken in their fabrication. The tests were performed solely to test the hypothesis behind the sensor, that the power level would indeed increase as the metal film was removed from the fiber by corrosion. For these tests, the mechanical means of removing the plastic cladding may not have provided a completely clean surface on which to evaporate. Also, the plastic cladding may not have been removed completely in all places. A second reason for these differences could be the evaporation process itself. Since evaporation is typically used to coat flat surfaces, the coating was probably not uniform around the circumference of the fiber. Placement in the corrosion chamber could also have been a factor. One of the sensors was further from the water in the bottom of the chamber and may not have been subjected to the same temperature and humidity as the second. All of these factors were investigated further as the research progressed. The results of these investigations are presented throughout the chapter.

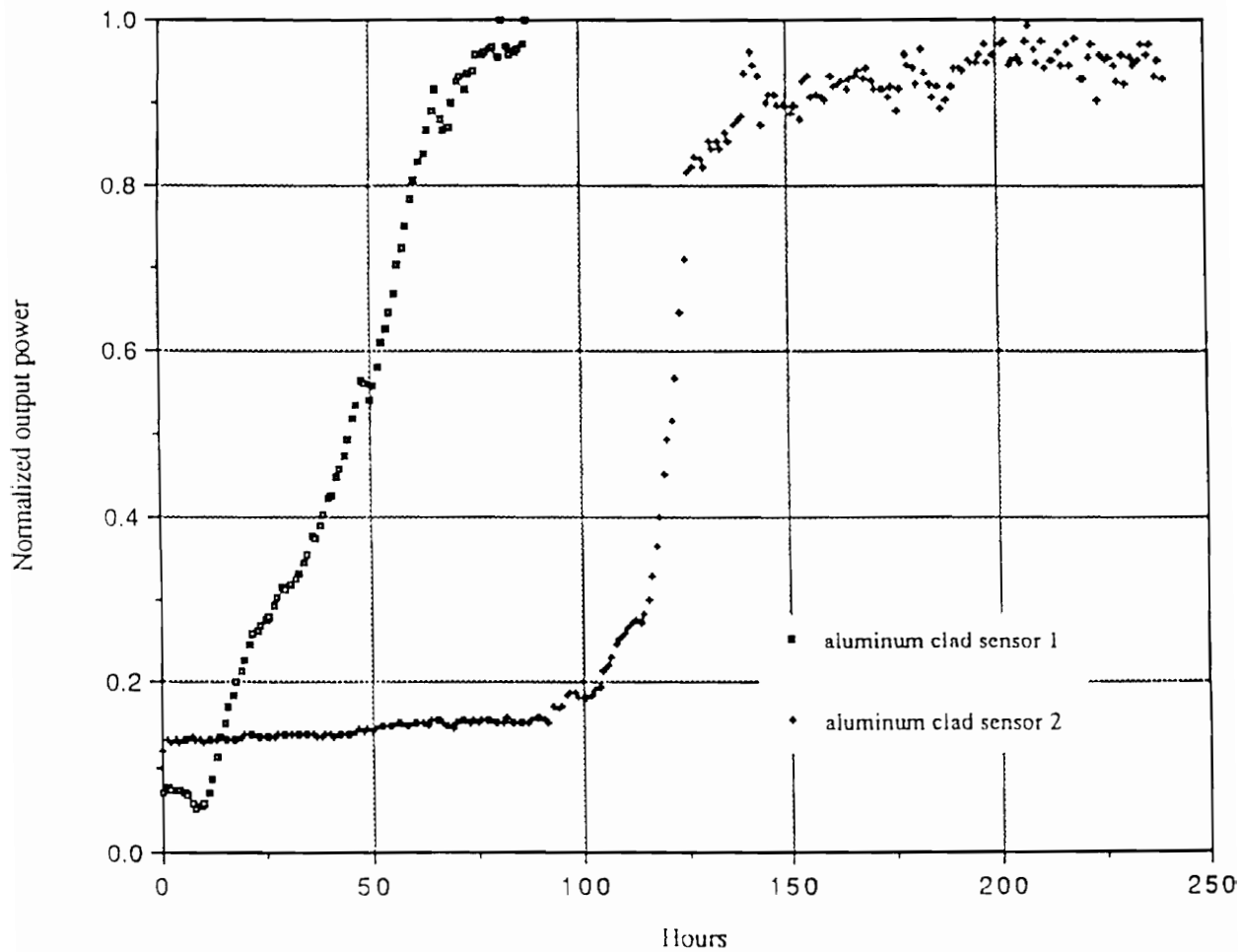


Figure 5.2. Output power versus time for two aluminum-clad corrosion sensors.

Upon analysis of the data presented in Figure 5.2, it was decided to further investigate the metal-clad aluminum corrosion sensor. This investigation included a theoretical analysis to help understand the sensor and predict the effect of various parameters on the function of the sensor. Additional testing was performed to verify the theory, identify the best lengths for the sensor and wavelengths of the source, and also to identify methods for fabricating the sensor. Also, the initial tests used pure aluminum as the metal, but aircraft are fabricated using aluminum alloys. Therefore, a method to coat aluminum alloy films onto the fiber as the cladding was developed. The results of these investigations comprise the remainder of this chapter.

5.1 Theoretical Analysis

A theoretical model was developed to predict the response of the metal-clad corrosion sensors. The model is based on the geometric ray-optics approximation to waveguiding in an optical fiber. Basically, this approximation estimates each mode propagating in an optical fiber as a ray traveling at a specific angle with respect to the core/cladding interface. The range of angles is limited to between 0° and the critical angle for the core/cladding index ratio. Figure 5.3 shows the geometry of the fiber and the ray approximation for the light in the fiber.

The critical angle is the angle at which there is no transmission of light across the interface. The critical angle, θ_c is defined by the equation

$$\cos(\theta_c) = \frac{n_2}{n_1}, \quad (5.1)$$

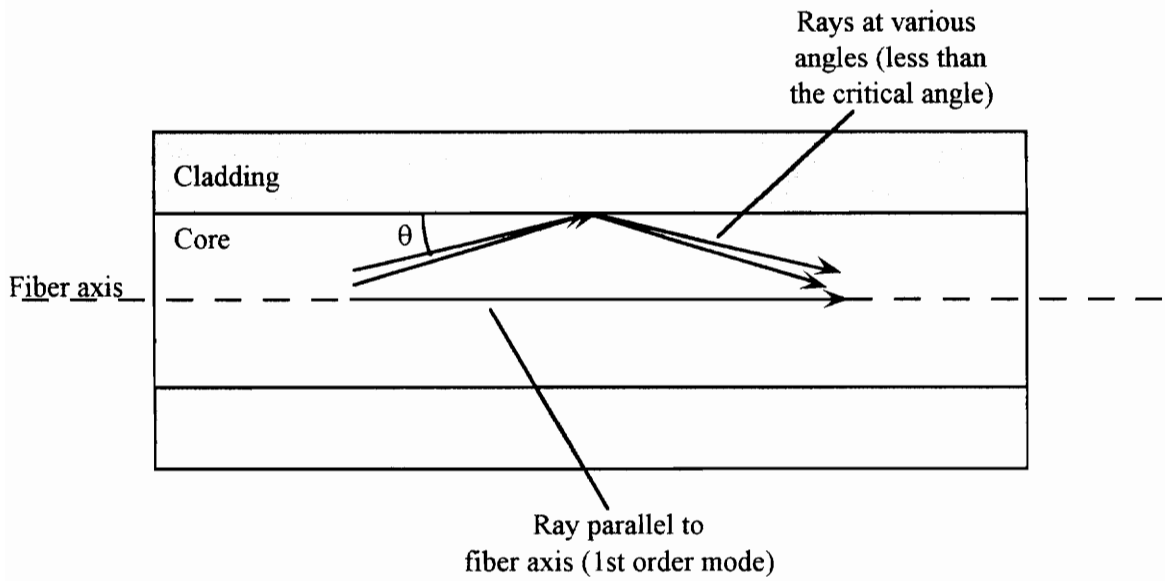


Figure 5.3. Schematic of a fiber and the ray-optics approximation

where n_2 is the index of the cladding and n_1 is the index of the core. In order for a specific ray angle to exist in a fiber, a phase matching condition must hold true. That is, the phase of a given ray must change by a multiple of 2π after traveling twice across the fiber and reflecting off the top and bottom interfaces. This insures that the multiple reflections will remain in phase with one another and not cancel each other out. The solution for an allowable angle is given by [35]

$$\theta = \sin^{-1} \left(\frac{2n_1kd}{2\delta + 2\pi m} \right), \quad (5.2)$$

where M is an integer, d is the diameter of the fiber, and k is the free space propagation constant for the light given by $k=2\pi/\lambda$. δ is given by the equation

$$\delta = 2 \arctan \frac{(n^2 \cos^2(\theta) - 1)^{1/2}}{n \sin \theta}, \quad (5.3)$$

where n is given by n_1/n_2 . By combining the maximum possible angle (Equation (5.1)) with the equation defining the possible angles (Equation (5.2)), a complete set of angles is defined for a given fiber.

For this derivation, it is assumed that the rays at each angle defined above are propagating in the fiber prior to reaching the modified region with the metal cladding. Upon reaching this region, the rays with these angles continue to propagate down the fiber, but they are now affected by the presence of the metal cladding. This assumption is reasonable because the rays are considered to be propagating in an infinite medium until they interact with the core/cladding boundary. The reflection at the boundary is calculated as if each ray was a plane wave incident on the surface. Therefore, the change from glass-clad to metal-clad fiber will not affect the rays until those rays propagate to

the edge of the core and interact with the metal. To determine the effect of the metal cladding on the rays in the fiber, the Fresnel formulation [17] is used to calculate a reflectivity for each angle. There are two possible cases for a given angle, that of transverse magnetic (TM) polarization or transverse electric (TE) polarization. It will be assumed that the light is split evenly between these two polarization states because for this derivation, the source is assumed to be unpolarized indicating an even split between two orthogonal polarization states. The basic Fresnel formula for the reflection from a multilayer interface is modified for this derivation by replacing the second dielectric with the metal having a complex index of refraction. The outer material's index is included in this formulation as n_3 , and n_2 , the index of the cladding, is now a complex quantity. Figure 5.4 defines the geometry of the interfaces and shows the incident, transmitted, and reflected light rays. The incident light ray is partially reflected at both of the interfaces and the total reflection coefficient is calculated by combining these two reflections and taking into account their phase difference. That is, the reflection depends on the reflectivities of the interfaces and the phase of the two reflections upon recombination.

The derivation of the reflectivities and phases of the reflections and the recombination process is given by Born and Wolf [20]. The intensity reflectivity \mathfrak{R} , which is the square of the field reflection coefficient, is given by the expression

$$\mathfrak{R} = |r|^2 = \left| \frac{r_{12} + r_{23}e^{2i\beta}}{1 + r_{12}r_{23}e^{2i\beta}} \right|^2, \quad (5.4)$$

where r_{12} and r_{23} are the magnitudes of the reflection coefficients at the dielectric/metal and metal/outer material interfaces, respectively. The value for β is defined by

$$\beta = \frac{2\pi}{\lambda_0} \tilde{n}_2 h \cos \theta_2, \quad (5.5)$$

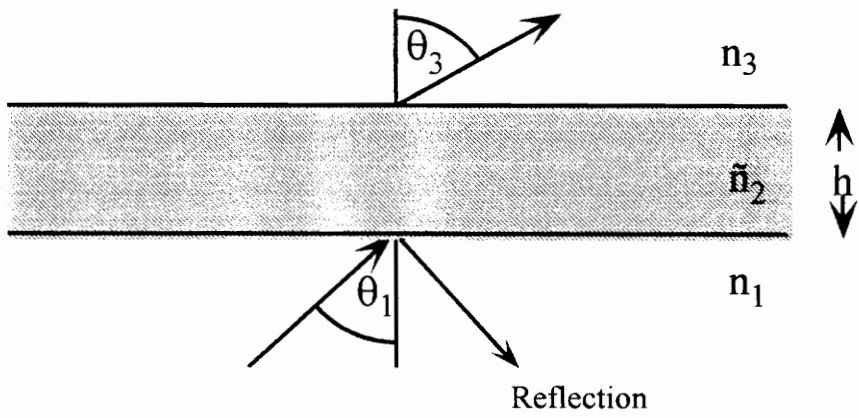


Figure 5.4. A metal film between two dielectric media.

where h is the thickness of the metal film and θ_2 is defined by Snell's Law: $n_1 \cos \theta_1 = \tilde{n}_2 \cos \theta_2$. Recall that \tilde{n}_2 is the complex index of refraction for the metal. The reflection coefficients are different for the TE and TM polarizations. For TE polarization, the values for the reflection coefficients are calculated to be

$$r_{12} = \frac{n_1 \cos \theta_1 - \tilde{n}_2 \cos \theta_2}{n_1 \cos \theta_1 + \tilde{n}_2 \cos \theta_2}, \text{ and} \quad (5.6)$$

$$r_{23} = \frac{\tilde{n}_2 \cos \theta_2 - n_3 \cos \theta_3}{\tilde{n}_2 \cos \theta_2 + n_3 \cos \theta_3}. \quad (5.7)$$

For the TM case the equations are calculated to be

$$r_{12} = \frac{\frac{\cos \theta_1}{n_1} - \frac{\cos \theta_2}{\tilde{n}_2}}{\frac{\cos \theta_1}{n_1} + \frac{\cos \theta_2}{\tilde{n}_2}}, \text{ and} \quad (5.8)$$

$$r_{23} = \frac{\frac{\cos \theta_2}{\tilde{n}_2} - \frac{\cos \theta_3}{n_3}}{\frac{\cos \theta_2}{\tilde{n}_2} + \frac{\cos \theta_3}{n_3}}. \quad (5.9)$$

Then next step is to calculate the number of times each ray will reflect off the core/metal interface as it travels down the sensing region. This is a simple case of geometry. Assuming the ray starts at the center of the core, the number of reflections is calculated to be

$$\# \text{ reflections} = NR = \frac{L \tan \theta}{d}, \quad (5.10)$$

where L is the length of the sensing region. The TE and TM intensity reflectivities are raised to the power of the number of reflections and averaged (assuming a 50/50 split between the polarization states) to obtain the percentage of total power transmitted through the sensing region for each ray.

The distribution of energy in the rays in the fiber is assumed to be Gaussian with the most light in the rays closest to the axis, a standard assumption for multimode fibers. Therefore, the ray angles are weighted using a Gaussian distribution and the total power is the sum of the powers transmitted through the sensing region for each ray.

It should be mentioned that this approximation assumes there is no loss in the lowest order mode since it has no reflections as it travels down the fiber. Additionally, this formulation assumes a perfectly straight sensing region. No bending of the sensing region is taken into account. A uniform bend in the fiber could be included by modifying the angles of incidence of the rays based on the radius of curvature of the bend and the distance down the sensing region. However, this was not the intent of the initial model.

Figure 5.5 shows a theoretical plot for values matching those used in the experiment described in the previous section. Those values are: a wavelength of 633 nm, a sensing length of approximately 250 cm, a fiber having a 200/240 micron core/cladding profile, and the proper indices of refraction for the core and the outer material. It needs to be noted that the theoretical curves shown in this dissertation show a decrease in metal thickness as the x-axis moves to the right. This is to allow comparison with the experimental curves where the increasing time scale leads to a decreasing thickness. Additionally, the plots stop when the thickness reaches zero.

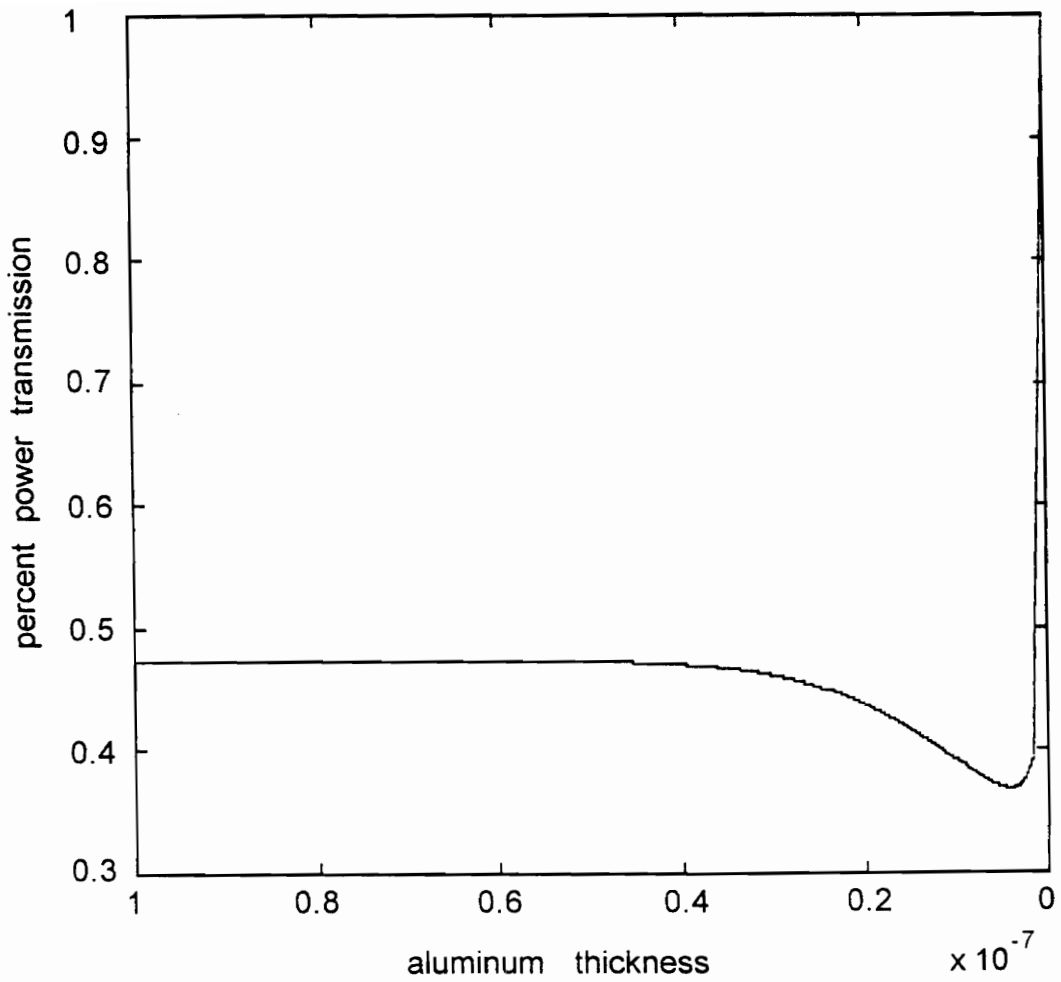


Figure 5.5. Theoretical data for power level versus thickness using the physical data from the first experiment performed using the aluminum-clad fiber.

The first observation from Figure 5.5 is that the increase in power level is much greater for the experiment than for the theory. This is explained by the way the light is launched into the fiber and the geometry of the fiber in the test chamber. The launching of the HeNe laser into the fiber most likely resulted in an overfilled fiber. This overfilling will cause a great loss of light in the sensing region since this light will be removed almost totally by the aluminum, but when the metal is removed, the sensing region is more like a waveguide, and this overfilled light can still be maintained by the fiber. This is not taken into account by the theory. Additionally, the fiber was not held straight in the chamber meaning that the light will be incident on the cladding at higher angles for greater bending curves. The result is that more loss will be experienced. As the metal is removed and the waveguide structure returns, these angles have less effect on the power transmission. One positive result is that the dip present in the first experimental curve is predicted by the theory. The second experimental curve shows a slight dip at around 100 hours but after the intensity had begun to increase, but it is not clear if this is the dip predicted by theory or a noise effect in the intensity of the sensor.

5.2 Al-Clad NaOH tests

Further testing of the aluminum-clad sensor was necessary to characterize its operation and to determine the optimal sensing length and manufacture technique. However, the corrosion process is a very slow process as can be seen from the first test where one micron of metal took approximately 10 days to reach steady state. Therefore, a means to speed up the testing process was needed. As described in Section 3.5.3, sodium hydroxide (NaOH) can be used as an aluminum etchant. Therefore, a test procedure using NaOH to remove the aluminum film and imitate corrosion was developed.

The method for fabricating the sensors also required modification because of the inconsistencies in removing the plastic cladding and applying the aluminum. A search was performed, and a commercially available aluminum-clad fiber was found. This fiber

had a 140 micron glass core and a 20 micron thick aluminum film applied around the circumference of the core. The film was pure aluminum which is not exactly the metal in the aircraft, typically aluminum alloys, but it did provide much information during the testing. The sensing region also needed input and output fibers, so a method to attach input and output fibers was developed which could also withstand the NaOH etchant.

5.2.1 Experimental Setup

The experimental setup used for the NaOH tests was a very simple setup. Figure 5.6 shows the basics of this setup. The NaOH solution was placed in a large beaker so that the fiber could be inserted into the solution. Multiple sources were used to test the effect of wavelength on the sensor operation. A HeNe laser was used at 633 nm, a 1300 nm laser diode was used and an LED at 850 nm was used. It should be noted that these experiments were performed prior to the theoretical model development. Therefore, the model will be used to compare to the experimental results for each wavelength investigated. The output intensity from the sensor was monitored using a power meter and recorded by hand along with the time. The photodetector used for the power meter was made from silicon for the 633 and 850 nm sources and germanium for the 1300 nm source.

5.2.2 Sensor Fabrication

The sensor consisted of three sections: the input fiber, the sensing region, and the output fiber. The input fiber and the output fiber were both chosen to be 100/140 multimode optical fibers with acrylate coating to protect them from the NaOH. The input and output fibers had to be spliced to the sensing fiber in such a manner as to insure a continuous and non-fluctuating power transfer. Also, the splices had to be protected to some degree from the NaOH. A two-step process was decided upon to insure that both of these criteria were met.

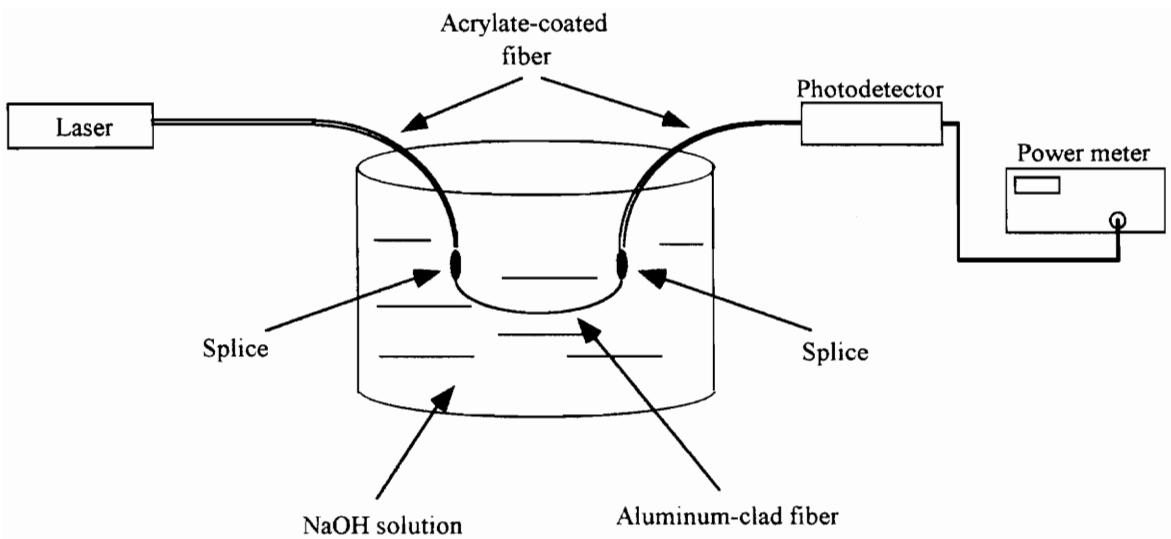


Figure 5.6. The setup of the NaOH etch tests for the aluminum-clad corrosion sensor.

Figure 5.7 shows a schematic of the splice used for both the input and output fibers. The first step was to insure the power transfer to and from the sensing fiber. The aluminum coating was removed from a section of the aluminum-clad fiber using an NaOH solution, and the end of the fiber cleaved and inserted into a 145 micron inner diameter silica tube. This end was epoxied to the tube using cyanoacrylate epoxy and then Devcon[®] 5-minute epoxy. The center of the tube was filled with an index-matching liquid to insure high power coupling, and a stripped and cleaved multimode fiber was inserted into the other end of the tube. The multimode fiber was bonded to the tube in a similar fashion as the aluminum-clad fiber. A large core tube was placed over the entire structure and bonded to the aluminum and acrylate coating of the input (or output) fiber. This tube was sealed with epoxy to insure that the NaOH did not enter the tube and affect the splice.

5.2.3 Experimental Results

A series of aluminum-clad corrosion sensors were fabricated using various lengths for the sensing region. The sensing lengths ranged from 50 cm to 250 cm in order to determine which sensing length responded better to the corrosion process. The first tests were performed using a 633 nm HeNe laser as the source. Plots of the output of the sensor versus time are shown in Figures 5.8 and 5.9 for 75 cm and 260 cm sensors, respectively. Both of these plots exhibit the dip in power that is predicted by the theoretical analysis. Also, the 260 cm sensor has a net increase in power of 12.5 dB while the 75 cm sensor has a net increase of only 6 dB. There is a noticeable difference in the time of response for the two sensors. This could be attributed to the percent solution of the NaOH. Since the amount of NaOH placed in the solution was not precisely measured, the overall pH of could differ between solutions. As described in Chapter 2, the pH of the solution has a direct effect on the corrosion rate with higher rates present for higher pH levels. Even small changes in the pH level will have an effect on the overall metal removal rate. This would cause the different time of response for each test.

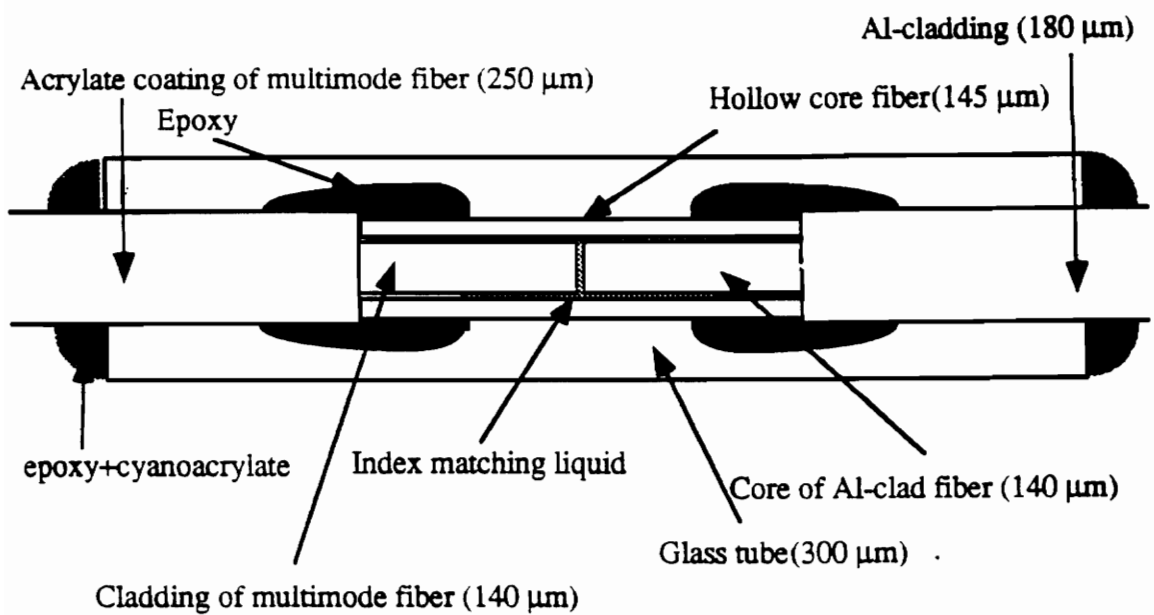


Figure 5.7. Schematic of the splice for the aluminum-clad corrosion sensor.

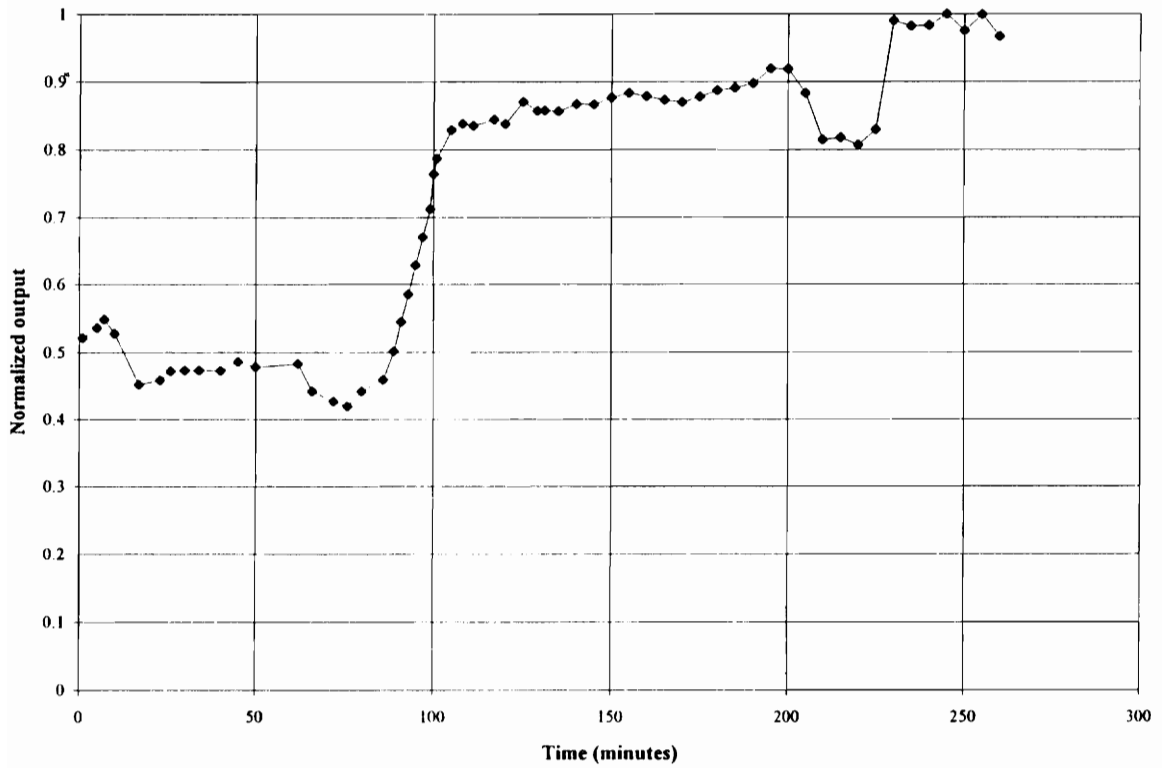


Figure 5.8. Power versus time for a 75 cm sensor using 633 nm light.

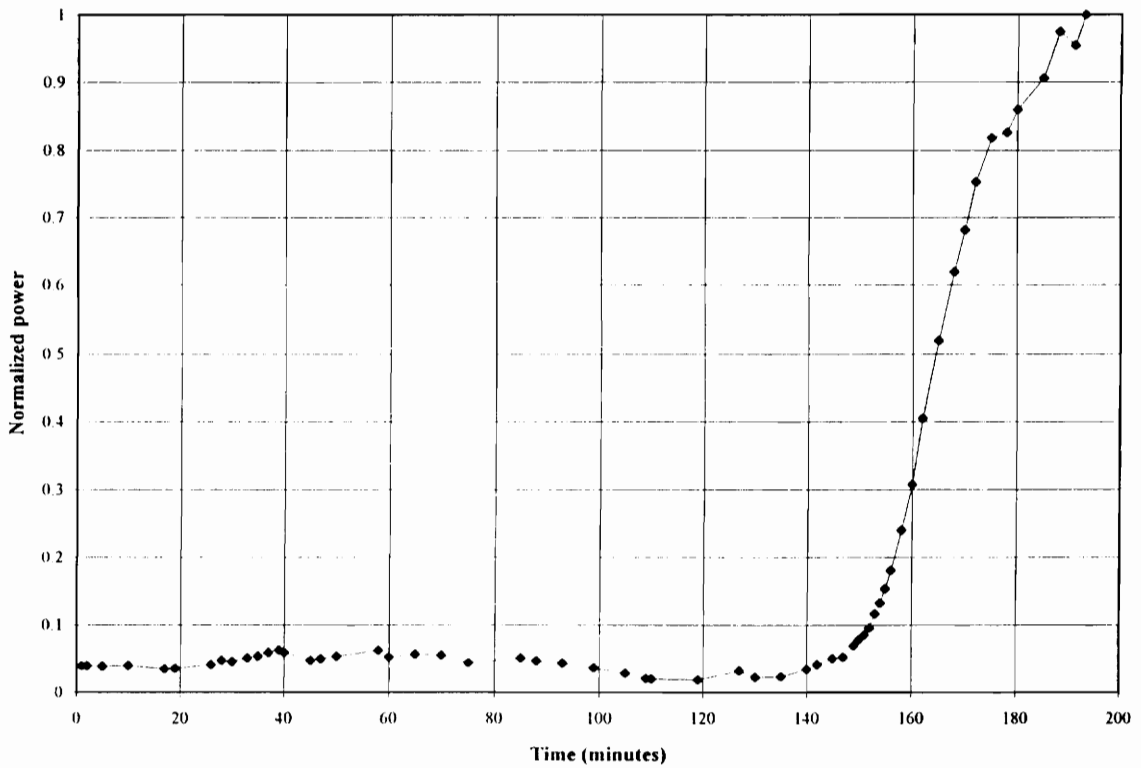


Figure 5.9. Power versus time for a 260 cm sensor using 633 nm light.

Another observation made from the data was the amount of fluctuation in the signal. This can again be attributed to the fact that the sensor was not held straight in the NaOH, but allowed to freely float and move during the test. As mentioned in Section 5.1, a small amount of bending will increase the loss of the metal-clad fiber before metal removal due to corrosion. Therefore, if the amount of bending changed during the test, the output power level would also fluctuate. The intensity output would change each time the sensor moved or the table the test was on was inadvertently bumped. The positive side of this is that none of these intensity changes were of the magnitude of the corrosion-induced change. This indicates that the sensor is fairly immune to these intensity variations which are present to some degree in most intensity-based sensing schemes.

The theoretical model was used with the source and sensing length conditions represented in Figures 5.8 and 5.9. The results are shown in Figures 5.10 and 5.11, respectively. Comparing the theoretical data with the experimental, it can be seen that the theoretical data predicts a total change in power level increase of approximately 1.5 dB, but the experimental data demonstrates a change in power level increase of 6 dB. Once again, this can be attributed to the bending of the fiber and the method of source injection. Also, the theory is an approximation, and it can be seen that this approximation may cause some error in the magnitude of the predicted signals. The shape of the curves is very similar for the theory and the experiment.

The second observation is that the thickness for the theoretical analysis was started at 0.1 microns whereas the actual aluminum started at a thickness of 20 microns. The fact that the shapes are so similar leads to two conclusions. First, the NaOH etch rate is probably not uniform as the thickness decreases. It is likely that the etching starts quickly, but as the aluminum dissolves into solution around the sensor, the NaOH can no longer etch the aluminum at the same rate. The solution was not agitated during the test, so the localized

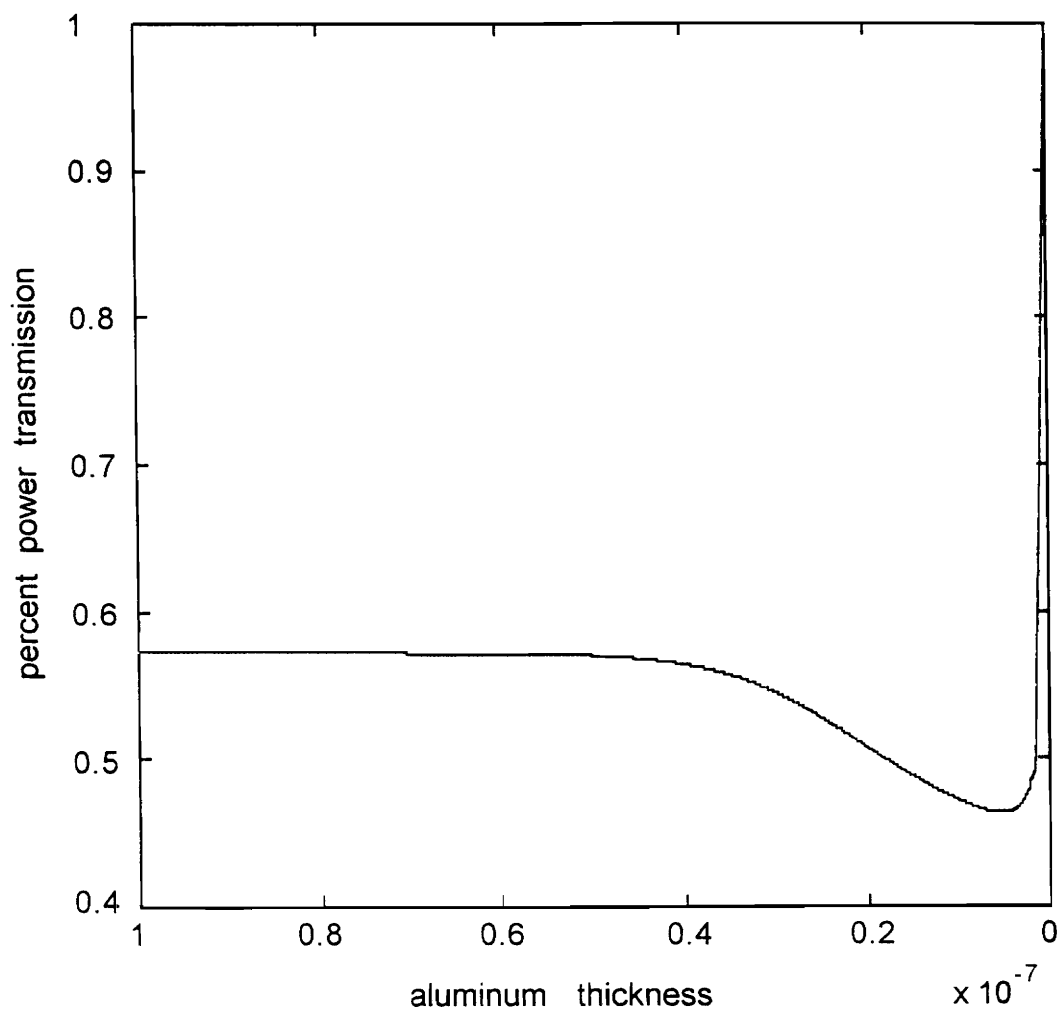


Figure 5.10. Theoretical data for power output versus thickness for a 75 cm sensing length using 633 nm light.

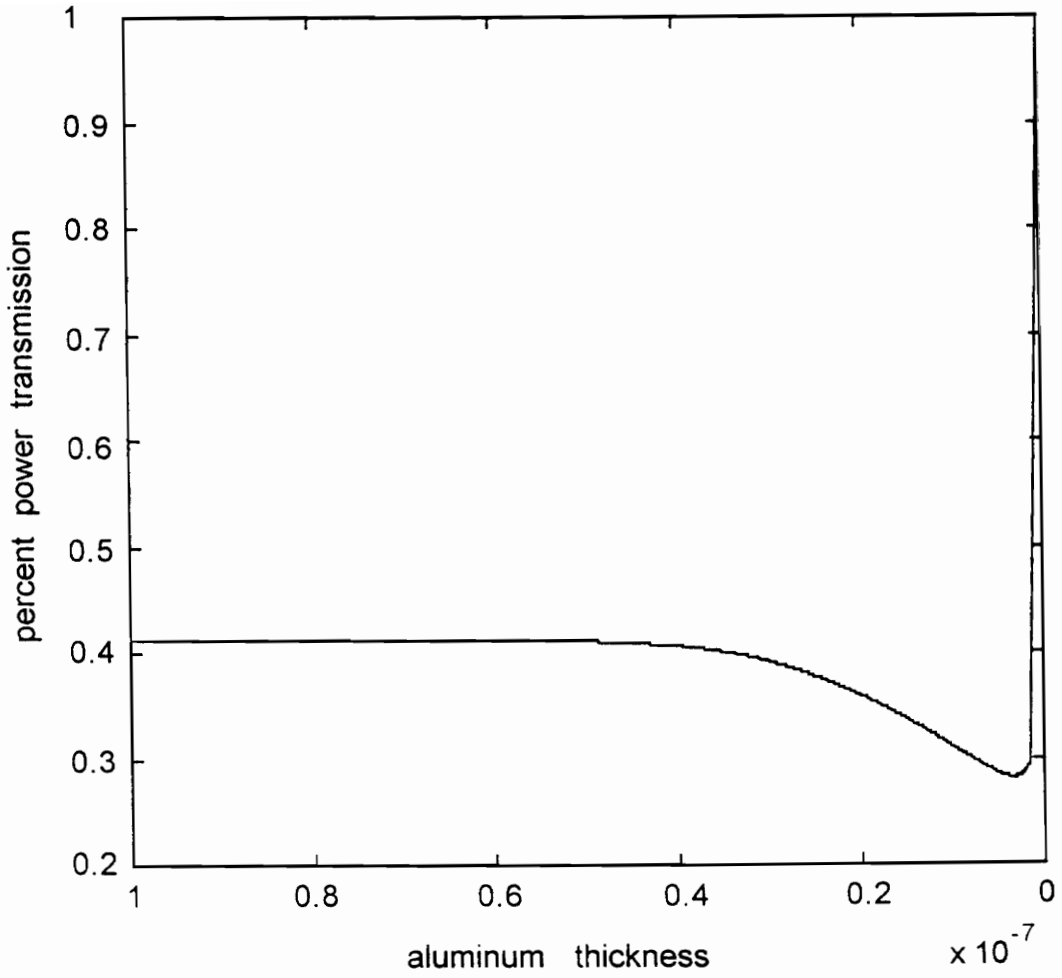


Figure 5.11. Theoretical data for power output versus thickness for a 260 cm sensing length using 633 nm light.

buildup of aluminum around the sensor would decrease the rate of removal for the remaining aluminum on the sensor. The second conclusion is that the ray approximation for the theory decreases the predicted thickness where power level changes can occur. That is, there is a certain thickness at which the fields no longer penetrate into the outer material, and are therefore no longer affected by changes in the outer parts of the aluminum. Below this thickness, the power level will rise as the thickness decreases. For normally incident waves, this thickness is on the order of the wavelength of the light being used. The theory presented here predicts this thickness to be around 0.05 microns. This discrepancy occurs because of the angle of incidence the light is assumed to have with respect to the metal film in the ray optics approximation. The angle is so close to 0° that the sine of the angle is very small and this is multiplied by the aluminum thickness to find the penetration of the light. The light in the fiber actually has normal field components that probably penetrate much more than this. This would cause the difference that is seen between the theory and the experiments.

Additional experiments were performed using a 1300 nm laser diode as the source. The laser was pigtailed to a single-mode optical fiber, so the input 100/140 fiber had to be mode filled using a mode scrambler in order to insure proper mode fill. The result for a 75 cm sensing length is given in Figure 5.12. A noticeable difference between the 1300 nm data and the 633 nm data is that the dip is greater in magnitude for the 1300 nm source. Figure 5.13 is a theoretical curve for the same physical configuration. The same conclusions about the theoretical analysis and the experiments can be drawn from this data as with the data from the 633 nm source. The theory and the experimental data do show the same trend where the dip is more gradual in the beginning than for the 633 nm data. This does not have any significance to the operation of the sensor.

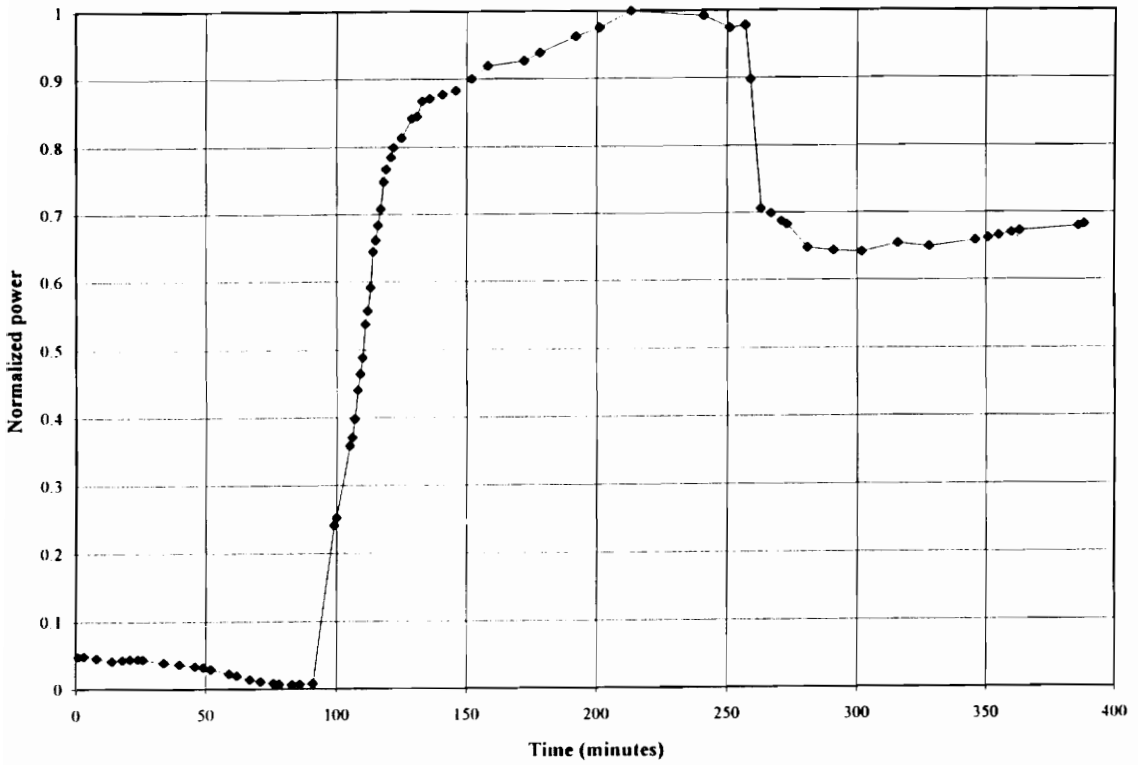


Figure 5.12. Experimental data for a 75 cm sensing length and a 1300 nm source.

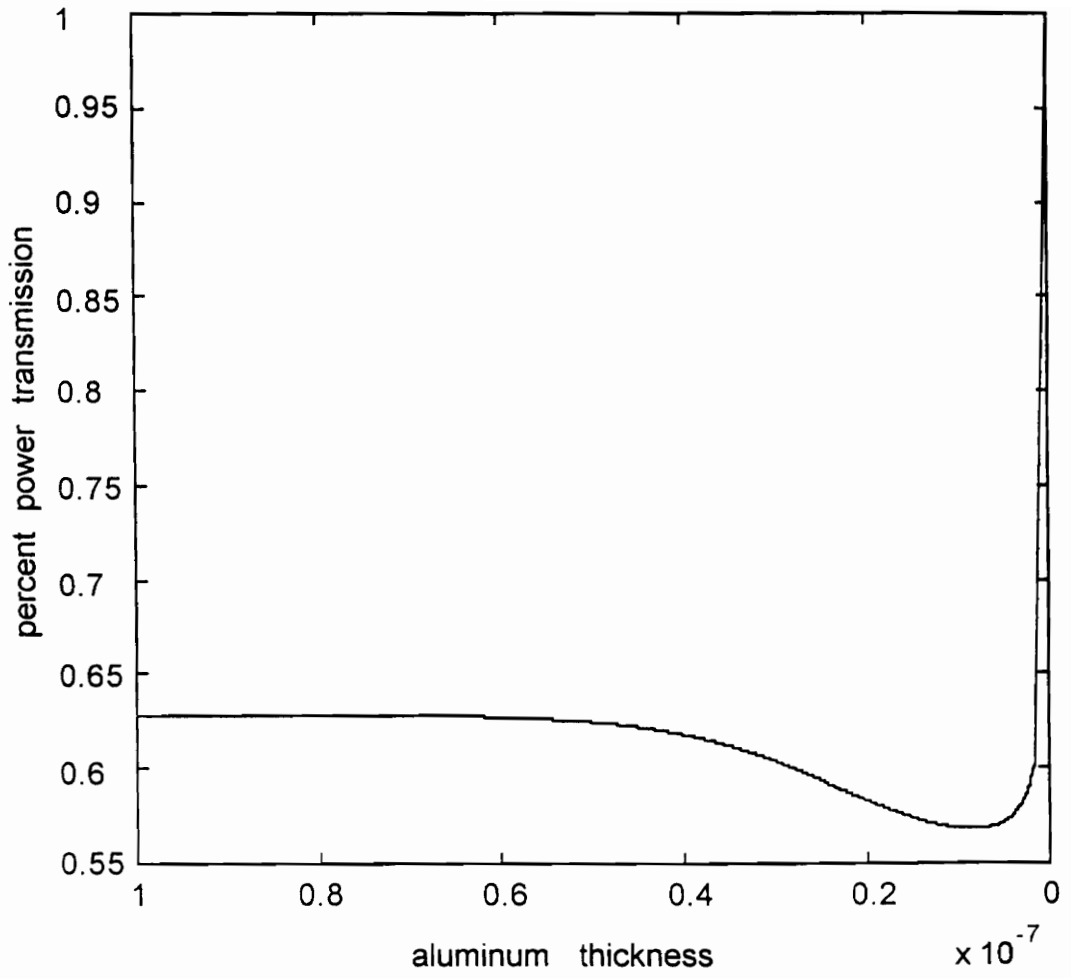


Figure 5.13. Theoretical curve for a 75 cm sensor and a source at 1300 nm.

The final experiments performed using the NaOH setup on the aluminum-clad corrosion sensor used an 850 nm LED as the source. This source was chosen because it was a practical choice for a commercial type sensing system. It offered 50 microwatts of power coupled into a 100/140 micron fiber, low cost and easy integration into a prototype system. The wavelength also allows the use of a silicon photodiode as opposed to a germanium photodiode. The silicon photodiode offers lower cost and lower noise than its germanium counterpart. Figure 5.14 shows the output from a 100 cm sensing length corrosion sensor using the 850 nm LED. It can be seen that the output appears much more smooth for the 850 nm LED than for either of the two laser sources. One possible explanation for this difference is that the LED has a broad range of input angles whereas the laser outputs are very confined immediately out of the laser itself. Small bends or movements in the fiber or the table would have less effect on the LED system because of proper mode filling. Another interesting point in this graph is the sudden step-like increase in power and then gentle increase from that point on. Part of the cause may be the frequency of data collection. A second explanation which ties into a previous remark is the possibility of the aluminum in solution saturating the region of the NaOH around the sensor and slowing down the etching process. The theoretical analysis was run on the 850 nm source for the same sensing length and is presented in Figure 5.15. The spread in wavelengths of the LED was not accounted for in the theoretical analysis, but is not expected to have much effect on the outcome because the index change for aluminum in the 50 nanometers around the 850 nm center of the LED is less than 2%. This low variation in index of refraction indicates that the reflectivity changes for the spread of wavelengths could be accurately approximated by using only the center wavelength in the theoretical model. Figure 5.15 shows that the output is very similar to the other theoretical results.

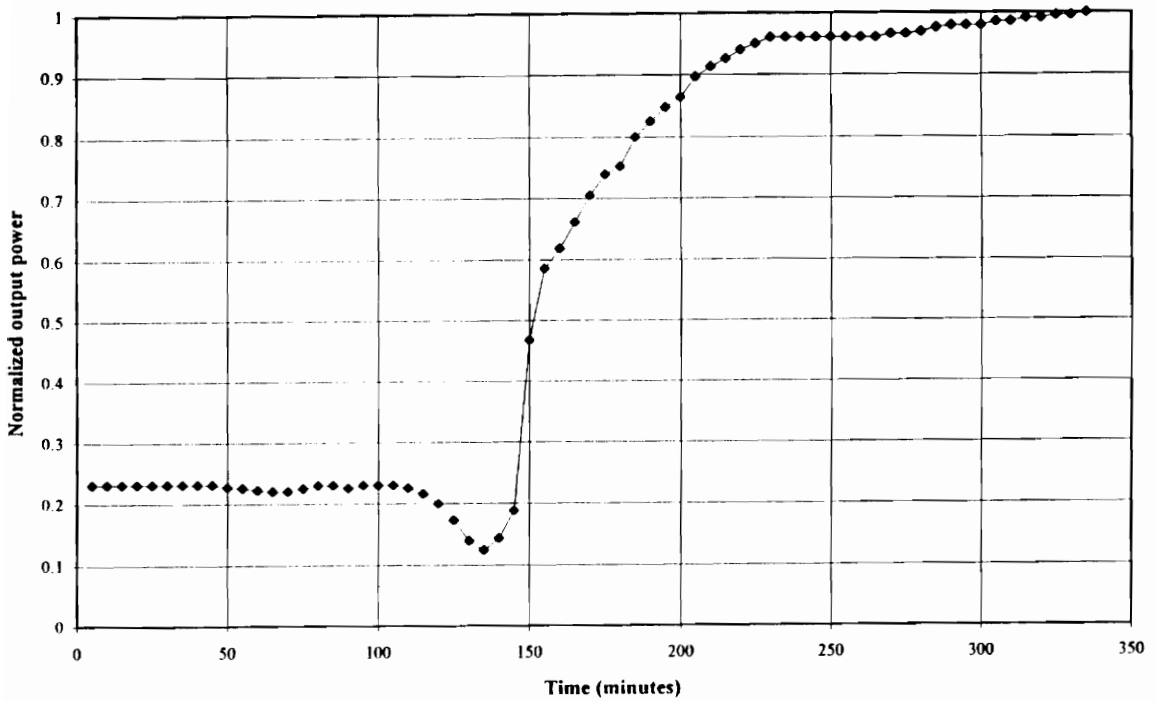


Figure 5.14. Experimental curve for a 4 inch sensor and 850 nm source.

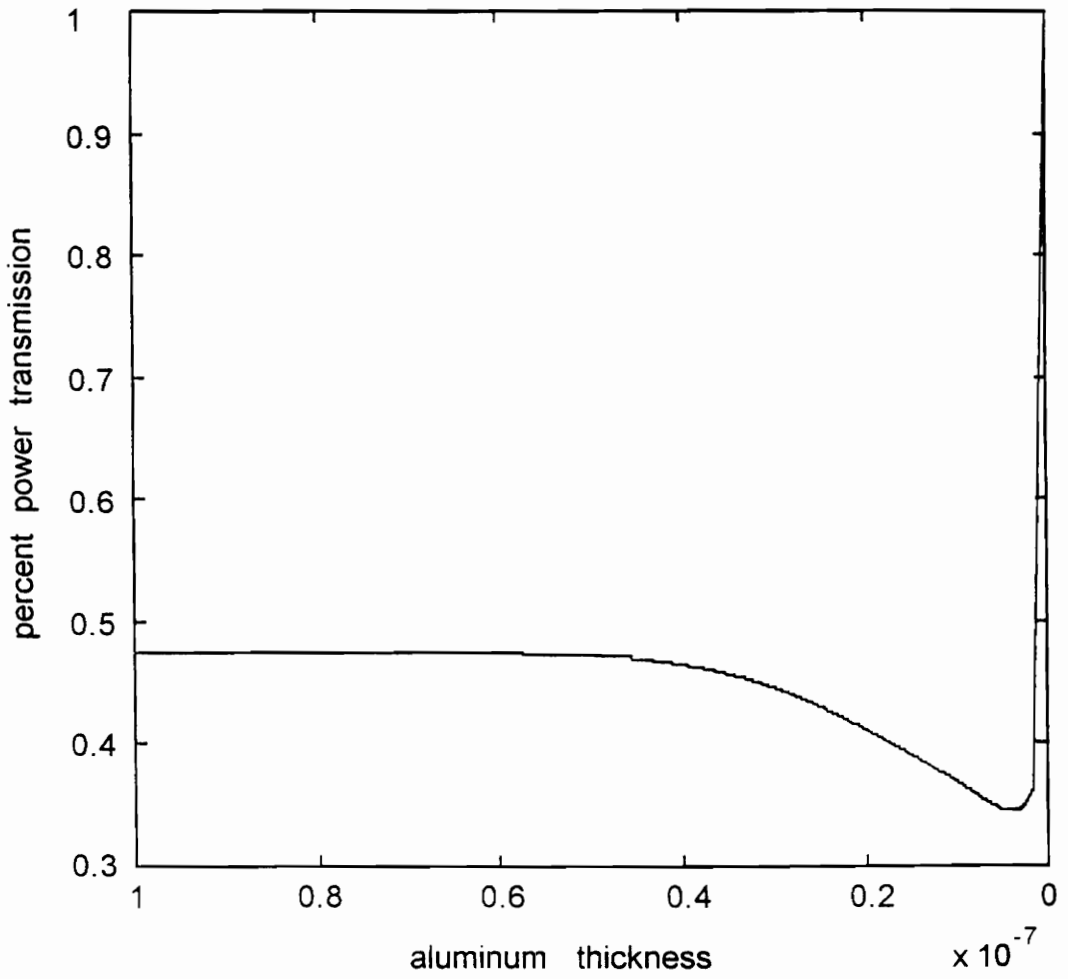


Figure 5.15. Theoretical curve for a 100 cm sensor at 850 nm.

These results show that there is very little difference between the various wavelengths in terms of output shape versus metal thickness. The overall power increase changes between wavelengths for a certain sensor length, but all increase magnitudes are much greater than the magnitude of any noise in the system due to intensity variations. The only decision factors would then be system factors. As mentioned above, the 850 nm LED offers three important advantages over other sources: low cost, high power coupling and the use of silicon photodiodes as opposed to germanium. Therefore, this source was chosen for all future research.

Additionally, the spliced sensor geometry was very difficult to make repeatably and with any mechanical strength. Sensors were fragile and had to be handled with great care. Also, the splices were bulky and added stress to the aluminum-clad sensing region causing many breaks during testing. For aircraft applications, the sensor will be attached to the metal in the region where corrosion is to be sensed. A robust sensor will be necessary for this attachment. The end result was a decision to research other manufacturing methods for the aluminum-clad corrosion sensor.

5.3 Sputter-Coated Sensor

The method chosen for future manufacturing was a sputter coating scheme. It was thought that if a standard step-index multimode fiber had its silica cladding removed, a method could be devised to cylindrically sputter a uniform thickness of aluminum, or possibly an aluminum alloy, onto the fiber. In order to coat the circumference of the fiber uniformly, a modification to an existing sputtering system was needed.

5.3.1 Sensor Fabrication Unit

A radio frequency (RF) magnetron sputtering system was custom designed and built to provide the ability to coat the optical fibers with the metal. Because the sputtering

chamber must be maintained at a high vacuum ($<10^{-6}$ Torr), a magnetic coupling device was utilized to allow position control of the fiber in the chamber without actually having access to the fiber or fiber holder. A fiber holding assembly was designed to operate with the magnetic coupler. Figure 5.16 shows a schematic of the sputtering system vacuum chamber and the fiber holder. The fiber holder consists of a specially designed mounting sleeve which extends over the rod coming from the magnetic coupler and a fiber chuck. A hole in the side of the sleeve was made for the excess fiber. Two mounting screws held the rod and the fiber chuck. Special hollow tubes were attached above and below the vacuum chamber to allow the movement of the fiber holder over a length of approximately 0.5 meters. The top tube holds the magnetic coupler and the rod extending to the mounting sleeve. The bottom tube provides a space for the coated fiber to move into without the need for bending or coiling. The mechanism is to simply move the fiber from the top side of the chamber through to the bottom.

To insert the fiber holder into the chamber, the RF magnetron source is removed. The fiber mounted in the mounting sleeve is inserted through the hole left by the magnetron source and connected to the rod from the magnetic coupler. A special weight is attached to the bottom of the fiber to maintain a straight line through the vacuum chamber. This weight is simply a shortened fiber chuck.

The material to be sputtered is ejected from the single magnetron source. Because the distribution of the sputtered species in the chamber is non-uniform, it was desirable to develop a positioning system for the magnetic coupler which allowed simultaneous rotation and translation of the fiber in front of the magnetron source. A computer controller was decided upon to provide simultaneous independent control of the rotation and translation. Figure 15.17 is a block diagram layout of this computer controller.

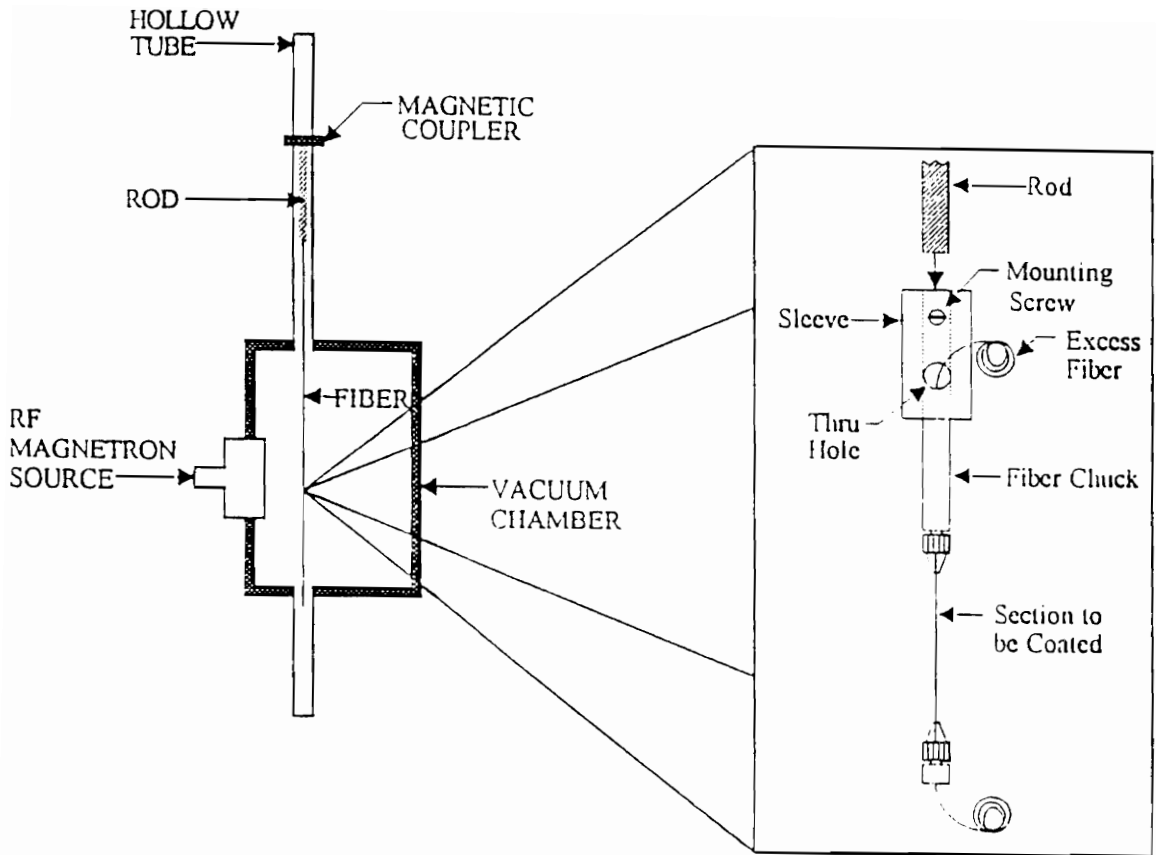


Figure 5.16. Schematic of the vacuum deposition chamber and fiber holder.

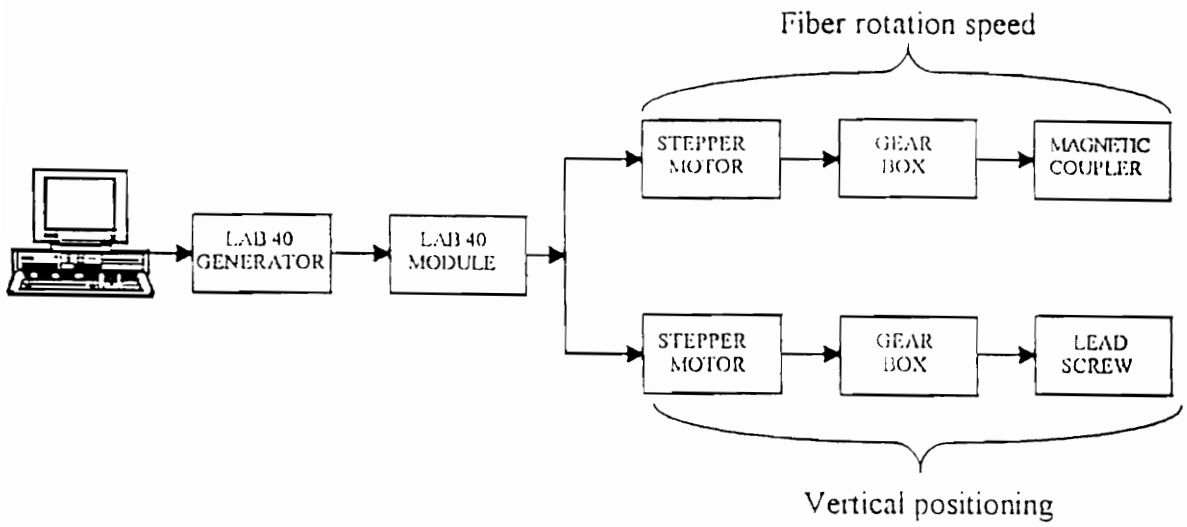


Figure 5.17. Block diagram of the positioning system.

A LAB 40 generator A/D card was purchased and installed in an IBM PC. The card works in conjunction with an external LAB 40 function module designed specifically for driving stepper motors. Software included with the LAB 40 function module allows the control of parameters such as stepper motor speed, direction, number of steps, and mode of operation (single phase or dual phase). A 20:1 reduction gear box was used between the stepper motors and drive mechanisms to increase the positioning accuracy. For this setup, one complete revolution of the optical fiber in the deposition chamber can be resolved into 800 discrete steps of the stepper motor.

To control the magnetic coupler with the computer system, a lead screw runs from a platform at the top of the sputtering unit down to a second platform which supports the magnetic coupler. Translational positioning of the magnetic coupler is controlled using the stepper motor at the top of the sputtering system as shown in the photograph in Figure 5.18. The stepper motor/gear box assembly rotates a small gear attached to the lead screw which in turn lowers the platform and therefore the magnetic coupler. Rotation of the magnetic coupler and therefore the fiber inside the sputtering chamber is controlled with a second stepper motor/gear box assembly attached to the moving platform. The gear box is attached to an 0.2 meter gear mounted on top of the magnetic coupler. Using this setup, the fiber in the chamber can be rotated at speeds up to 2 revolutions per minute, or as slowly as desired.

5.3.2 Sensor Fabrication

The sensor design consisted of a standard step-index multimode optical fiber with a region of its cladding removed and replaced with aluminum or aluminum alloys. Figure 5.19 shows this concept. Using this design, the fiber is continuous, no splices are needed, and the sensor manufacturing should be repeatable. The sensor diameter is maintained below the fiber coating diameter and the mechanical strength is maintained. What was necessary was a method to remove the cladding only in a specific region.

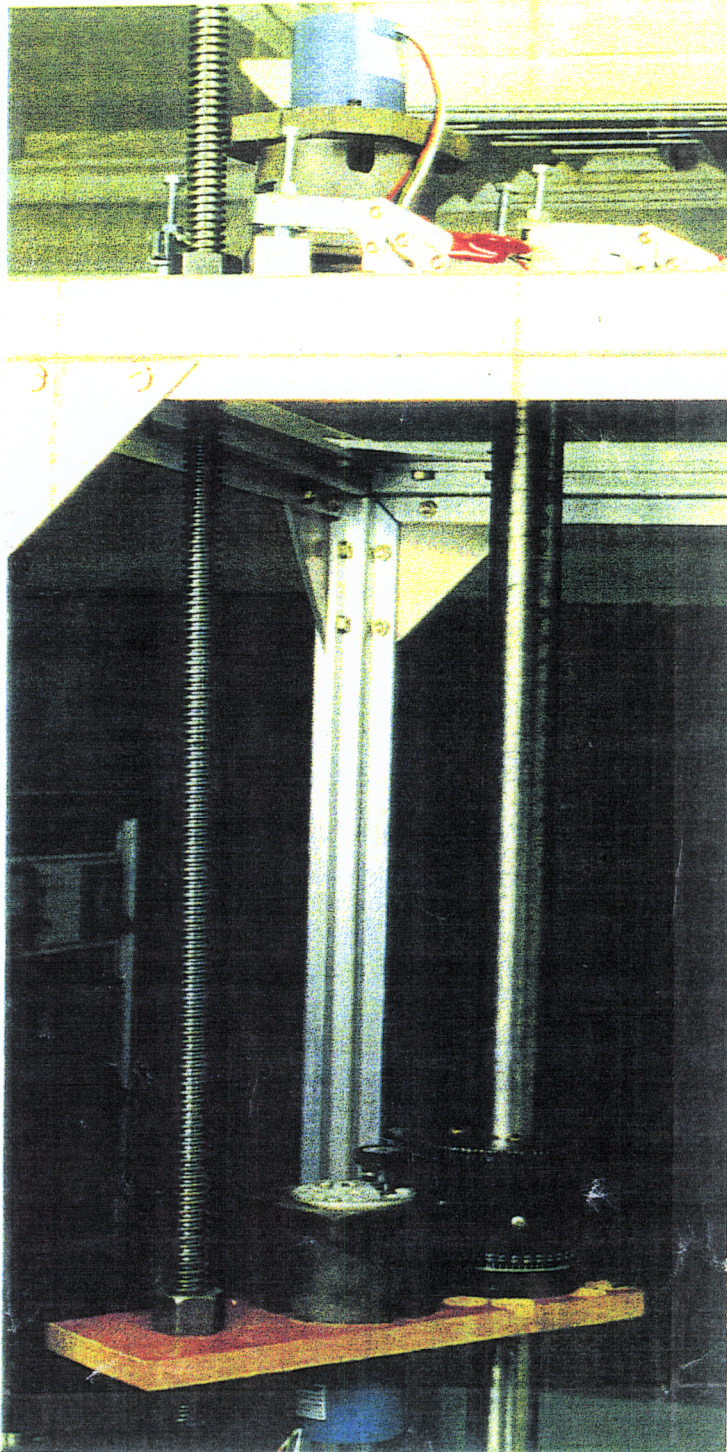


Figure 5.18. Photograph of the positioning system.

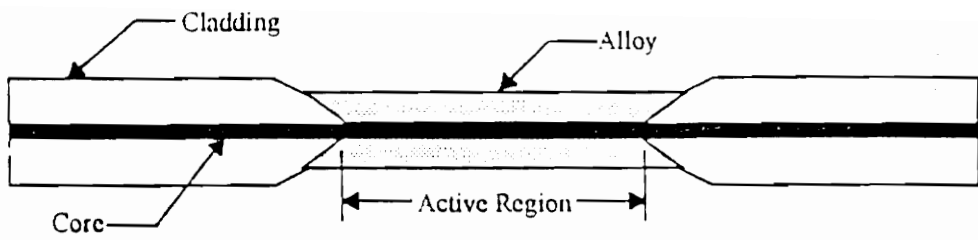


Figure 5.19. The in-line aluminum-clad corrosion sensor.

The optical fiber chosen for use as the corrosion sensor fiber was a 100/140 micron core/cladding step-index multimode fiber. The fiber was coated with a 500 micron diameter acrylate coating. A special holder was designed to hold a number of fibers in a pre-chosen radius as shown in Figure 5.20. The slots in the sides of the holder allowed the placement of 25 fibers and guaranteed that all the loops were identical. Two meter long fiber sections were placed in the holder and taped in place. The loops allowed the free flow around the fibers of the chemicals used to etch the coating and cladding. Figure 5.21 is a photograph of the holding fixture fully loaded with fibers. The chemical method for coating and cladding removal was chosen because the use of razor blades to remove the coating could not provide the repeatability of stripped lengths desired for the sensor. Also, the razor blade would usually nick the fiber, weakening it and reducing the overall mechanical strength of the fiber.

To protect the operator from the chemicals being used in the etching process, a special etching system was designed and fabricated. Figure 5.22 shows a schematic of this system which includes a tank, gravity feed bottle, hoses, and spigots all made from Nalgene[®], a polyethylene material resistant to hydrofluoric acid (HF) and other acids used in the etching process. For additional safety, the fiber platform is placed in the tank, and the entire apparatus is placed under a fume hood to remove any toxic vapors. A photograph of the completed etching system is shown in Figure 5.23.

A two-step chemical etching process was chosen to remove the acrylate coating on the fiber. Because the acrylate was relatively thick (>200 microns) the fiber manufacturer recommended a bath of nitric acid to soften the coating followed by a bath of methylene chloride to remove the coating from the silica glass fiber. The process was defined as a bath in nitric acid for 5 minutes followed by a 5 minute bath in the methylene chloride.

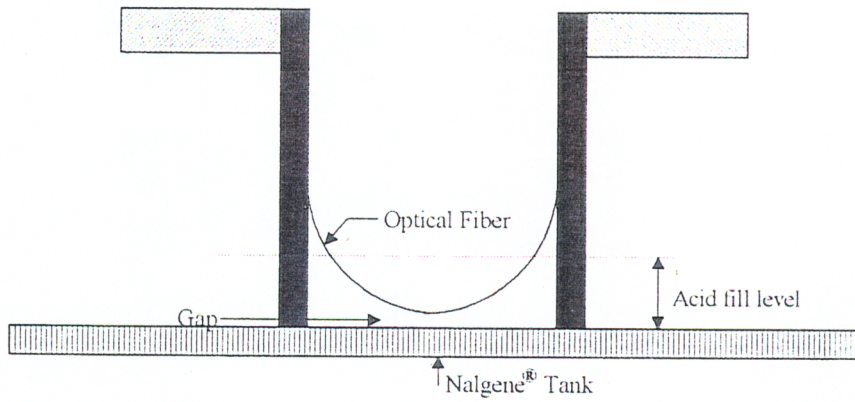


Figure 5.20. The platform for mounting optical fibers for etching.

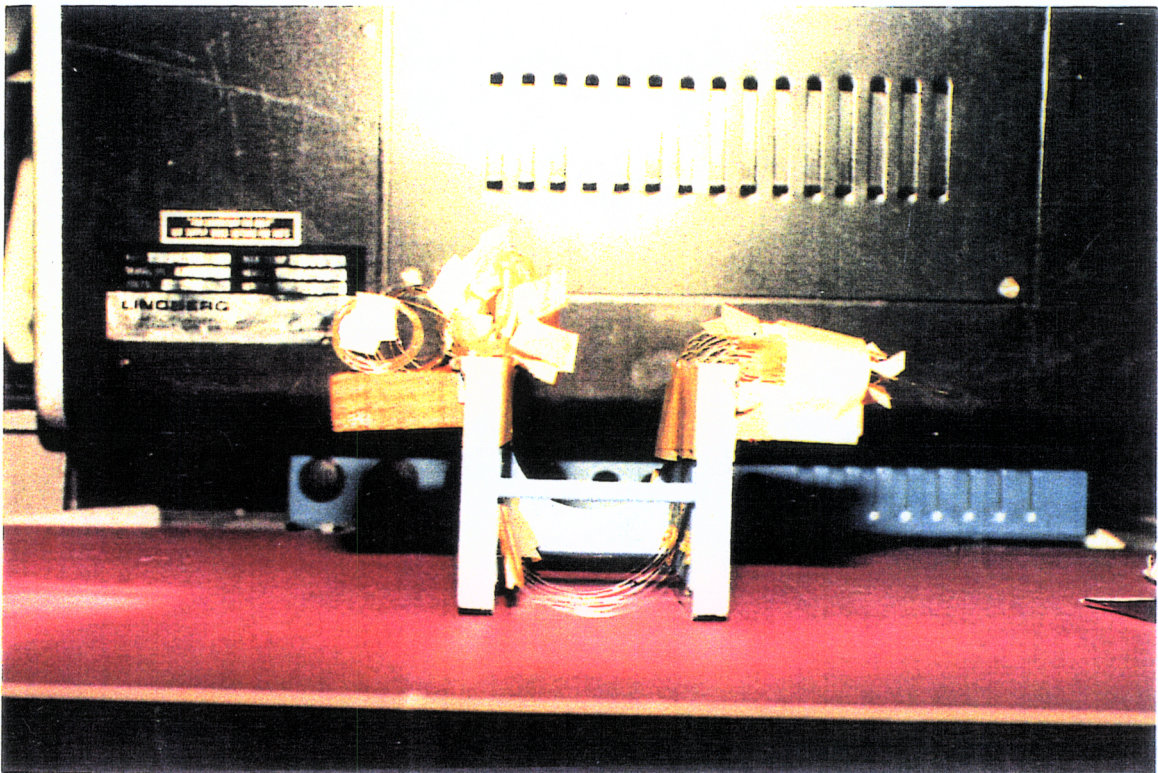


Figure 5.21. A photograph of the platform with loaded fibers.

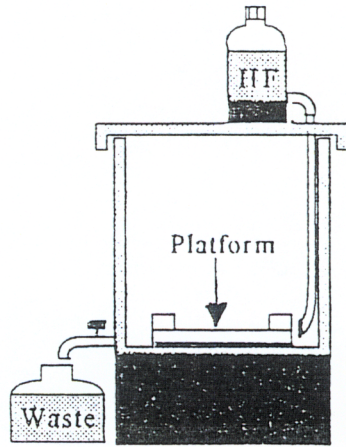


Figure 5.22. A schematic of the etching assembly.

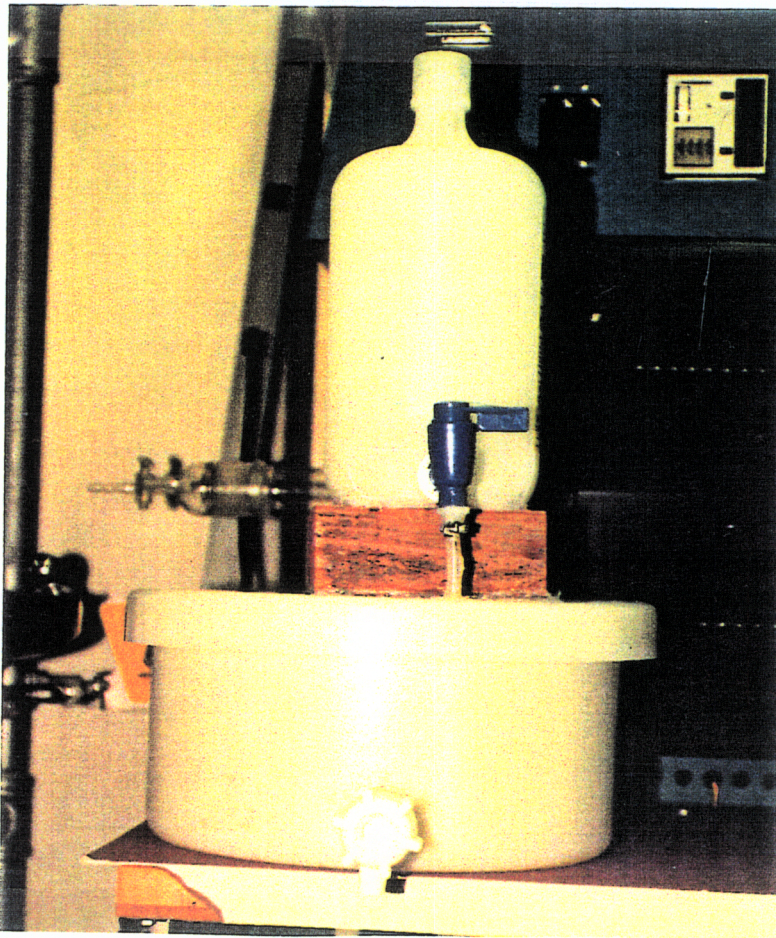


Figure 5.23. Photograph of the completed etching assembly.

To remove the silica cladding, hydrofluoric acid was used. Previous tests have demonstrated an etching rate of 3.3 microns/minute for silica fibers immersed in HF. Using this value, an etching time of 6 minutes was chosen to remove the 20 micron thick cladding. The tank was then flooded with deionized water to neutralize the acid. The final step was to place the fibers and holding fixture in a shallow tray of ethyl alcohol to remove any residual moisture from the fibers. The fibers were then allowed to dry, removed from the holder, and placed in a dessicating chamber for storage.

One problem did surface while using the aforementioned etching process. The etch rates varied slightly depending on the environmental conditions and the age of the acid. As the final fiber diameter was of prime importance, a method to actively monitor the thickness during the etching process was developed. Test fibers, short lengths of stripped fibers, were placed in the chamber along with the sensing fibers. These fibers were removed periodically during the etching process to monitor the fiber diameter. This information was then used to accurately determine when to rinse the fibers.

5.3.3 Sensor Analysis

As mentioned earlier, the actual metal used in the aircraft which are the primary end user for this initial corrosion sensor are aluminum alloys. However, to this point, only pure aluminum had been available for use on the fibers. With the development of the sputter-coating chamber, it was possible to coat aluminum alloys directly onto the fiber surface. After discussions with personnel from Boeing Corporation, two alloys were determined that are primarily used on aircraft: alloy 7075 and alloy 2024.

The first concern was whether the alloys would sputter onto the fiber and maintain their respective compositions. Therefore, both alloys were sputter-coated onto prepared optical fibers and tested using a scanning electron microscope (SEM) and energy

dispersive X-ray spectroscopy (EDAX) analysis. These tests were designed to provide information about the microstructure and composition for the sputtered films.

The first coating to be tested was the 7075-T6 alloy. The alloy was deposited in an argon atmosphere at an RF power of 60W and 20 mTorr pressure. An SEM photograph was taken of the surface and is shown in Figure 5.24. The photograph shows a relatively large grain size, approximately 1.5 microns, which is due to the high RF power. The energy of the sputtered species has a direct affect on the grain size of the sputtered film. The smaller the grain size, the better the adhesion of the film to the fiber. For this sputtering attempt, a grain size of 1 micron was the target value.

The EDAX analysis was performed to provide compositional information about the alloy to insure that the elemental percentages remained the same as the bulk alloy. Figure 5.25 is the spectral analysis provided by the EDAX. The primary peaks are labeled in the spectrum. Any peaks that are not labeled have been verified as secondary peaks for the Al, Zn, Mg, Cu, and Cr. The chemical composition of the film was determined and is presented in Table 5.1 with corresponding expected values for the percentages. the expected values are the industry accepted percentages.

Table 5.1. Aluminum alloy 7075.

Element	Predicted	Actual
Al	90%	94.66%
Zn	5.6%	1.73%
Mg	2.5%	3.47%
Cu	1.6%	0.14%
Cr	0.3%	--



Figure 5.24. SEM photograph of the 7075 sputtered film.

02-NOV-93 17:10:35 EDAX READY
RATE= 1340CPS TIME= 120LSEC
FS= 1393CNT PRST= 120LSEC
A =A1 7075

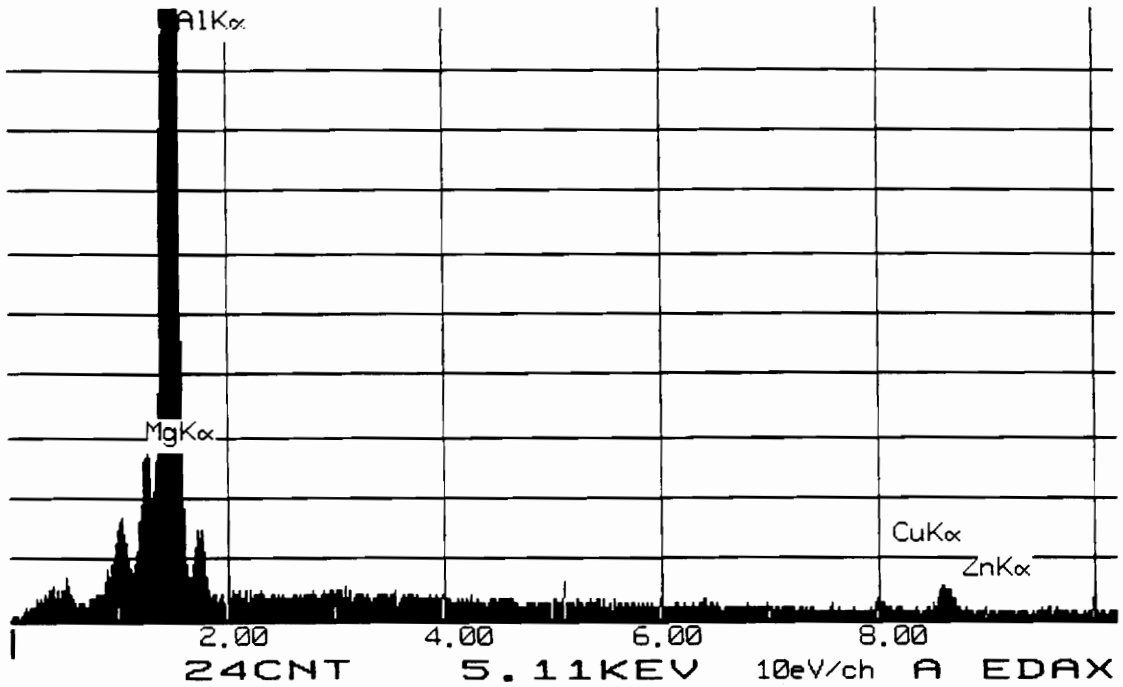


Figure 5.25. EDAX spectral analysis for the 7075 film.

The percentages shown in Table 5.1 demonstrate that the percentages fall within accepted values for the 7075-T6 alloy and the measurement capability of the EDAX system. Figure 5.26 is a color composite of the surface of the film indicating the distribution of the elements in the sputtered film. As can be seen from this composite, the elements are dispersed uniformly throughout the film demonstrating that the alloy was successfully deposited onto the fiber.

The aluminum alloy 2024-T4 was then sputter coated onto the prepared fiber. For this coating, an RF power of 40W was used at a pressure of 16 mTorr. The power and pressure were reduced to reduce the grain size and promote a more amorphous film on the fiber. The SEM photograph of the film is shown in Figure 5.27 with the same magnification as the photograph in Figure 5.24. This photograph clearly indicates the decrease in grain size (less than 1 micron) resulting from the drop in power and pressure. The EDAX analysis was also performed to determine the composition of the film. Figure 5.28 shows the spectrum of the 2024 film. The results are compiled in Table 5.2.

Table 5.2. Aluminum alloy 2024.

Element	Predicted	Actual
Al	93.4%	97.4%
Cu	4.5%	2.2%
Mg	1.5%	--
Mn	0.6%	0.4%

Once again, the percentages are within acceptable ranges to conclude that the composition is that of aluminum alloy 2024. Figure 5.29 shows the color composition of the film. As with the 7075 alloy, the film of the 2024 alloy has a properly amorphous distribution of elements to be classified as an alloy.

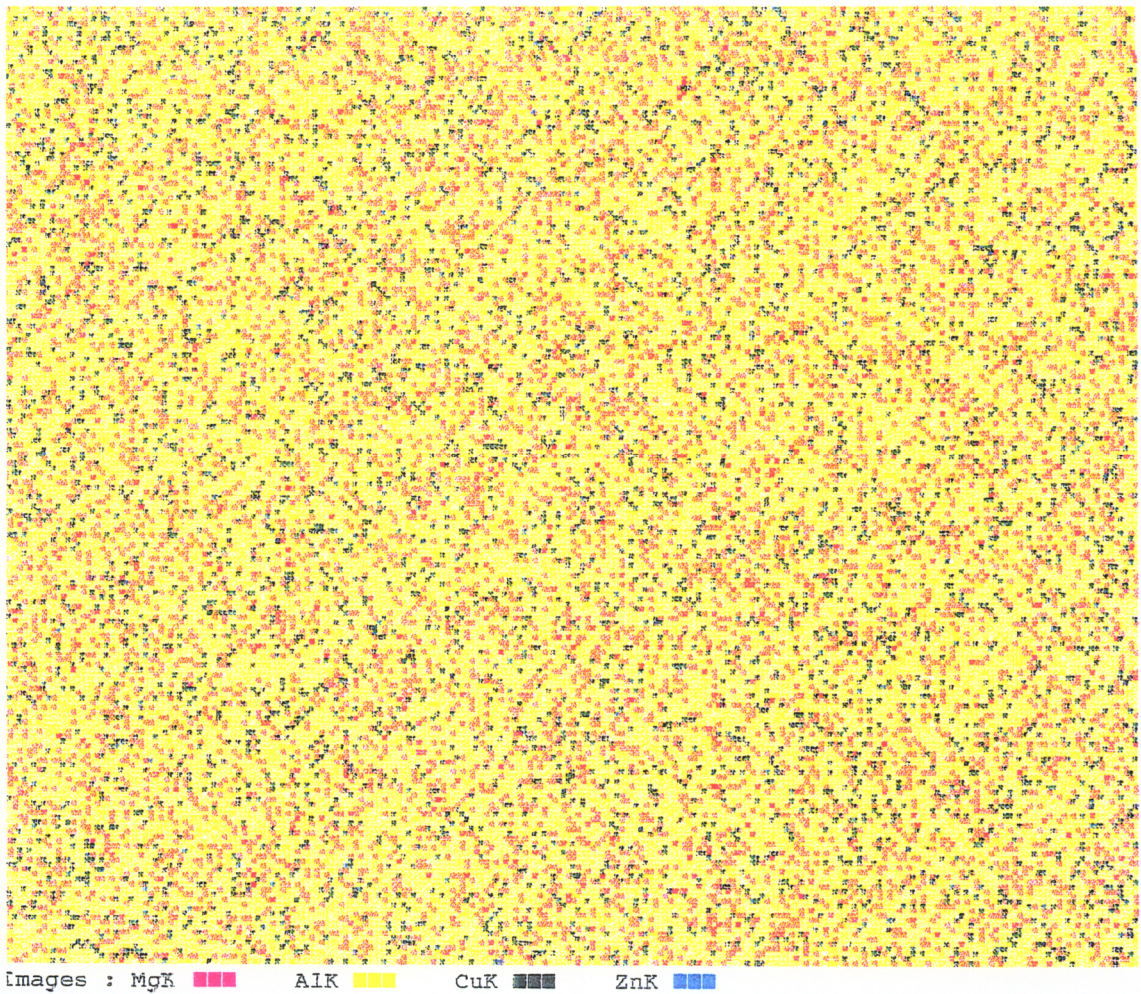


Figure 5.26. Color composite showing the distribution of the elements in the film.

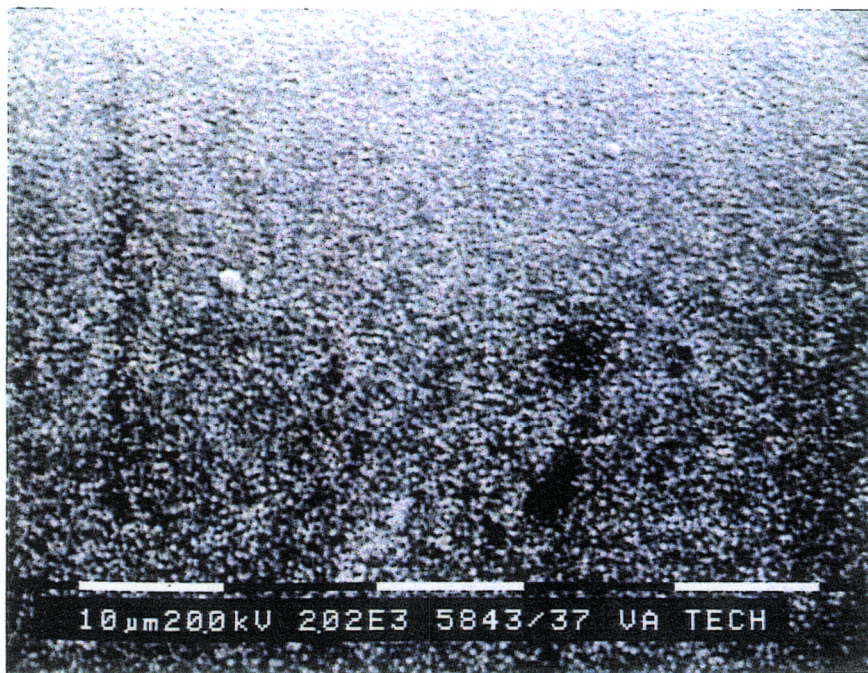


Figure 5.27. SEM photograph of the sputter coated 2024 film.

29-OCT-93 09:53:19 SUPER QUANT
RATE= 958CPS TIME= 69LSEC
FS= 1345/ 1345 PRST= 120LSEC
A =Al alloy 2024

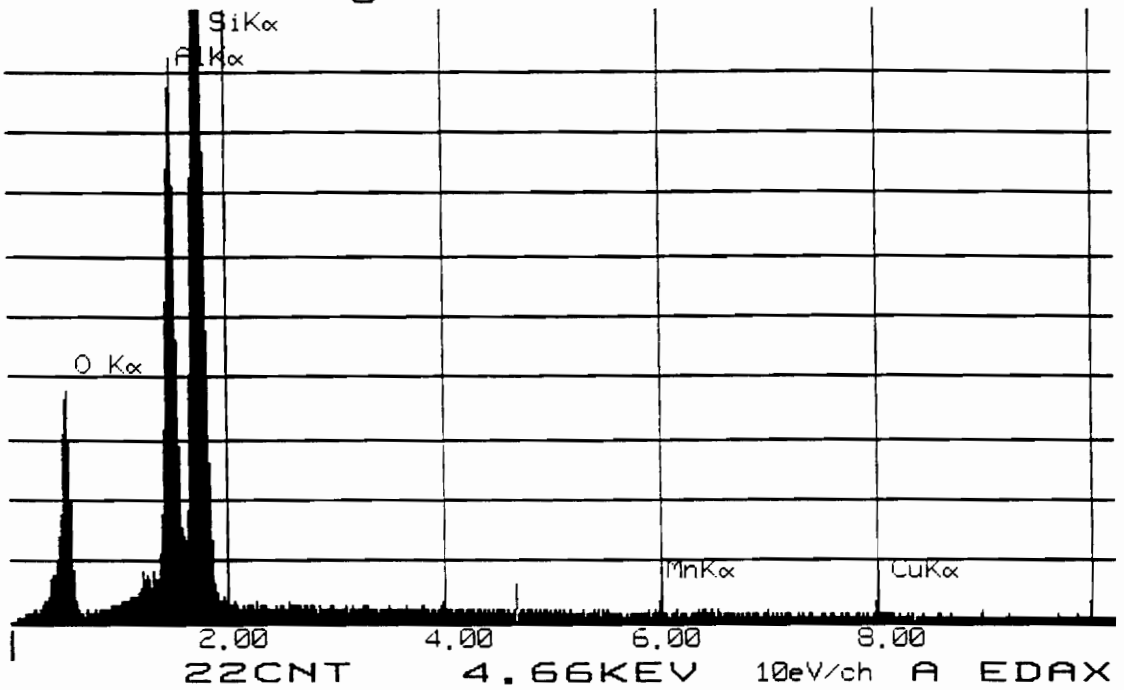


Figure 5.28. Spectrum of the 2024 film.

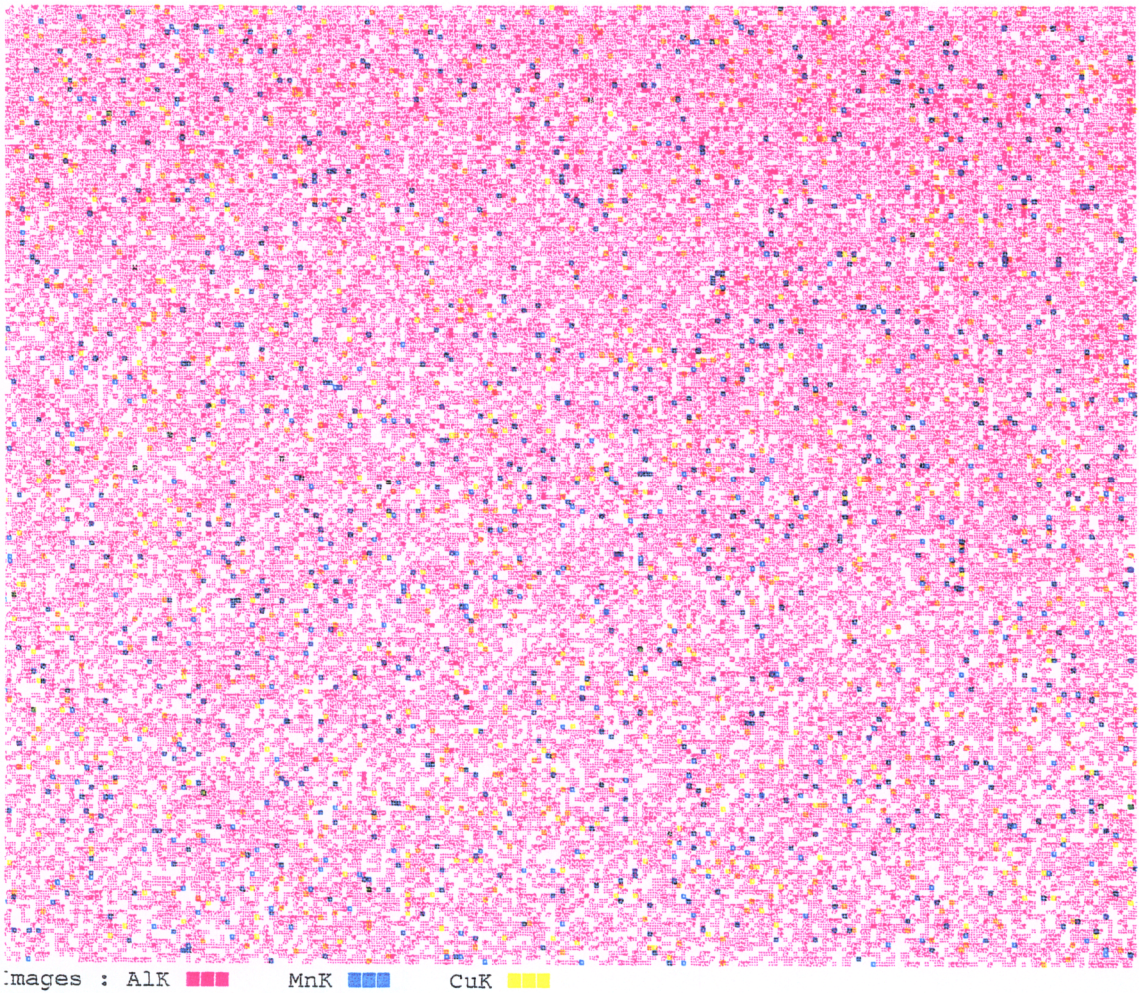


Figure 5.29. Color composition indicating element distribution for the 2024 film.

5.3.4 Sensor Fabrication and Testing

A sensor testing system was designed and fabricated using 850 nm LEDs and silica photodiodes. Two units were fabricated, a source unit and a detector unit. Each unit can support six channels and the source unit provides both sensing signals and reference signals. Figure 5.30 is a system level schematic of this new sensor signal processing system. The idea behind this system is to develop a prototype processing system which might mirror a future product. The six channels were chosen to allow several sensors to be tested simultaneously. The output from the detector box is designed to be fed into a computer via an A/D board as shown in Figure 5.30. The sensors are connectorized and plugged into the source and detector boxes allowing maximum interchangeability and flexibility for testing even more sensors.

A series of sensors were fabricated over a period of several weeks. Each sensor took two days to fabricate: one to apply vacuum to the sputtering chamber and one to apply the coating. These sensors were tested in turn with little success in achieving the outputs seen in the past. After further investigation, it was found that the fiber used was a graded index fiber instead of a step index fiber. This would tightly confine the modes to the core of the fiber and allow very little interaction with the aluminum film. Also, it was discovered that the etching process may not have been continued for a proper amount of time and a small amount of cladding was left on the fiber. This would further confine the light to the core and reduce to negligible amount the amount of interaction with the aluminum cladding.

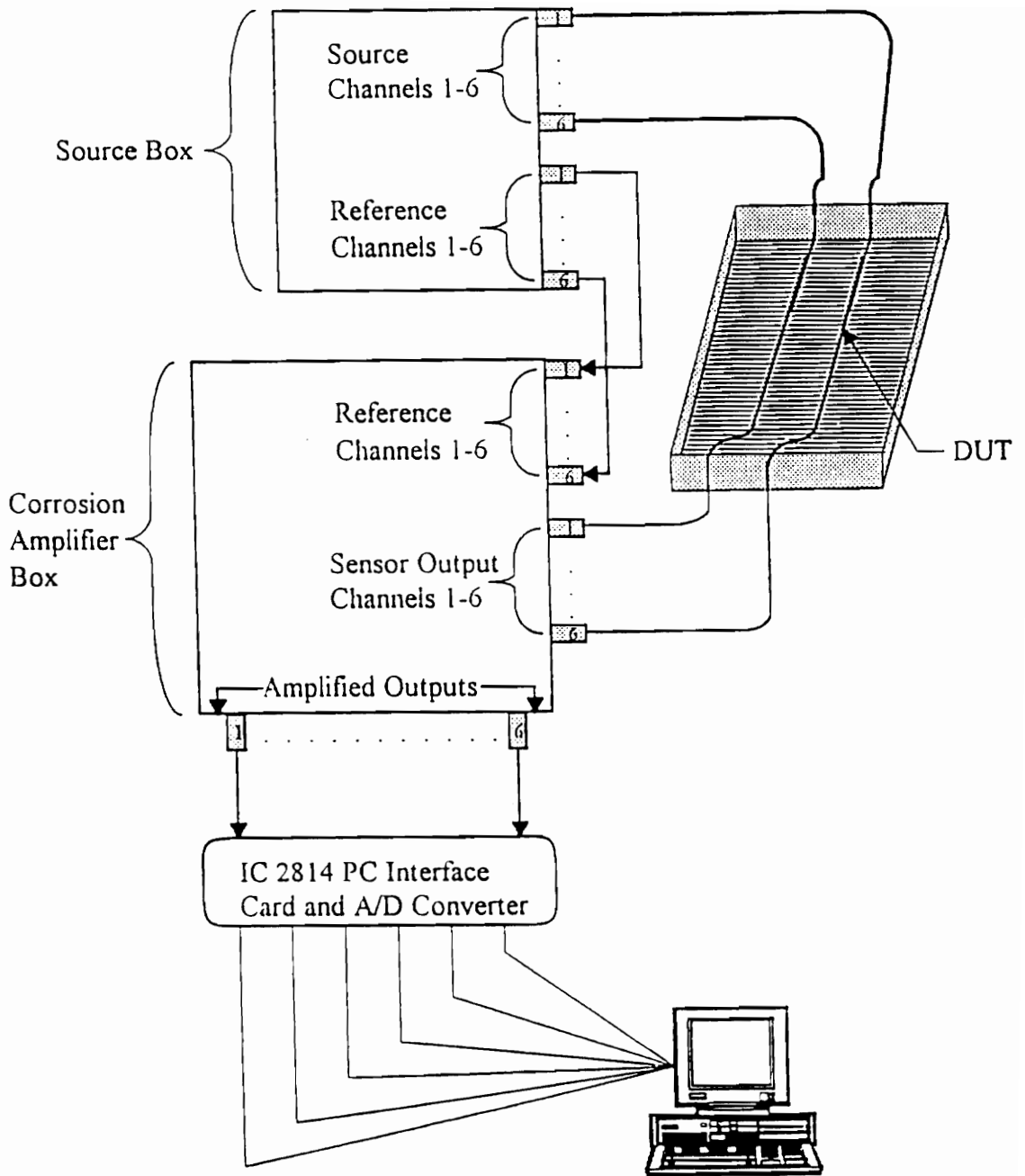


Figure 5.30. Corrosion sensor test setup. DUT: device under test (aluminum-clad corrosion sensor).

CHAPTER 6: DISCUSSION

A series of potential optical fiber-based corrosion sensing techniques have been presented. The majority of these techniques had one or several problems associated with them that eventually led to their removal from further consideration as a corrosion monitoring technique. Two sensing techniques, the surface plasmon approach and the metal-clad sensor configuration, showed much promise and were further investigated.

6.1 Surface Plasmon Approach

At first, the use of surface plasmons for corrosion sensing did not seem feasible. The three-layer geometries utilized to that point could not operate with outer material indices less than 1.41. Since the outer material in a corrosion process is typically air (index of 1) or water (index of 1.33), this technique seemed to hold little promise. On further investigation, two potential methods for using optical fiber surface plasmons were discovered: the use of a four-layer system with the existing polished fiber approach and the use of cylindrically-coated fibers for surface plasmon generation.

The theoretical analysis performed on the four-layer system indicated that the system would work, and the outer index could be brought as low as needed for the sensor. The fabrication process proved to be an exacting process, where two evaporation processes had to be used and tolerances on the film thicknesses was very tight. Sensors were

fabricated and tested, and the system was proven to work. However, the complexity of fabrication was a great concern for practical development of the sensor.

The second approach, that of cylindrically coating a modified fiber with the metal, proved to be more practical. For this technique, the fiber cladding must be removed and replaced with a very thin film of the metal in question. The fiber must be relatively large core (at least 100 microns) and multimode. Step-index fiber is also highly desirable. Since the modes in the fiber can be approximated as rays propagating at different angles, the device is similar to the Kretschmann prism device, the first device used for exciting surface plasmons. This device consisted of a layer of metal coated onto a prism. The angle of incidence of the light onto the film from within the prism could be changed, and only one specific angle met the conditions necessary for surface plasmon generation. The angles in the fiber have the same effect and allow any index of refraction from 1 to 1.5 to be used as the outer material. The output was monitored in the wavelength regime, and the characteristic intensity dip was seen at the surface plasmon resonance point. This technique offered a practical manufacturing method (which is the same as the metal-clad method), and precise yet simple signal processing that could be used to indicate changes in the metal characteristics and geometry. The main problem with this geometry, which is a problem with all surface plasmon devices, is that they do depend so heavily on the outer material index of refraction. Since it is not known whether air or water or something else will surround the metal and sensor, the reference state of the sensor can not be known. If the surrounding environment changes, the output will change.

Future work for the surface plasmon sensor would have to concentrate on this problem. A method for separating the environmentally-induced changes from corrosion induced changes is needed. If the baselines for the possible environments could be determined and stored in the signal processing unit, the environment surrounding the sensor could be monitored, and the advent of corrosion could be sensed. The signal processing scheme

for this would involve calibrations for at least water and air as the outer material and then a monitoring system which could measure the change in the dip location from the baseline locations.

6.2 Metal-Clad Corrosion Sensor

As mentioned earlier, the metal-clad corrosion sensor was the most promising of all the sensing techniques investigated. Its unique response to corrosion, that of an increase in power level, offers advantages over other intensity-based techniques in that it is nearly immune to the usual noise sources caused by bending, connector losses and source fluctuations. The series of tests performed using the NaOH test setup demonstrated the operation and feasibility of the sensing technique. These tests also showed that a variety of sources could be used depending on the specific needs of the end user. Although no test results were obtained using the sputter-coating manufacturing method, the earlier results are more than sufficient to demonstrate the sensor. The new manufacturing technique has proven to be repeatable and reliable for the production of the sensors. Future tests will demonstrate the use of these sputter-coated sensors.

The output of the sensor is somewhat of a step function when the aluminum is thinned to the point where the light penetrates through the metal to the outer material. Any additional metal thickness only adds to the amount of corrosion necessary to reach the region where the output will change. The change in power for the sensor also occurs over a relatively small range of thickness values. In order to increase the sensitivity of the sensor to the amount of corrosion, it is proposed to use a tapered aluminum cladding to gradually increase the output power with corrosion.

6.2.1 Tapered Aluminum Sensors

The theory behind this idea is that a tapered aluminum cladding, i.e. linearly increasing in thickness with length, will still corrode at a fairly uniform rate along its length. As the cladding thins, the thinnest regions will experience the power increase first followed by the rest of the sensor as the metal continues to thin. The end result is expected to be a gradually increasing power level which can accurately represent the actual amount of corrosion that the sensor has experienced. Two techniques were devised that would allow the manufacture of such a sensor. The first is a progressive mask and coating process as shown in Figure 6.1. For this technique, a mask is applied over part of the cladding-less fiber and aluminum is coated onto the fiber. A second section of the mask is then removed and the coating process is repeated. The region where the first coating was applied grows thicker with the second coating. The process is repeated down the fiber coating the entire sensing length. The end result is a step-like function of thickness with length. As the corrosion occurs, each section will corrode at the same rate and the power level will increase in steps indicating when each metal thickness level is removed due to corrosion.

The second method involves first coating the maximum desired metal thickness onto the fiber and then etching off that metal to form a tapered geometry. The geometry is formed by slowly moving the fiber into and out of an acid etching bath as demonstrated in Figure 6.2. The rate of movement is used to determine the amount of thickness variation along the length of the sensor.

A first attempt to test the tapered fiber approach was performed using a sensor fabricated as described in Section 5.2.2. A 100 cm sensor was placed halfway into the NaOH and allowed to etch until approximately half the aluminum was removed in the etched region. This formed a step in thickness at the half-way point. The sensor was then tested as

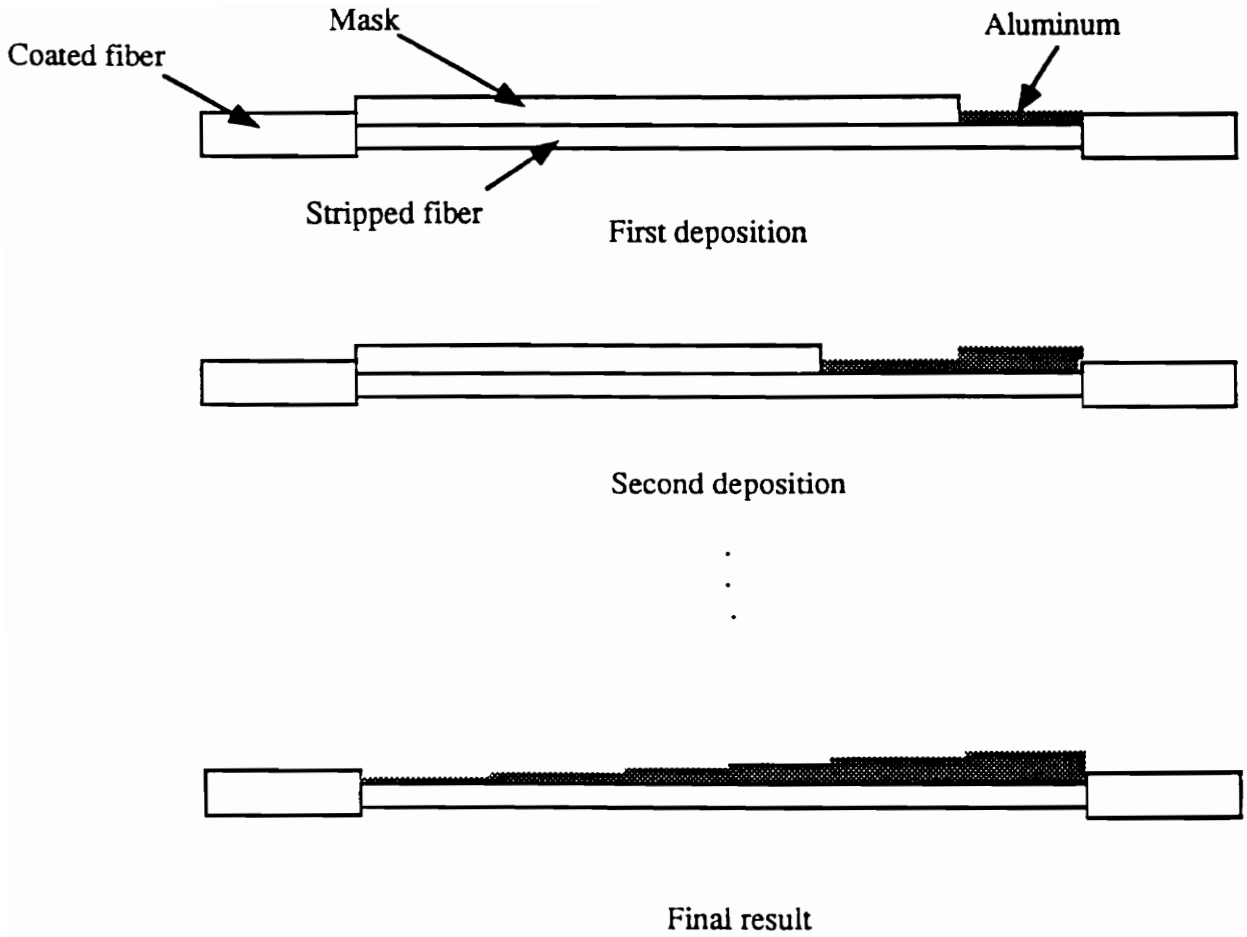
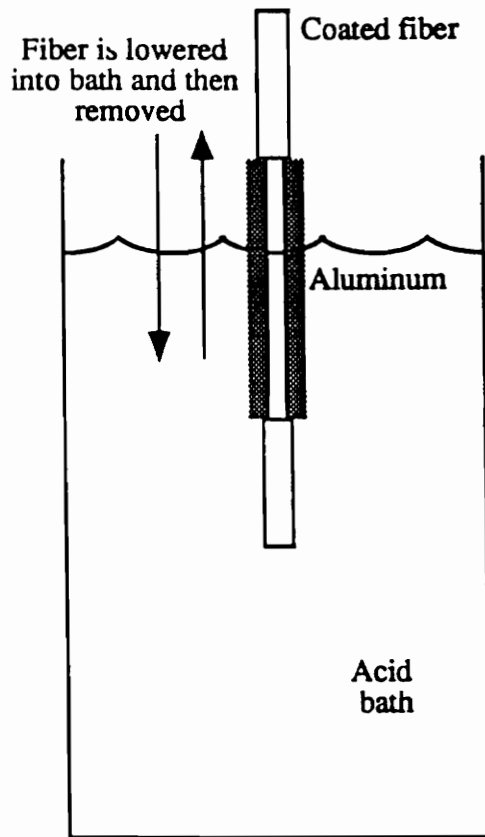


Figure 6.1. A diagram of the process and result of the masking technique for variable thickness coating fabrication.



Final result

Figure 6.2. The acid etch technique of variable thickness aluminum coating.

before and the results recorded. Figure 6.3 shows the results from this experiment. It is immediately obvious that the power increase is much more gradual than any of the other experimental curves. The dip is still present, and the initial step still appears, although not with the magnitude previously seen. This result is promising and indicates the need for further experimentation.

6.2.2 Reflective Sensor Design

An additional future development would be the incorporation of a reflective design for the sensor. For this sensor, the sensing length is halved, the fiber end is polished and coated with gold for high reflectivity, and the sensing region is then coated with the aluminum as shown in Figure 6.4. This adds reliability to the sensor because there is only one transition to the aluminum clad region. It also offers single-ended operation which is desirable in practice. Single-ended operation removes the need to bring a fiber back from the sensing region to the detector box. Also, only one connector is needed out of the signal processing unit.

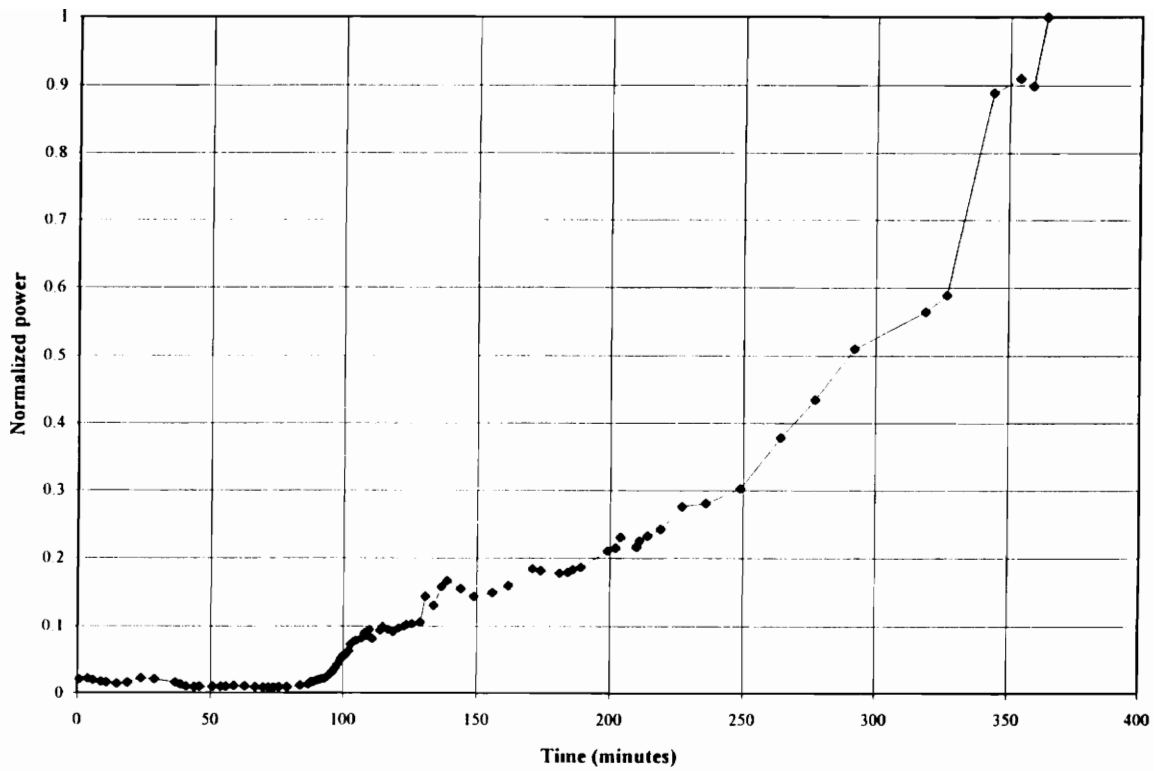


Figure 6.3. NaOH etch test on a half-etched 4" aluminum-clad sensor.

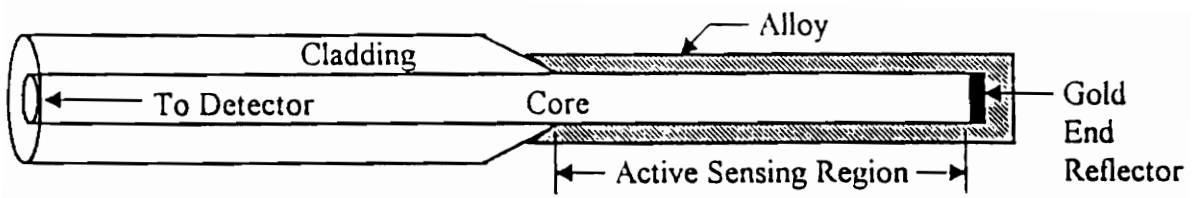


Figure 6.4. Proposed reflective aluminum-clad corrosion sensor.

REFERENCES

1. G. Keiser, Optical Fiber Communications, McGraw-Hill, Inc., New York, 1983.
2. S. D. Personick, Fiber Optics, Technology and Applications, Plenum Press, New York, 1985.
3. W. J. H. Bender, A Chemical Sensor Based on surface Plasmon Resonance on surface Modified Optical fibers, Ph.D. Dissertation, Department of Chemistry, Virginia Tech, 1993
4. W.J.H. Bender, R.E. Dessy, M.S. Miller. and R.O. Claus, "Feasibility of a chemical microsensor based on surface plasmon resonance on fiber optics modified by multilayer vapor deposition," *Analytical Chemistry*, Vol. 66, pp. 963-970, 1994.
5. L. L. Shreir, Corrosion Volume 1 "Metal Environment Reactions," Butterworth Publishers Inc., Boston, MA, 1978.
6. H. H. Uhlig and R. W. Revie, Corrosion and Corrosion Control, John Wiley & Sons Inc., New York, 1985.
7. J. M. West, Basic Corrosion and Oxidation, Ellis Horwood Ltd., West Sussex, England, 1986.
8. D. Slutzkin, Theory of Corrosion, Keter Publishing House Jerusalem Ltd., Jerusalem, Israel, 1976.
9. Handbook for Structural Engineering Repairs, Volume 1, Chapter produced by the Naval Aviation Depot, North Island, San Diego, California, 1989.
10. Corrosion Prevention and Control, Boeing Commercial Airplanes, Seattle, Washington, 1988.
11. G. C. Moran and P. Labine, Corrosion Monitoring in Industrial Plants, ASTM, 1986.
12. Aircraft Corrosion, AGARD Conference Proceedings No. 315, April 1981.

13. A. R. Bond, "Corrosion detection and evaluation by NDT", *British Journal of NDT*, Vol. 17, No. 2, pp. 46-52, 1975.
14. E. W. Richmond, Birefringent Single-Arm Fiber Optic Enthalpimeter for Catalytic Reaction Monitoring, Ph.D. dissertation, Department of Chemistry, Virginia Tech, 1990.
15. R. D. Rempt, "Active corrosion site detection scheme using optical fibers," *Review in Progress of QNDE*, July 1991.
16. K. A. Murphy, M. S. Miller, A. M. Vengsarkar, R. O. Claus, "Elliptical-core two-mode optical-fiber sensor implementation methods," *Journal of Lightwave Technology*, Vol. 8, p. 1688, 1990.
17. K. A. Murphy, M. F. Gunther, A. M. Vengsarkar, and R. O. Claus, "Quadrature phase-shifted, extrinsic Fabry-Perot optical fiber sensors," *Optics Letters*, Vol. 16, p. 273, 1991.
18. T. A. Tran, W. V. Miller, K. A. Murphy, A. M. Vengsarkar, and R. O. Claus, "Stabilized extrinsic fiber-optic Fizeau sensor for surface acoustic wave detection," *Journal of Lightwave Technology*, Vol. 10, p. 1499, 1992.
19. M. Gunther, A. Wang, B. Fogg, S. Starr, K. Murphy and R. Claus, "Fiber optic impact detection location system embedded in a composite material," *Proc. SPIE OE Fibers Conference (Boston, MA)*, September 1992.
20. M. Born and E. Wolf, Principles of Optics, Electromagnetic theory of propagation interference and diffraction of light, Sixth edition, Pergamon Press, New York, 1980.
21. A. Otto, "Excitation of non-radiative surface plasma waves in silver by the method of frustrated total reflection," *Z. Phys.*, Vol. 216, 1968, p.389.
22. H. Raether, "Surface plasma oscillations and their applications," *Physics of Thin Films*, volume 9, Academic Press, Inc., New York, 1977.
23. W. M. Robertson and E. Fullerton, *J. Opt. Soc. of America*, Vol. 6, 1989, p. 1584.
24. Y. Mao, H. A. Macleod, and K. Balasubramanian, *Applied Optics*, Vol. 28, 1989, p. 2914.
25. B. Liedberg, C. Nylander, and I. Lundstrom, *Sensors and Actuators*, Vol. 4, 1983, p. 299.
26. W. Eickhoff, "In-line fibre-optic polariser," *Electronics Letters*, Vol. 16, p. 762, 1980.
27. O. Parriaux, S. Gidon, and F. Cochet, "Fiber-optic polarizer using plasmon-guided wave resonance," in *Conf. Proc. 7th ECOL (Copenhagen, Denmark)*, 1981, p. 6-1.

28. D. Gruchmann, K. Petermann, L. Staudigel, and E. Weidel, "Fiber-optic polarizers with high extinction ratio," in Conf. Proc. 9th ECOC (Amsterdam), The Netherlands: Elsevier Science Publishers, 1983, p. 305.
29. J. Feth and C. Chang, "Metal-clad fiber-optic cutoff polarizer," *Optics Letters*, Volume 11, Number 6, p. 386, 1986.
30. S. Markatos, M. Zervas, I. Giles, "Optical fibre surface plasmon wave devices," *Electronics Letters*, Volume 24, p. 287, 1988.
31. W. Johnstone, G. Stewart, B. Culshaw, T. Hart, "Fibre-optic polarisers and polarising couplers," *Electronics Letters*, Volume 24, p. 868, 1988.
32. M. Zervas and I. Giles, "Optical-fibre surface-plasmon-wave polarisers with enhanced performance," *Electronics Letters*, Volume 25, p. 321, 1989.
33. W. Johnstone, G. Stewart, T. Hart, and B. Culshaw, "Surface plasmon polaritons in thin metal films and their role in fiber optic polarizing devices," *Journal of Lightwave Technology*, Volume 8, p. 538, 1990.
34. M. Zervas, "Surface plasmon-polariton fiber-optic polarizers using thin chromium films," *Photonics Technology Letters*, p. 597, 1990.
35. E. Economou, "Surface plasmons in thin films," *Physical Review*, Volume 182, p. 539, 1969.
36. R. C. Jorgenson, S. S. Yee, K. S. Johnston, and B. J. Compton, "A novel surface plasmon resonance based fiber optic sensor applied to biochemical sensing," SPIE Vol. 1886, *Fiber Optic Sensors in Medical Diagnostics*, p. 35, 1993.
37. A. Nagarajan, Chemical Sensing Applications of fiber Optics, Masters of Science Thesis, Department of Electrical engineering, Virginia Tech, 1994

APPENDIX A: COMPUTER PROGRAMS

The following computer programs were written for the metal-clad corrosion sensor theory. They are written for the MATLAB[®] environment. The following pages are the individual programs with the program title at the top of the page with a section label. The program AL_CLADC.M is the main program and the remainder are sub-programs used during the course of AL_CLADC.M.

AL CLAD.C

```
%Analytical Model for aluminum clad corrosion sensors
%   based on ray optics approximation
%   developed by Mark Miller
%   May, 1994
disp('This program derives the output of an aluminum clad fiber corrosion sensor.')
disp('A series of values must be input to define the sensor parameters.')
disp(' ')
disp(' ')
disp('First, we will define the sensor geometry.')
disp(' ')
length = input('What is the sensing region length [in millimeters]? ');
length = length/1000;
begthk = input('What is the beginning aluminum thickness [in microns]? ');
begthk = begthk/1000000;
disp(' ')
disp(' ')
disp('What type of fiber is being used?')
disp(' ')
coresz = input('What is the core diameter [in microns]? ');
coresz = coresz/1000000;
cladsz = input('What is the cladding diameter [in microns]? ');
n_one = input('What is the core index of refraction? ');
n_two = input('What is the cladding index of refraction? ');
disp(' ')
disp(' ')
disp('Some additional information required:')
disp(' ')
lambda = input('What is the wavelength of operation [in nanometers]? ');
lambda = lambda*1.E-9;
n_three = input('What is the index of the outer material? ');
disp(' ')
points = input('How many steps in aluminum thickness would you like? ');

theta_max = acos(n_two/n_one);
kk = 2*pi/lambda;
thetas = [theta_max/200:theta_max/200:theta_max]';
ms = angles(thetas,n_one,n_two,lambda,coresz);

disp(' ')
disp('calculating angles')
theta2 = maximize(thetas,ms,n_one,n_two,lambda,coresz);
num_refl = length*tan(theta2)./coresz;
```

```

theta2 = pi/2-theta2;
disp(' ')
disp('finished calculating angles')

n2c = realind(lambda);
kappa = imagind(lambda);
kappa2 = kappa/n2c;
n2compl = n2c * (1+kappa2*i);
theta_2 = asin(n_one*sin(theta2)./n2compl);
theta_3 = asin(n_one*sin(theta2)./n_three);

r12te = (n_one*cos(theta2)-
n2compl*cos(theta_2))./(n_one*cos(theta2)+n2compl*cos(theta_2));
r23te = (n2compl*cos(theta_2)-
n_three*cos(theta_3))./(n2compl*cos(theta_2)+n_three*cos(theta_3));
r12tm = (cos(theta2)./n_one-
cos(theta_2)./n2compl)./(cos(theta2)./n_one+cos(theta_2)./n2compl);
r23tm = (cos(theta_2)./n2compl-
cos(theta_3)./n_three)./(cos(theta_2)./n2compl+cos(theta_3)./n_three);

scaleval = gaussian(200);

l=1;
h=begthk;
while h >= 0

    beta = 2*pi*h*n2compl*cos(theta_2)./lambda;
    freflte = (r12te+r23te.*exp(2*i*beta))./(1+r12te.*r23te.*exp(2*i*beta));
    frefltm = (r12tm+r23tm.*exp(2*i*beta))./(1+r12tm.*r23tm.*exp(2*i*beta));
    refte = real(freflte).^2+imag(freflte).^2;
    reftm = real(frefltm).^2+imag(frefltm).^2;
    totrefl = .5*refte.^num_refl+.5*reftm.^num_refl;
    totrefl = [1;totrefl];
    powerout = totrefl.*scaleval;
    intens = sum(powerout);
    finals(1,1) = intens;
    finals(1,2) = h;
    l = l+1;
    h = h-begthk/points;
    if l==points
        h=0;
    end

end

end
plot(finals(:,2),finals(:,1))

```

ANGLES.M

```
function m = angle(x,n_one,n_two,lambda,coresz)
% Calculate m index versus angle for optical fiber

delta = 2*atan(((n_one/n_two)^2*(cos(x).^2-1).^(1/2)./(n_one/n_two)*sin(x)));
m=(2*n_one*2*pi*coresz./(lambda*sin(x))+2*delta)./(2*pi);
```

GAUSSIAN.M

```
function y=gaussian(x)
% determines a gaussian distribution with the 13.5% point
% at the center of the set of numbers
sigma = x/4;
set = [0:x]';
y = exp(-.5*(set./sigma).^2)./(sqrt(2*pi)*sigma);
tot = sum(y);
scale = 1/tot;
y = y.*scale;
```

IMAGIND.M

```
function kappa = imagind(lambda)
% determines the imaginary component of the complex index of refraction
% of the aluminum based on a lookup table

x =
[413.26;442.79;476.85;516.58;563.55;619.9;652.53;688.78;729.29;774.88;826.53;885.57
;953.69;1033.17;1127.09;1239.5;1377.56;1549.75;1771.14;2066.33];
x = x./1000000000;
y =
[5.024;5.385;5.8;6.283;6.846;7.479;7.821;8.205;8.573;8.597;8.309;8.212;8.949;10.01;11
.181;12.464;14.021;15.955;18.328;21.403];

kappa = interp1(x,y,lambda);
```

MAXIMIZE.M

```
function theta2=maximize(thetas,ms,n_one,n_two,lambda,coresz)
% finds the optimal angles to make m integers

for i = 1:200
if i<10
    step = .00000000001;
elseif i<40
    step = .000000001;
else step = .00000001;
end
    while abs(ms(i) - fix(ms(i)))>.01

        if i == 200
            thetas(i) = thetas(i)-step;
        elseif ms(i)-fix(ms(i)) > .5
            thetas(i) = thetas(i)-step;
        else thetas (i) = thetas (i) +step;
        end
        ms(i)=angles(thetas(i),n_one,n_two,lambda,coresz);
        %disp([ms(i), thetas(i), ms(i)-fix(ms(i))])
    end
disp([thetas(i),ms(i)])
end
theta2=thetas;
```

REALIND.M

```
function n2c = realind(lambda)
% determines the real component of the complex index of refraction
% of the aluminum based on a lookup table

x =
[413.26;442.79;476.85;516.58;563.55;619.9;652.53;688.78;729.29;774.88;826.53;885.57
;953.69;1033.17;1127.09;1239.5;1377.56;1549.75;1771.14;2066.33];
x = x./1000000000;
y =
[.523;.598;.695;.826;1.018;1.304;1.488;1.741;2.143;2.625;2.745;2.237;1.468;1.260;1.20
1;1.212;1.264;1.444;1.77;2.273];
n2c = interp1(x,y,lambda);
```

VITA

Mark S. Miller was born on November 29, 1966 in Rochester, New York, son of Theodore and Martha Miller. He graduated from Gates-Chili Senior High School, Rochester, New York, in 1984. Moving on to Virginia Polytechnic Institute and State University, he received Bachelors of Science and Masters of Science degrees in Electrical Engineering in November 1987 and April 1990, respectively. A member of the Fiber & Electro-Optics Research Center since 1987, he has also worked for Fiber and Sensor Technologies Inc. in Christiansburg, Virginia.

Mark was married to Rebecca Susan Oette of Rochester, New York on December 27, 1987 and now has two sons, Robert and Matthew. The family has recently relocated to Minneapolis, MN, where Mark now works for Rosemount Aerospace Inc.